University of Washington
Department of Civil and Environmental Engineering

NUMERICAL SIMULATION OF THE HYDRODYNAMICS OF OVERLAND FLOW WITH SPATIAL VARIATION IN ITS PHYSICAL CHARACTERISTICS

Weihua Zhang

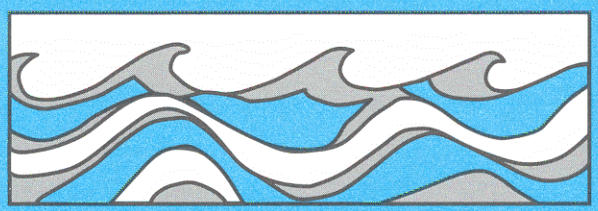

Water Resources Series
Technical Report No.123
August 1990

Seattle, Washington
98195

Department of Civil Engineering
University of Washington
Seattle, Washington 98195

NUMERICAL SIMULATION OF THE HYDRODYNAMICS OF OVERLAND FLOW WITH SPATIAL VARIATION IN ITS PHYSICAL CHARACTERISTICS

Weihua Zhang

Water Resources Series
Technical Report No. 123

August 1990

Department of Civil Engineering
University of Washington
Seattle, Washington 98195

NUMERICAL SIMULATION OF THE HYDRODYNAMICS OF OVERLAND FLOW WITH SPATIAL VARIATION IN ITS PHYSICAL CHARACTERISTICS

by

Weihua Zhang

Water Resources Series
Technical Report No. 123

August 1990

Research Supported by: U.S. Geological Survey
14-08-001G1154

U.S. National Science Foundation
EAR85-18058 & BSR-8107522

Principal Investigator: Thomas Dunne
Professor of Geology

Terrance W. Cundy
Professor of Forest Hydrology

ACKNOWLEDGEMENTS

This report is based on the author's Ph.D. dissertation, which reflects the influences of many people. I am grateful to Tom Dunne and Terry Cundy for their advice and support throughout this work. I would like to thank Steve Burges for his candid and immensely wise discussions about this research. I also wish to thank Wen-Sen Chu, Ron Nece and Jim Smith for their constructive suggestions along the way.

This research was supported by the U.S. Geological Survey under grant 14-08-001G1154 and the U.S. National Science Foundation under grants EAR85-18058 and BSR-8107522. The views and conclusions contained in this document are those of the author and should not be interpreted as necessarily representing the official policies, either expressed or implied, of the U.S. Government.

TABLE OF CONTENTS

LIST OF FIGURES

LISTS OF TABLES

Numbers

Chapter One

INTRODUCTION

1.1 Statement of the Problem

Overland flow is of fundamental importance to the hydrology of arid and semi-arid regions and on disturbed hillslopes under any climate. In these areas, overland flow is the dominant mechanism in the generation of floods, soil erosion and the transport of pollutants. However, our knowledge of overland flow on natural hillslopes and our ability to predict the above-mentioned processes is limited. Much work needs to be done to increase our understanding on the processes of overland flow, and thus, to improve our capability for prediction.

Natural hillslopes are not planar surfaces with homogeneous physical and hydraulic properties. Topography, surface roughness and soil hydraulic properties on natural hillslopes vary over distances of centimeters to meters. These spatial variations strongly influence the characteristics of overland flow, including the distributions of depth and velocity fields and the characteristics of hydrographs. The nature of these spatial variations cannot generally be identified by the usual inverse methods of calibrating available mathematical models or comparing basin runoff to sparse hydrological records. Yet, the resulting spatial

variabilities of depth and velocity fields strongly affect the spatial variability of the shear stress field in overland flow, and therefore have significant impacts on soil erosion, contaminant transport, and eventually hillslope geomorphology.

The characteristics of overland flow on natural hillslopes depend on the hillslope hydraulic properties. To analyze the impacts of hillslope spatial variations on the characteristics of overland flow, and to examine the relationships between the surface flow process and hillslope soil and vegetation features, detailed analysis of surface runoff on a spatially-varied hillslope is necessary. The relationships between overland flow and hillslope physical features and the description of detailed flow fields of surface runoff are also necessary input data to any of the physically-based erosion and transport models, which have been developed during the last decade (e.g., Simons et al., 1975; Foster, 1982; and Zhang, 1985).

The significance of spatial variability in soil-water parameters, surface roughness, topography and vegetation cover to the hydraulic and hydrologic response of hillslopes, including erosion, is widely recognized through field studies (Izzard, 1944; Emmett, 1970 and Abrahams et al., 1986). Dunne and his co-workers (Dunne and Dietrich, 1980; Dunne, 1983 and Aubry, 1984) conducted

field experiments to investigate overland flow processes and hillslope soil and vegetation features at plot scales. In the study, they made a series of direct and detailed measurements of surface runoff hydraulics on natural hillslopes and characterized the actual values of depth, velocity, resistance, their local variability and systematic downslope variation. These studies provided a comprehensive set of hydraulic data for surface runoff over plots on natural hillslopes and characterized the hydraulics of overland flow under the conditions of a realistic range of surface resistance, gradient, infiltration capacity and precipitation intensity. These field studies provide an insight into the hydraulics of overland flow on natural hillslopes. However, since the spatial characteristics of natural hillslopes vary significantly from place to place, field studies alone cannot lead to generalizations about hillslope hydraulic and hydrologic processes and hydraulic parameters. Physical and mathematical modeling is required.

While field studies clearly indicate the importance of two-dimensional flow on natural hillslopes where soil properties, microtopography and water interact in a complex manner, theoretical and modeling studies of overland flow in the past several decades have been limited to one-dimensional and homogeneous surfaces and dominated by use of the kinematic-wave equation (KWE). By

constraining the flow paths in one dimension and idealizing natural hillslopes as homogeneous planes, current models ignore the real, measurable spatial variations in hillslope characteristics. As a result, significant errors are created in, for example, the predicted distributions of flow velocity, depth, and shear stress, and in the predicted outflow hydrograph, and several interesting and important overland flow features are ignored. There are a few studies of two-dimensional overland flow, but only on the most simple surfaces and the effects of spatially-varying hillslope properties have not been incorporated. Without considering spatially-varying hillslope properties and relating them to the characteristics of overland flow, runoff models are of limited use for understanding the mechanics of runoff, soil erosion and pollutant transport.

In most modeling of runoff, the characteristics of overland flow, e.g., depth and velocity, and hydraulic parameters, e.g., surface resistance, have been back-calculated from plot or basin hydrographs without using field measurement of the spatial variations of flow and hillslope characteristics (e.g. Woolhiser et al. 1970). In so doing, current models lump the effects of spatial variations of hillslope characteristics with a few model parameters, especially, the parameters representing infiltration and surface roughness. The spatial variations

of hillslope characteristics vary widely for individual hillslopes and among different hillslopes. Simply lumping hillslope spatial variations with a few model parameters by the back-calculation from plots or basin hydrographs will result in the values of the model parameters being so variable for the "same" hillslope conditions that they are hard to use for prediction. As a result, current physically-based models lose their predictive nature, and become "parameter-fitting" or "parametrically-fitted" models.

Physically-based, multi-dimensional mathematical models, which incorporate the realistic spatial variability in hillslope characteristics, are necessary to: analyze and interpret field results in a realistic conceptual framework; draw generalizations about overland hydraulic processes and the hydraulic and hydrological parameters of hillslopes; and accurately predict the hydraulics and hydrology of overland flow. The expansion of model dimension and explicit incorporation of spatial variations in hillslope characteristics reduce the constraints in flow paths and allow runoff processes to be examined realistically.

In recent years it has been increasingly appreciated that for adequate hydraulic and hydrological characterization of overland flow on natural hillslopes it is necessary to study the effects of spatially-varying

hillslope properties on the variability of overland flow. This is the concern of recent studies by Smith and Hebbert (1979), Freeze (1980), Matias and Correia (1987) and Loague (1988). These studies, based on either the one-dimensional KWE or parametric equations, such as travel time routing and unit hydrographs, aimed at examining the bulk effects of spatially varied infiltration on hydrographs. Little attention has been paid to the effects of other spatially variable controls, such as topography and surface roughness. Because of the limitations of the available overland flow models, no attempt has been made to relate these spatial variations to measurable characteristics of overland flow. Therefore, the influences of spatial variations of these hillslopes variables are still largely unknown. Yet, it is widely reported in field studies that these effects are important.

Characterization of the hydraulics and hydrology of overland flow requires detailed simulations of overland flow fields using a physically-based and multi-dimensional model for assessing the significance of various aspects of variability on the hydraulic and hydrological responses of hillslopes. Such understanding should ultimately lead to better prediction of overland flow and its associated soil erosion.

1.2 Research Objectives

This research will develop a two-dimensional, hydrodynamic and numerical model for overland flow. The model explicitly incorporates realistic spatial variations in physical characteristics of hillslopes. Based on the detail simulation results of the model, the impacts of the spatial variations of hillslope properties on the characteristics of overland flow is examined, and the implications of the spatial variability of the overland flow on soil erosion are also discussed. Through quantitative analysis of the relationships between the characteristics of overland flow and spatial variations of hillslope characteristics, the study will provide a fundamental and realistic framework necessary for the prediction of surface runoff and soil erosion on spatially varied hillslopes.

These goals will be accomplished through the following specific objectives:

(1) to develop a mathematically rigorous and physically sound two-dimensional hydrodynamic and numerical model for overland flow. The model explicitly addresses spatial variations in infiltration, surface roughness and microtopography. Rainfall impacts will also be considered. The development of the hydrodynamic equation begins with the Navier-Stokes equation. The resulting model is solved by a numerical method, based on

the MacCormack finite-difference scheme. The complete hydrodynamic and numerical model is tested and validated with experimental data and compared with available models.

(2) to use the overland flow model to examine the effects of spatial variations in infiltration, surface roughness and microtopography on characteristics of overland flow. To achieve this, the overland flow model is used to conduct a series of systematic simulations for spatial variations of infiltration and surface roughness. Both the random and trending variations for these two variables are simulated. The impacts of microtopography on the characteristics of overland flow are analyzed based on model simulations for a series of mathematically-generated topographic surfaces and two field plots with realistic microtopography. Based on the simulation results, the study identifies the roles of different spatial variations of hillslope characteristics in overland flow and important hydraulic parameters of hillslopes.

(3) to examine the implications of the spatial variability of overland flow for soil erosion. For this purpose, the results of the spatially-variable overland flow fields simulated by the model are used to generate spatially-distributed shear stress fields. Then, a Du-Boys type equation is used to compute the relative soil erosion rate at individual cross-slope sections based on the computed excess shear stress. The bias in predicting the

excess shear stress fields and the soil erosion rate by the approximation of a spatially-variable surface with a homogeneous plane will be discussed. The influences of the soil resistance properties and the excess rainfall rate on the prediction is examined.

1.3 Significance of the Research

The research differs significantly from earlier attempts at overland flow modeling and the analysis of the spatial variability of overland flow. As with the introduction of spatially-varied and multi-dimensional modeling in groundwater flow and transport, the development of the physically-based, two-dimensional model breaks new ground for overland flow research and should advances overland flow modeling to a more realistic level than previously achieved. Such a model is not only essential for improved understanding of flood generation in arid and semi-arid areas but for fundamental study of soil erosion, transport and deposition processes, and therefore of hillslope geomorphology. In addition, the work will contribute to the ultimate solution of numerical and physical problems associated with the hydrodynamic equation for overland flow.

The analysis of the effects of these spatial variations will also contribute to an improved understanding of the processes responsible for flood

generation in small basins, pollutant transport, and soil erosion. The identification of the role and relative importance of hillslope spatial variables by the detailed model simulation suggests useful measures of hillslope characteristics for routine hydrology and erosion prediction.

Chapter Two

PROCESSES AND HYDRAULICS OF OVERLAND FLOW

2.1 Overland Flow as A Storm Runoff Process

Several processes produce storm runoff on a hillslope. Depending on the flow paths by which storm water reaches a stream, the runoff production processes are classified as Horton overland flow, saturation overland flow, and subsurface storm runoff. The relative importance of each process in a region is affected by climate, geology, topography, soil characteristics, vegetation, and land use. Dunne (1978) summarized the relation of the various runoff processes to their major controls (Figure 2.1).

Two processes that generate overland flow are Horton overland flow and saturation overland flow. Horton overland flow occurs whenever the rainfall intensity exceeds the soil infiltration capacity and the process is considered as soil controlled (Horton, 1933). In arid and semi-arid regions and those areas disturbed by humans, e,g., agricultural land, and construction and mining sites, Horton overland is the dominant storm runoff process.

Saturation overland flow occurs when soils become saturated from below by rising water tables. In the saturated areas, the soil infiltration rate reduces to

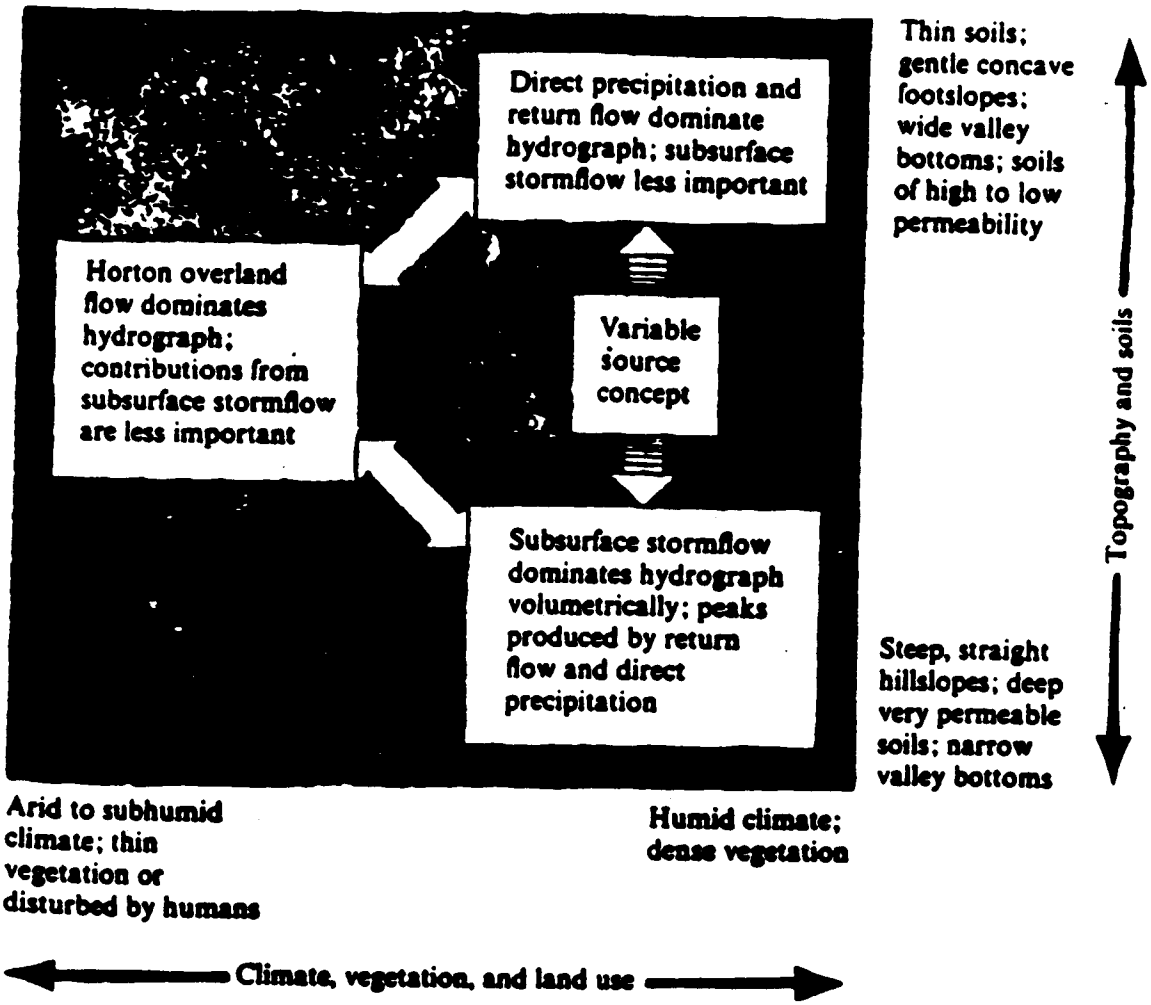

Figure 2.1 Runoff processes in relation to their major controls (from Dunne and Leopold, 1978).

zero, and there may be some exfiltration from the soil column to the surface. Besides soil properties, the control on this process include topography of the hillslope. Saturation overland flow is common on the hillslopes adjacent to stream channels in humid regions and is enhanced by shallow soils, convergent topography and extended periods of rainfall.

Both Horton overland flow and saturation overland flow are important for the generation of storm runoff hydrographs and hillslope soil erosion in their respective environments, but the emphasis of this research is on Horton overland flow. In the rest of this thesis, Horton overland flow is simply referred to as overland flow.

2.2 Soil Infiltration

Overland flow is generated at a point on a hillslope only after surface soil layers become saturated and surface ponding takes place. Horton (1933) showed that when rainfall reaches the soil surface, it infiltrates the soil surface at a rate that decreases with time. For heavy rains, the actual infiltration follows a limiting curve, called the infiltration capacity of the soil. The infiltration capacity decreases rapidly during the early part of a storm and reaches a more or less constant rate within a short time period, generally less than 30

minutes, as the storm continues (Figure 2.2). If the antecedent soil moisture content is large, the constant infiltration rate can be attained almost immediately. This final constant infiltration capacity is close to the saturated hydraulic conductivity of the soil in the absence of surface crusting (Rubin, 1966).

Theoretical consideration of infiltration and vertical soil-water movement led to the development of the following physically and mathematically rigorous partial differential equation

$$\frac{\partial \theta}{\partial t} = \frac{\partial}{\partial z}\left[D \frac{\partial \theta}{\partial z} \right] + \frac{\partial K(\theta)}{\partial z} \qquad (1)$$

Where θ is the volumetric moisture content, $K(\theta)$ is the hydraulic conductivity, D is the soil water diffusivity, z is the direction of gravity, and t is the time. This equation, known as the Richards equation, was first proposed by Richards (1931). Because of the boundary conditions needed and the difficulties in solving the partial differential equation, some simple, yet physically based infiltration equations are often used. Among them is the Philip equation. Philip (1957, 1958) proposed a simple algebraic equation derived from Richards equation

$$f = \frac{1}{2} S t^{-1/2} + A \qquad (2)$$

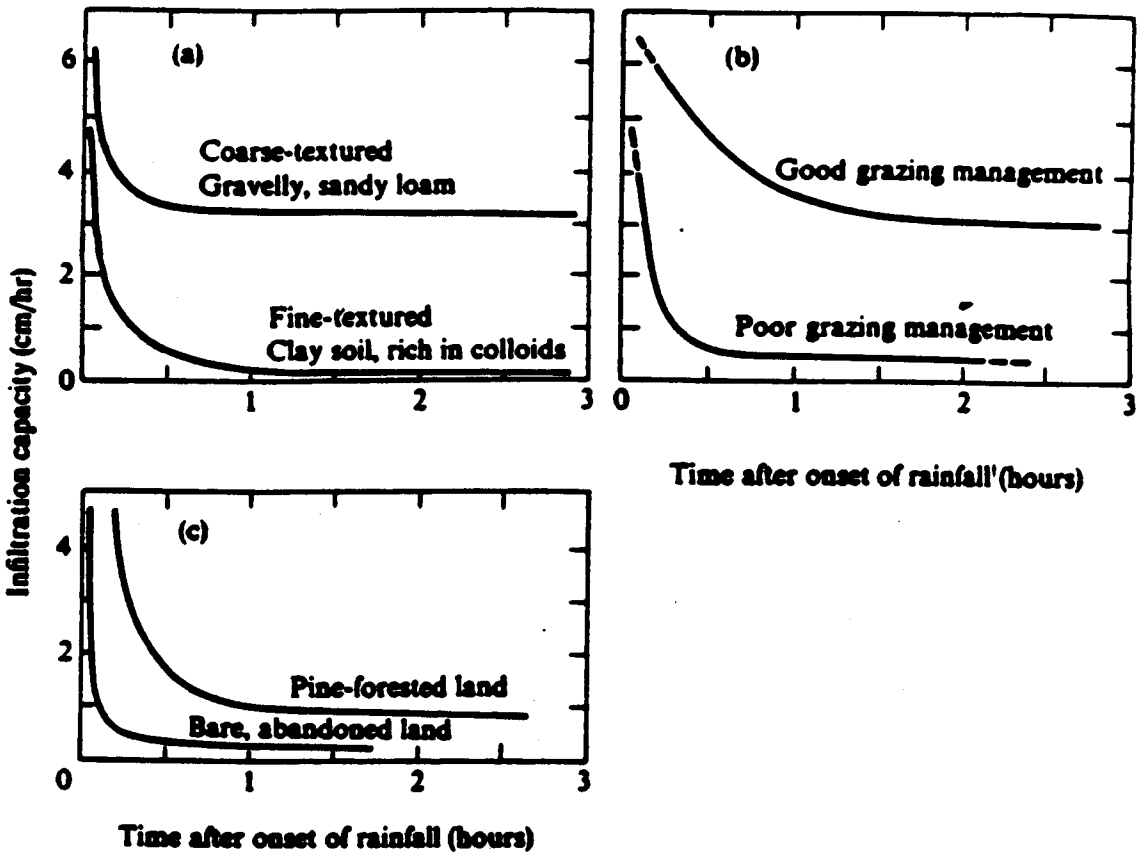

Figure 2.2 Infiltration capacity curves for soils of (a) different texture, (b) vegetive cover, and (c) land-use practice (from Strahler, 1975).

where f is the infiltration capacity, S is the parameter called sorptivity and A is the coefficient reflecting the final infiltration capacity and generally close to the saturated hydraulic conductivity.

It is clear from equation (2) that infiltration rates are mainly determined by two soil hydraulic parameters. The soil sorptivity parameter, S, dictates the shape of the limiting curve of infiltration capacity, and the final infiltration capacity, A, determines the final constant infiltration rate. Any time rainfall intensity exceeds the infiltration capacity, overland flow occurs. In large rainstorms, it is the final infiltration capacity that largely determines the amount of surface runoff generated on hillslopes (Dunne and Leopold; 1978). In the following discussions, the final infiltration capacity, A, is approximated by soil saturated hydraulic conductivity, K_s.

2.3 Hydraulic Resistance

Overland flow generally has depths between several millimeters and several centimeters and flow velocities of 0.5 to 20 centimeters per second. Because of the small depth of overland flow, the boundary effect of hillslope surfaces on the characteristics of overland flow is very large. Strong spatial variations of hillslope properties, therefore, result in a strong spatial variability in the characteristics of overland flow. Over a short distance,

the state of overland flow may change from laminar to turbulent, and from subcritical to surpercritical, or vice verse. Therefore, characterization of overland flow is more difficult than is the case for deep flow in rivers and estuaries.

The hydraulic equations for steady and uniform flow in open channels are given by either the Darcy-Weisbach equation or the Manning equation. For wide open channel, they are respectively defined as: Darcy-Weisbach equation

$$u = \sqrt{\frac{8g}{f} hS_f} \tag{3}$$

and Manning equation

$$u = \frac{1}{n} h^{2/3} S_f^{1/2} \tag{4}$$

where u is the vertically averaged velocity, h is the flow depth, f is the flow resistance parameter for Darcy-Weisbach equation, n is the surface roughness parameters for Manning equations, and S_f is the flow energy slope, which is equal to the bed slope for steady and uniform flow.

While the Manning equation is valid for turbulent flow only, the Darcy-Weisbach equation can be used for both laminar and turbulent flow, with f being a function of Renolds number:

$$f = \frac{K_o}{R_e} \tag{5}$$

where K_o is theoretically determined as 24 and R_e is the Reynolds number defined as

$$R_e = \frac{uh}{\mu} \tag{6}$$

where μ is the dynamic viscosity of water. For turbulent flow, the effect of Reynolds number reduces to a minimum, as the surface roughness becomes more important. For this case the f-R_e relation has an approximate slope of -0.2 on the Moody diagram and there are many empirical equations derived to describe the f-R_e relation.

For overland flow, Izzard (1944) and Emmett (1970) have shown that as bed surfaces get rougher, K_o in equation (5) can be several orders of magnitude lager than its theoretical value of 24. On the Moody diagram the resistance equation (5) is the lower limit for overland flow (Figure 2.3). The K_o for this case is therefore a parameter reflecting the surface roughness. While these descriptions of hydraulic resistance are accurate for steady and uniform flow in open channels, they were not derived to deal with some of the characteristics of overland flow, such as the local accelerations, changes in depth, form roughness effects due to gravel,

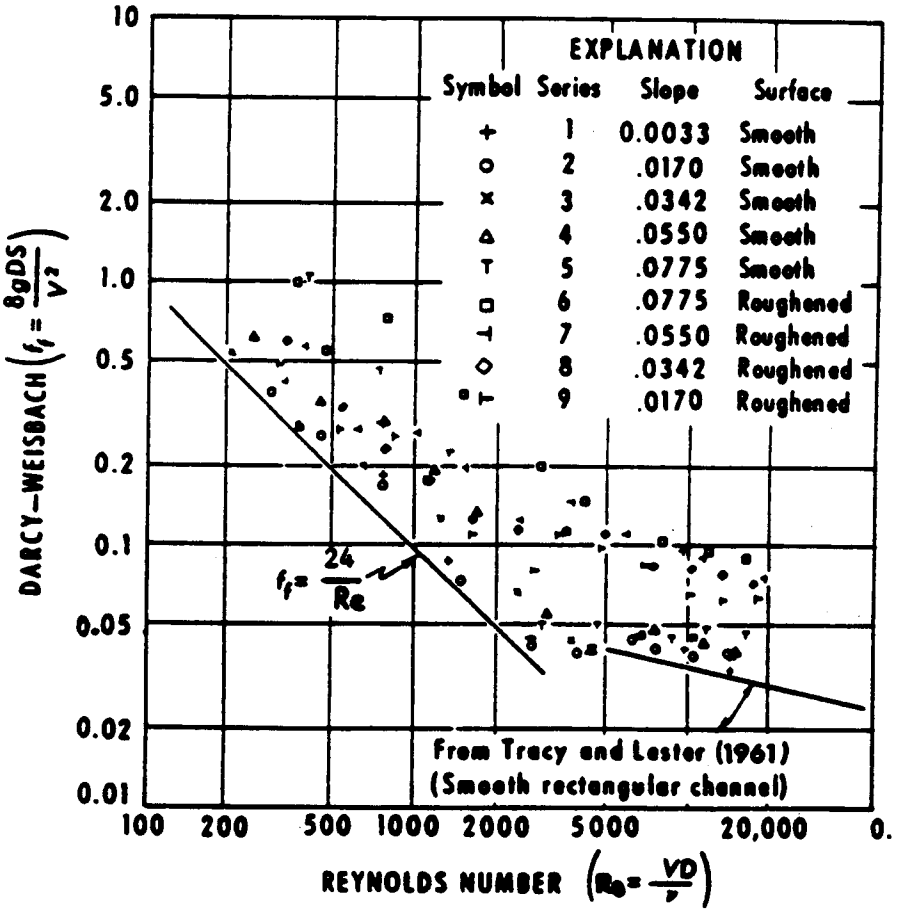

Figure 2.3 Darcy-Weisbach factor for uniform flow as a function of Reynolds number on a hillslope surface (from Emmett, 1970).

microtopography and vegetation roughness, and even the effects of rainfall impact. However, an assumption is usually made that the Darcy-Weisbach equation is appropriate for description of overland flow and field results are also consistent with those predicted by theory (Dunne and Dietrich, 1980).

2.4 Factors that Cause Spatial Variability in Overland Flow

On a plane surface, such as a paved plot or laboratory flume, a thin film of water may flow downslope with little cross-slope variation in depth and velocity. On natural slopes, overland flow generally appears as a shallow sheet of water with threads of deeper, faster flow diverging and converging around topographic protuberances and vegetation. The flow depth and velocity may vary markedly over a short distance, giving rise to changes in the state of flow. Over a small area the flow may be laminar, turbulent, or transitional, or may consist of patches of any of these three flow states. Under certain conditions the flow may become unstable and give rise to the formation of roll waves. The impact of rainfall on the sheet of flowing water further complicates the characteristics of overland flow.

Many factors cause spatial variability of overland flow on natural hillslopes. Some of the important ones

are: soil infiltration properties, surface roughness, microtopography, the patchiness of vegetation coverage and rainfall impact. Each of the factors is discussed below.

2.4.1 Soil Infiltration Properties

Soil infiltration determines the excess rainfall rate at a point on hillslope surfaces. Many factors influence the two soil hydraulic parameters S and K_s, including soil textures and structure and vegetation. Because these soil properties vary greatly on a given hillslope, the soil sorptivity parameter S and saturated hydraulic conductivity K_s show significant spatial variation for a given hillslope. Field measurements of the parameters S and K_s and their associated probability distributions and statistical properties are shown in Table 2.1. The distributions of S and K_s are best described by a lognormal distribution.

As a result of the significant variations of S and K_s, large spatial and temporal variations in rainfall excess are created on a hillslope surface. The spatially variable excess rainfall rate not only determines the quantity of surface runoff but is important to the characteristics of overland flow, including spatial variation of depth and velocity along and across the flow paths and the hydrographs.

Table 2.1 Summary of distributions of S and K_s

var.	dist.	mean	S.D.	soil type	reference
K_s	Lognormal	20.3	21.6	variable	Nielsen etal.(1973)
K_s	Lognormal	98.5	121.1	sand	Babalola (1978)
K_s	Lognormal	25.2	16.9	clay-loam	McCuen et al.(1981)
S	Lognormal	32.4	36.8	clay-loam	
K_s	Lognormal	1.32	.692	sandy-loam	Wagenet (1981)
S	Lognormal	6.56	1.61	sandy-loam	
K_s	Normal	.698	.279	loam	Vieira et al.(1981)
K_s	Lognormal	1.0	1.2	loam	Duffy et al.(1981)
K_s	Lognormal	.65	1.3	clay	
K_s	Lognormal	11.6	6.3	coarse-loam	Achouri & Gifford (1984)
K_s	Lognormal	16.2	5.76	-	Russo &
S	Normal	17.18	6.57	-	Bresler (1981)

note: all units are in cm-hr system

This table is reproduced from Cundy (1982).

2.4.2 Surface Roughness

By surface roughness, I mean specifically the skin roughness. This surface roughness is due to the small scale irregularities of the surface and mainly caused by grains or small gravels and the presence of vegetation. The effect of the surface roughness is to retard the flow, increase flow depth, and delay the arrival time of peak runoff discharge. Studies show that for different soil surfaces the roughness parameters are different, and the values of these parameters for different surfaces have been documented (Table 2.2). Some of the values were obtained by direct measurement and others by back-fitting of kinematic wave predictions to measured hydrographs. Even for the case of direct measurement, these surface roughness parameters were almost all computed from the hydraulic resistance equations by using measured mean flow velocity and depth. Besides the errors in measurements of flow depth and velocity, the effects of spatial variability of hillslope characteristics in, e.g., microtopography, infiltration, and rainfall impacts are all lumped in the surface roughness parameter. A separation of the roughness into components relating to the spatial variations of hillslope characteristics is necessary for improved understanding of overland flow processes on natural hillslopes.

Despite the extensive field studies on the effects of

Table 2.2 Surface roughness parameters for overland flow

surface	laminar flow K_o	turbulent flow Manning n
Concrete or Asphalt	24 - 108	.01 - .013
Bare Sand	30 - 120	.01 - .016
Gravel Surface	90 - 400	.012 - .03
Bare Clay-Loam (eroded)	100 - 500	.012 - .033
Sparse Vegetation	1000 - 4000	.053 - .13
Short Grass Prairie	3000 - 10,000	.10 - .20
Bluegrass Sod	7000 - 40,000	.17 - .48

Note: The table is reproduced from Woolhiser (1975).

surface roughness on overland flow, little attention has been paid to the nature of the spatial variability of surface roughness and its effects on overland flow. Aubry (1984), in his measurements on the Kenya hillslopes, showed that spatial patterns of soil particle sizes, therefore surface roughness, existed on natural hillslopes (Figure 2.4). Through flume experiments, Wu et al. (1978) illustrated the strong effects of spatial variability of surface roughness on the hydrographs. To understand the role of the spatial variability of surface roughness in overland flow, detailed study and simulation is necessary.

2.4.3 Microtopography

One of the major characteristics of natural hillslopes which the laboratory flumes do not reproduce, is microtopography. Microtopography is the deviation in local surface slope and aspect from the average slope and aspect of the hillslope. The scales of the microtopography may be characterized vertically by its amplitude and horizontally by its wave length. These amplitudes and wave lengths vary for hillslopes of different landscapes and for different positions along a given hillslope.

For many old landscapes in arid and semi-arid regions, such as the Kenya savanna hillslopes, slope surfaces generally appear rather smooth and the microtopography is characterized by relatively small

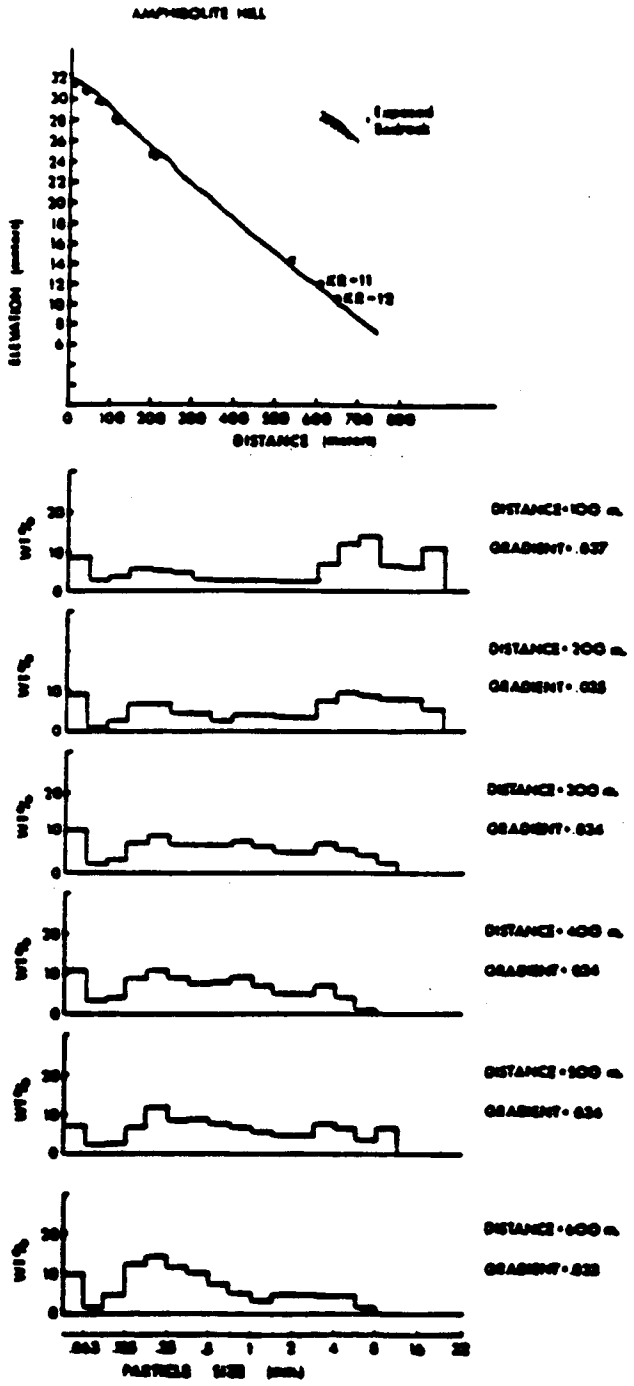

Figure 2.4 Frequency distributions of particle size in the surface soil at various locations along a typical hillslope in southern Kenya (from Aubry, 1984).

amplitudes and large wave lengths. The survey results on Kenya savanna hillslopes (Dunne and Aubry, 1988) showed that the microtopography had rather smooth curvature with the amplitude generally less than 0.10 m and the wave length ranging from 1 to 10 m. In these landscapes, the depressions in the microtopography on a hillslope are not incising to form rills over most of the hillslope length. Overland flow on these hillslopes is dominated by sheet flow covering the whole hillslope cross-section, at least over most of the hillslope length, however the flow does converge and diverge around microtopographic heights (Dunne and Aubry, 1988). Similar microtopography may also be found on hillslopes with surface soil formed with fine materials, e.g., those of the loess landscapes in the midwestern United States and in the upper-central part of the Yellow river basin in China.

For most of young landscapes, e.g., the pasture range lands in the western United States, surface soil is stony and hillslope microtopography is dominated by the cobbles and gravels of surface rubble and deeply incised rills. This microtopography gives rise to threads of concentrated overland flow in rills and between surface rubble. For this case, overland flow covers only fractions of the cross-slope sections.

The influence of microtopography on the characteristics of overland flow, especially, the flow

depth and velocity fields, has been demonstrated by many field studies. The altered flow fields of depth and velocity in overland flow will inevitably be reflected in the computed values of the hydraulic resistance if the measured mean depth and velocity are used, or the fitted values of a surface roughness parameter if the recorded hydrographs are used for back calculation. Emmett (1970) showed that the existence of microtopography increased the hydraulic resistance, f, and surface roughness parameter K_o, and therefore delayed the rising time of the hydrograph, whereas the study by Schumm et al. (1987) indicated that the existence of microtopography actually shortened the arrival time of the flow peak, therefore it would require a small fitted value of K_o, i.e., the existence of microtopography reduces the surface roughness. Obviously, the influence of microtopography on hillslope roughness depends on its geometric configuration. If the geometric configuration is favorable for flow convergence, the influence of the microtopography is to reduce the hydraulic roughness of the flow; otherwise it will increase the hydraulic roughness. Since the possible geometric configurations of microtopography for a given hillslope are, theoretically, unlimited, it would be difficult to parameterize the effects of microtopography as the hillslope roughness parameter for hydraulic and hydrologic prediction. The effect of the

microtopography should be examined as an independent hillslope variable, similar to the treatment of the saturated hydraulic conductivity, rather than a lumped surface roughness parameter.

2.4.4 Vegetation Coverage

The effects of vegetation on the characteristics of overland flow are complex. The evaluation of surface roughness due to vegetation has been conducted for both channel and overland flow. The studies of Lyatkher and Gurin (1977), Temple (1986), Petryk and Bosmajian (1975) and Chen (1975) showed that the existence of vegetation in an open channel could significantly slow down the flow. The nature of vegetation, including their heights, shapes and stiffness, has significant effects on the overall surface roughness and surface flow hydraulics. For example, Kouwen and Li (1980) observed that when water flows over a flexible vegetation, the vegetation may bend under certain conditions and reduce its height, and therefore reduce its resistance to the flow.

The effect of vegetation on surface roughness under overland flow conditions was studied by Izzard (1944). He found that the presence of vegetation could increase the surface roughness parameter K_o by several orders of magnitude. Dunne and his co-workers (Dunne and Dietrich, 1980; Aubry, 1984) analyzed the vegetation effects based

on their field studies of African hillslopes and suggested that the values of K_o increases with increasing vegetation coverage (Figure 2.5). Their work demonstrated that spatial variability in vegetation cover density exists on natural hillslopes due to spatial variation of soil and hillslope moisture conditions (Figure 2.6). Further analysis of these field observations (Dunne et al., 1987) indicated that vegetation was closely associated with both high infiltration capacity and microtopographic heights. This results in a positive relationship between measured infiltration capacity and rainfall intensity. These findings complicate the interpretations of vegetive effects on the characteristics of overland flow. More field and theoretical work must be done before vegetation effects can be incorporated into practical prediction by a physically based runoff model.

2.4.5 Rainfall Impacts

Raindrop impacts may have a significant influence on the hydraulics of overland flow, and thus on measured surface roughness. As raindrops enter the thin layers of overland flow, they generate splashing craters on the water surface and create turbulence in the flow. These splashing impacts can causes energy loss and increase flow resistance. This is particularly important in shallow laminar flow over a smooth surface. The rainfall splashing

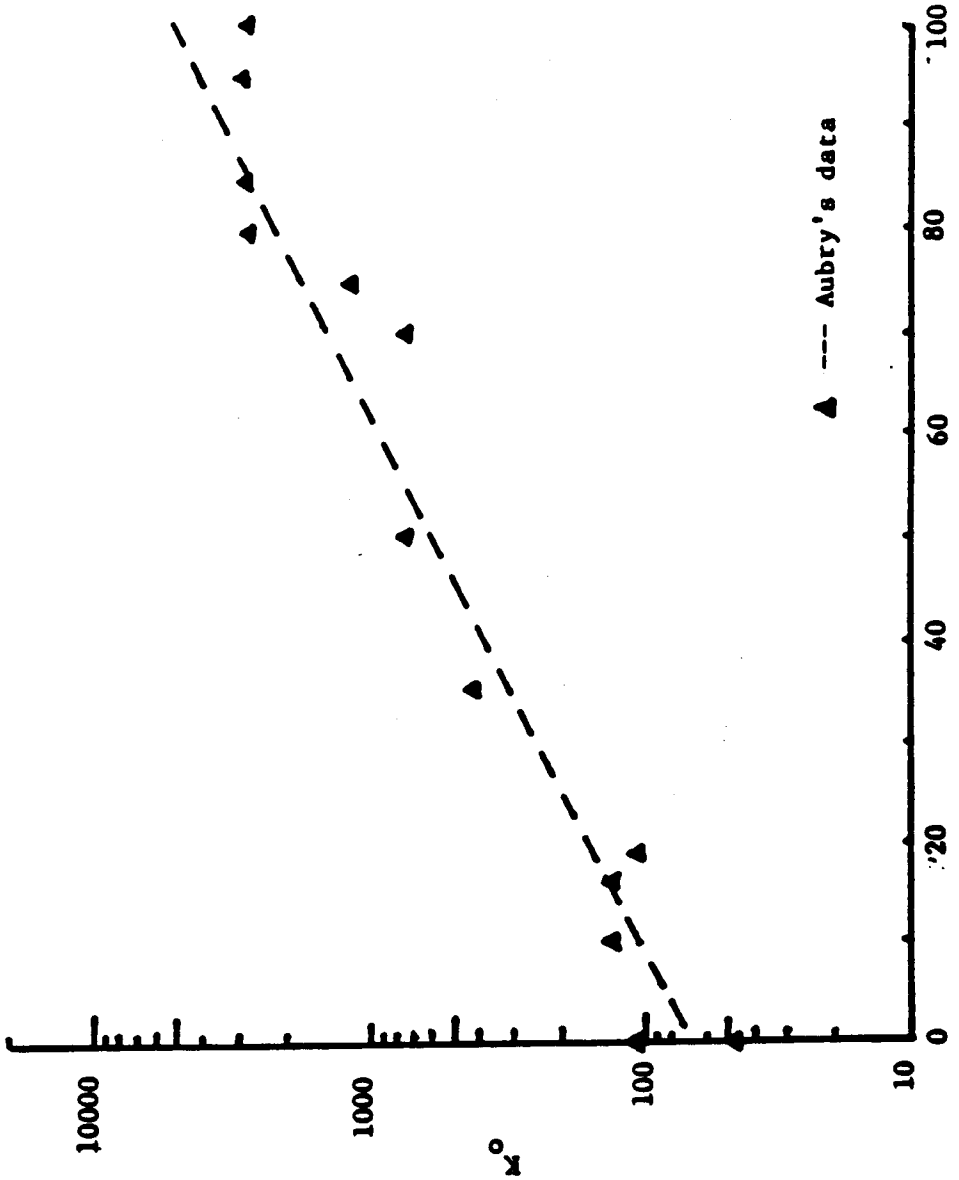

Figure 2.5 Surface roughness parameter K_o versus vegetation cover density.

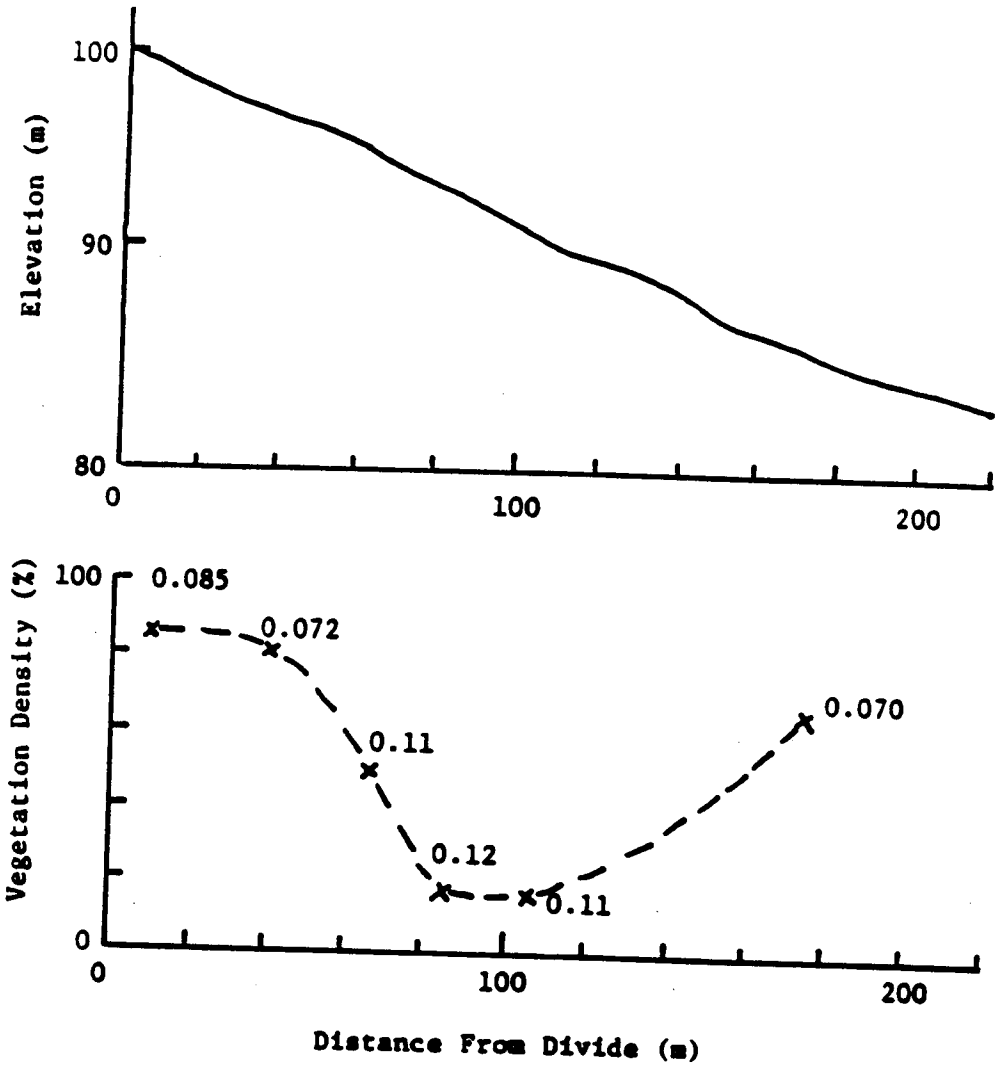

Figure 2.6 Spatial variation of vegetation cover density along a hillslope in northern Kenya. The numbers along the lower curve are local topographic gradients (from Aubry, 1984).

impact on overland flow is a complex phenomena and has not been well understood. Yoon and Wenzel (1971) showed through a laboratory experiment that the rainfall impacts could cause considerable retardation of shallow flow (Figure 2.7), and thus increase the hydraulic resistance. As the flow becomes more turbulent and the bed surface gets rougher, the rainfall impacts become insignificant (Izzard, 1944 and Kisisel et al, 1971).

In the absence of a sound theoretically based computation of the effects of raindrop impacts on flow resistance, Shen and Li (1973) have experimentally determined the equations for the Darcy-Weisbach coefficient f for flow with raindrop impacts. For laminar flow:

$$f = \frac{K_o + K_1 \, r^{0.41}}{R_e} \tag{7}$$

and for turbulent flow:

$$f = \frac{K_2}{R_e^{0.25}} \tag{8}$$

where K_o is the hillslope roughness and K_1 is the parameter related to raindrop velocity and K_2 is the roughness coefficient of turbulent flow, r is the rainfall intensity in in/hr. Since these equations were determined for a smooth surface (a stainless steel plate), their

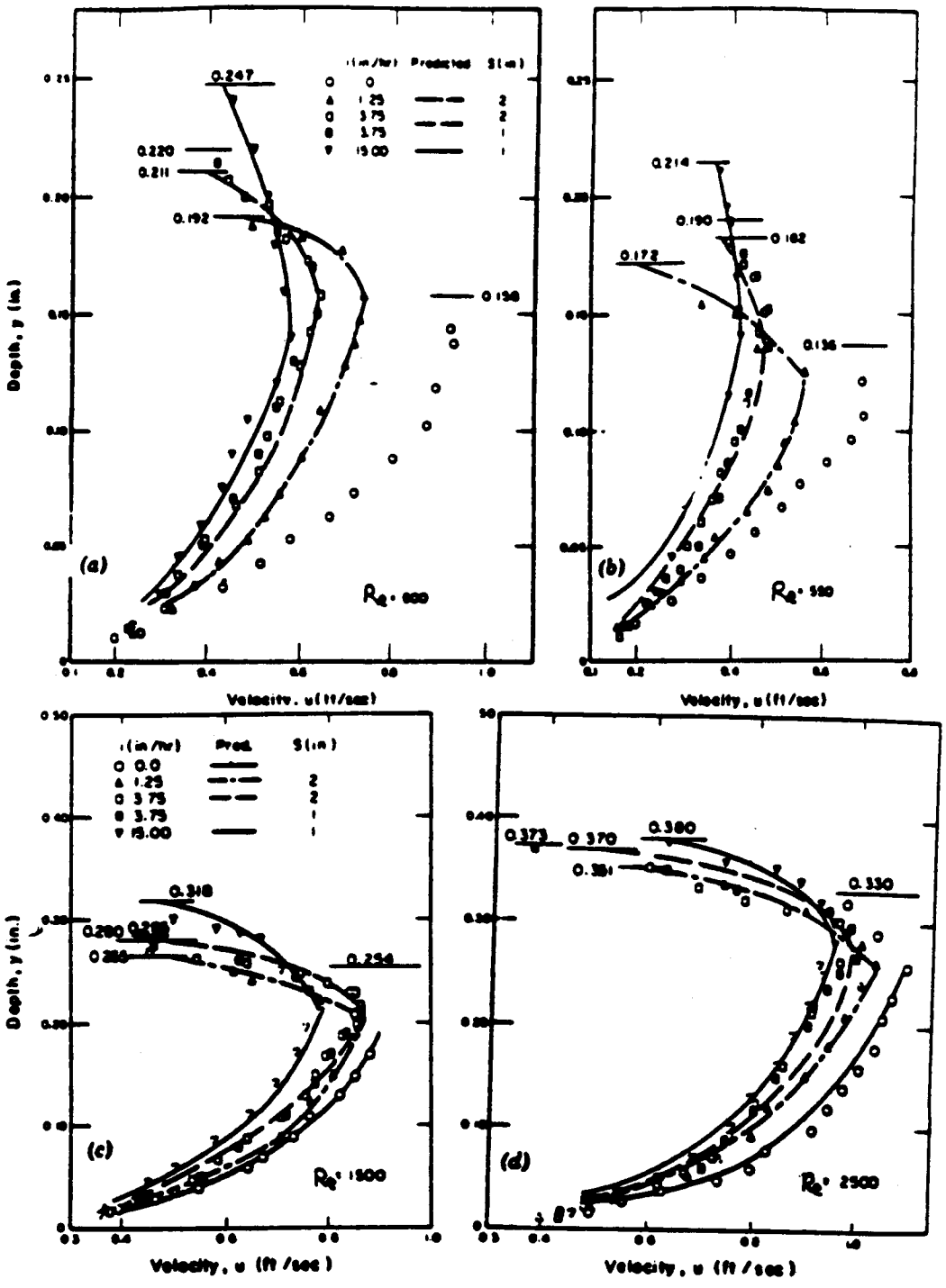

Figure 2.7 Velocity profiles showing the retarding effect of rainfall impact (from Yoon and Wenzel, 1971).

applicability for prediction on natural hillslopes is limited. Further study of effects of rainfall impacts on rough surface is needed.

2.5 Summary

The hillslope properties of infiltration, surface roughness, microtopography and vegetation can vary greatly over short distances on a natural hillslope, and strongly influence the hydraulics and hydrology of overland flow. Rainfall impacts may have significant influence on overland flow if the flow is laminar and the slope surface is smooth. The roles of the hillslope variables and their associated spatial variations have not been fully understood and their effects on overland flow have not been described quantitatively. In chapter four, I will examine the effects of soil infiltration, surface roughness and microtopography on the characteristics of overland flow by using a two-dimensional hydrodynamic and numerical model. The effects of vegetation on overland flow is not addressed.

Chapter Three

DEVELOPMENT OF A TWO DIMENSIONAL OVERLAND FLOW MODEL

3.1 Background Review

The earliest scientific studies and modeling of overland flow were carried out by Horton and his colleagues (1934). Since then many overland flow models have been developed. The two notable classes of overland flow models are those based on empirical relationship such as the rational and unit hydrograph methods, and those based on the physics and hydraulics of overland flow. The latter class is mainly based on the hydrodynamic equation or de Saint Venant equation and its simplified forms.

Based on the principles of conservation of mass and momentum, de Saint Venant in 1871 derived mathematically rigorous one-dimensional equations for gradually varied unsteady flow. The equations may br written in the following form: continuity equation

$$\frac{\partial h}{\partial t} + \frac{\partial (uh)}{\partial x} = V_o \qquad (9)$$

and momentum equation

$$g\frac{\partial h}{\partial x} + u\frac{\partial u}{\partial x} + \frac{\partial u}{\partial t} = g(S_o - S_f) \qquad (10)$$

(I) (II) (III) (IV) (V)

where h is the flow depth, u is the velocity, V_o is the lateral inflow rate or excess rainfall rate for overland flow, g is the acceleration of gravity, S_o is the slope of the surface and S_f is the flow energy slope. The terms on the left-hand side of the momentum equation reflect the flow properties. Term (I) represents the pressure differential of the flow due to depth variation and is insignificant for steady uniform flow; (II) is the convective inertia term and describes non-uniform flow; (III) represents the local inertia of the flow and is significant for unsteady flow. The terms on the right-hand side of the equation reflect the properties of the bed on which the water is flowing. Term (IV) is the gravitational energy component due to bed slope. Term (V) reflects the flow energy slope, which mainly reflects the resistance or friction effects of the bed surface.

Because of the difficulties in its solution for overland flow, attempts have been made to simplify the equation. Depending on the degree of simplification of the momentum equation, different forms of overland flow equations can be constructed. The most commonly used overland flow model resulting from such simplifications is the kinematic wave equation (KWE). The physical theory of the KWE was proposed by Lighthill and Whitham (1955), and first applied to the overland flow problem by Henderson and Wooding (1964). The underlying assumption for the KWE

is that energy variations of the flow due to depth pressure and local and convective accelerations are negligible in comparison with the gravitational energy component and friction effects of the bed slope. Therefore, all three terms relating to flow properties on the left-hand side of the momentum equation may be ignored. This results in a significant simplification to the momentum equation:

$$S_o = S_f \tag{11}$$

If we substitute equation (11) into equations (3) or (4), we have the following general form:

$$u = \alpha h^{\beta} \tag{12}$$

where α and β are parameters reflecting the slope and surface roughness of the bed and flow mode, respectively. For different flow resistance equations, α and β are expressed as: for the Darcy-Weisbach equation:

$$\alpha = \left[\frac{8g\ S_o}{f} \right]^{1/2} \qquad \beta = 1/2 \tag{13}$$

and for the Manning equation:

$$\alpha = \frac{S_o^{1/2}}{n} \qquad \beta = 2/3 \tag{14}$$

Using the method of characteristics, Henderson and Wooding (1964) developed an analytical solution to the KWE over a sloping plane with constant lateral inflow. Using the same approach, Cundy and Tendo (1985) analytically solved the KWE incorporating Philip's equation for unsteady infiltration on a plane surface. Li et al. (1975) developed a finite difference solution to the KWE, which allows unsteady non-uniform lateral input. All these models can be used to predict and simulate overland flow discharge, depth and velocity along the slope surface. However, the applications of these models are restricted to one-dimensional flow on a plane surface.

To incorporate variable slopes, Kibler and Woolhiser (1970) introduced the kinematic cascade model for overland flow. In the model the space dependence is removed by making the hillslope properties and lateral inflow piecewise uniform in space. The hillslope is divided into a series of plane segments with properties remaining constant within each plane segment but varying from segment to segment. Using the same idea, a more sophisticate kinematic shock fitting technique was developed by Borah et al. (1980). The method further eliminated the time dependence of the model parameters and lateral input by assuming each to be piecewise constant in time. Then the KWE is solved for each cascade segment subject to given initial and upstream boundary conditions.

The kinematic cascade model provides insight into the problem of overland flow with spatially and temporally dependent hydraulic parameters and lateral input. Yet, it does not allow cross-slope variation of the flow. Furthermore the method does not allow back facing slopes in any of the cascade planes, due to the limitations of the kinematic wave assumptions; this is a significant limitation if one is considering the effects of microtopography on runoff characteristics.

Woolhiser and Liggett (1967) showed that the prediction error of the KWE is significant, when the kinematic wave number (k) is small. The number is defined as

$$k = \frac{S_o L_o}{F_o^2 h_o} \tag{15}$$

where L_o is the slope length, h_o is the normal flow depth, and F_o is the Froude number for normal flow, expressed as

$$F_o = \frac{u_o}{(gh_o)^{\frac{1}{2}}} \tag{16}$$

where u_o is the normal velocity. This is the case for a surface of small slope, short length, smooth surface and with less intense rainfall. Woolhiser and Liggett (1967) suggested that the criterion for using the KWE is $k > 10$. For $k < 10$, the error in rising hydrograph by the KWE

would be more than 10%. This criterion is only for flow over a plane surface. For applications where a front face is formed due to spatial variation in slope, roughness, or lateral inflow along the flow path, the KWE is inadequate (Miller, 1984). Attempts to extend the KWE to two-dimensional overland flow have been made by Kuchment (1980), Constantinides and Stephenson (1981) and Cordova et al. (1982), among others. Their applications have been limited by the kinematic wave assumption.

Morris and Woolhiser (1980) introduced the diffusion wave approximation to the full de Saint Venant equation of overland flow to replace the KWE. The diffusion wave model uses the full continuity equation and simplified momentum equation by keeping an additional term (I) in the momentum equation to reflect the changes in kinetic energy. The momentum equation for this model is

$$\frac{\partial h}{\partial x} = S_o - S_f \qquad (17)$$

The diffusion wave model was solved by using either a finite difference method (Morris and Woolhiser, 1980) or a weighted residual method (Govindaraju et al., 1988). Their solutions showed that the diffusion wave model is a good approximation to the full Saint-Venant equation for small kinematic wave numbers where the KWE fails. Diffusion waves propagate only in the downstream direction, although

they attenuate as they move downstream. Therefore, the method is not suitable for the case where pronounced variations of local bed gradient and local flow occur. Ponce et al. (1978) presented the following criterion for the diffusion wave model to be adequate:

$$T\, S_o \left[\frac{g}{h}\right]^{1/2} \geq 30 \qquad (18)$$

where T is the wave period or length of time required for one wave to pass. If the left hand side of the equation is less than 30, the de Saint-Venant equation should be used.

Due to significant variations of physical and hydraulic characteristics of natural hillslopes, neither the KWE nor the diffusion wave model can be universally applied to overland flow without considerable compromise in accuracy, especially if they are used to simulate the overland flow field. Consequently, it becomes necessary to use the de Saint-Venant equation in modeling of overland flow. However, due largely to mathematical and numerical difficulties, the de Saint-Venant equation has never been properly solved for overland flow, either mathematically or numerically; therefore its application to overland flow has been extremely limited.

The one-dimensional hydrodynamic equation has been used for modeling of overland flow by Liggett and Woolhiser (1967) and Akan and Yen (1981). Liggett and

Woolhiser conducted extensive numerical experiments to compare different numerical schemes in solving the hydrodynamic equation for overland flow. This work provided experience and guidelines for the solutions to the hydrodynamic equation for overland flow. Akan and Yen developed an overland flow model which consisted of a one-dimensional hydrodynamic equation for surface flow and a subsurface flow equation. Both studies dealt only with one-dimensional homogeneous planes.

Chow and Ben-Zvi (1973) modeled overland flow by using a two-dimensional hydrodynamic equation, solved by using the Lax-Wendroff scheme. Yet, in the subsequent example problem they had to use a much simplified version of the hydrodynamic equation in which all the terms related to the convective acceleration were dropped from the hydrodynamic equation. These terms are significant in the presence of spatial variations in hillslope characteristics, which could not therefore be incorporated in the model. Katapodes and Strelkoff (1979) used a characteristic method to solve the two-dimensional flow. They clearly point out the advantages of characteristic methods, however, for the general overland flow case of spatial variability in slope, roughness and infiltration, characteristic methods are not tractable. Kawahara and Yokoyama (1980) presented a two-dimensional overland flow model, in which the two-dimensional shallow water equation

was solved by a finite element scheme. Spatial variability in infiltration and roughness were not included in their model. Hromadka et al. (1987) developed a diffusion hydrodynamic model, in which both the convective acceleration and local acceleration terms were dropped from the hydrodynamic equation.

In this paper, a two-dimensional hydrodynamic equation is developed for overland flow. The hydrodynamic equation is solved by a numerical scheme based on the explicit, second-order-accurate, MacCormack finite difference scheme. This scheme allows realistic spatial variation of hillslope features, including surface roughness, infiltration and microtopography.

To the best of the writer's knowledge, the hydrodynamic equation for overland flow has not been applied to a two-dimensional surface, and no attempt has been made in utilizing the hydrodynamic equation, either one-dimensional or two-dimensional, to model overland flow on non-uniform hillslopes.

3.2 Development of the Governing Equations

The general hydrodynamic equations of continuity and motion for an incompressible fluid with a constant density and without consideration of surface tension can be expressed as (Dronkers, 1964)

$$\frac{\partial u}{\partial x} + \frac{\partial v}{\partial y} + \frac{\partial w}{\partial z} = 0 \tag{19}$$

$$\frac{\partial u}{\partial t} + \frac{\partial uu}{\partial x} + \frac{\partial vu}{\partial y} + w\frac{\partial wu}{\partial z}$$

$$= -\frac{1}{\rho}\frac{\partial p}{\partial x} + \frac{1}{\rho}\left[\frac{\partial \tau_{xx}}{\partial x} + \frac{\partial \tau_{yx}}{\partial y} + \frac{\partial \tau_{zx}}{\partial z}\right] + F_x \tag{20}$$

$$\frac{\partial v}{\partial t} + \frac{\partial uv}{\partial x} + \frac{\partial vv}{\partial y} + w\frac{\partial wv}{\partial z}$$

$$= -\frac{1}{\rho}\frac{\partial p}{\partial y} + \frac{1}{\rho}\left[\frac{\partial \tau_{xy}}{\partial x} + \frac{\partial \tau_{yy}}{\partial y} + \frac{\partial \tau_{zy}}{\partial z}\right] + F_y \tag{21}$$

$$\frac{\partial w}{\partial t} + \frac{\partial uw}{\partial x} + \frac{\partial vw}{\partial y} + w\frac{\partial ww}{\partial z}$$

$$= -\frac{1}{\rho}\frac{\partial p}{\partial z} + \frac{1}{\rho}\left[\frac{\partial \tau_{xz}}{\partial x} + \frac{\partial \tau_{yz}}{\partial y} + \frac{\partial \tau_{zz}}{\partial z}\right] + F_z \tag{22}$$

where u, v and w are the projections of the velocity vector on the coordinate axes x, y and z, respectively, ρ is the density of water, p is the pressure of water, and τ is the shear or normal stress, with the following convention: the first subscript indicates the direction normal to the plane being considered and the second subscript indicates the direction of stress. F_x, F_y and F_z are the x, y, and z components of body force per unit mass. With reference to the cartesian coordinate system shown in Figure 3.1, where the z coordinate is parallel to and opposite of the direction of the gravity, the body

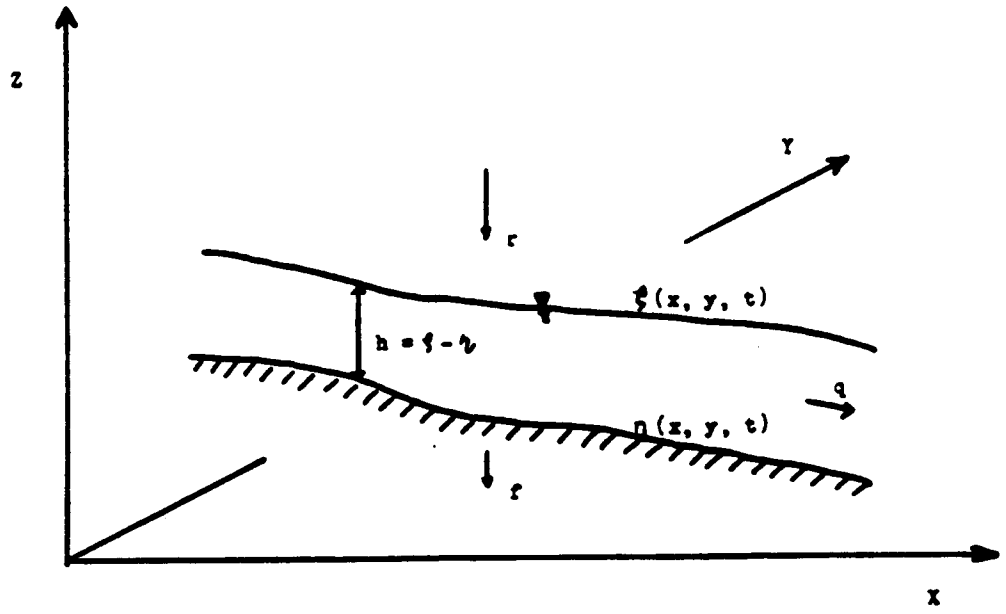

Figure 3.1 Schematic representation of cartesian coordinates for overland flow.

forces in x and y directions vanish, except that in the z direction where

$$F_z = - g \tag{23}$$

where g is the acceleration due to the gravity.

These general equations are meant here to include both laminar and turbulent flows. For turbulent flow the velocity components u, v and w represent mean velocity over short time intervals. The shear or normal stresses expressed above, therefore, include viscous stress and Reynolds' stress arising from the transfer of momentum by the turbulent motions. For convenience, only the shear stress terms in equation (20) are given below. Those in equations (21) and (22) can be defined similarly.

$$\tau_{xx} = \mu \frac{\partial u}{\partial x} - \rho \langle u'u' \rangle \tag{24}$$

$$\tau_{yx} = \mu \frac{\partial u}{\partial y} - \rho \langle u'v' \rangle \tag{25}$$

$$\tau_{zx} = \mu \frac{\partial u}{\partial z} - \rho \langle u'w' \rangle \tag{26}$$

where μ is the dynamic viscosity of water, u', v' and w' are the fluctuations of the velocity components around their corresponding mean value and <> indicates an average over a short time interval. In the above equations, the first and the second terms on the right hand sides of the

equations represent viscous stress and Reynolds' stress, respectively.

For the problem of overland flow shown in Figure 3.1, the following kinematic boundary conditions can be defined for the general hydrodynamic equations:

at the free surface $z = \xi(x,y,t)$

$$\frac{d\xi}{dt} = \frac{\partial \xi}{\partial t} + u_\xi \frac{\partial \xi}{\partial x} + v_\xi \frac{\partial \xi}{\partial y} = w_\xi - r(x,y,t) \qquad (27)$$

at the bed surface $z = \eta(x,y,t)$

$$\frac{d\eta}{dt} = \frac{\partial \eta}{\partial t} + u_\eta \frac{\partial \eta}{\partial x} + v_\eta \frac{\partial \eta}{\partial y} = w_\eta + f(x,y,t) \qquad (28)$$

where ξ and η are the free surface and bed surface elevations, respectively; u_ξ, v_ξ, and w_ξ are the velocity components at the free surface in x, y, and z directions, respectively; u_η, v_η, and w_η are the velocity components at the bed surface in x, y, and z directions, respectively; r is the rainfall rate; and f is the infiltration rate.

Two-dimensional overland flow equations are developed by vertically averaging equations (19) to (22) over the flow depth and using the above kinematic boundary conditions. In the derivation of the two-dimensional equations, the following assumptions were made: 1) for shallow water flow of long waves, the vertical acceleration of a fluid particle, dw/dt, is small in

comparison to the acceleration of gravity, 2) again in the case of long waves, the shear stresses due to the vertical velocity component, $\nabla^2 w$, are also small, 3) the terms due to horizontal shear on vertical surfaces, $\partial^2 u/\partial x^2$, $\partial^2 u/\partial y^2$, $\partial^2 v/\partial x^2$ and $\partial^2 v/\partial y^2$ are small compared with the terms due to vertical shear on horizontal surfaces, $\partial^2 u/\partial z^2$ and $\partial^2 v/\partial z^2$. Therefore, these terms were neglected in the development of the equations. The resulting two-dimensional overland flow equations are:

$$\frac{\partial(\xi-\eta)}{\partial t} + \frac{\partial q_x}{\partial x} + \frac{\partial q_y}{\partial y} = r(x,y,t) - f(x,y,t) \qquad (29)$$

$$\frac{\partial q_x}{\partial t} + \frac{\partial[\beta_x q_x^2/(\xi-\eta)]}{\partial x} + \frac{\partial[\beta_{xy} q_x q_y/(\xi-\eta)]}{\partial y} - u_\xi r$$

$$= -g(\xi-\eta)\left[\frac{\partial(\xi-\eta)}{\partial x} + \frac{\partial\eta}{\partial x}\right] + \frac{1}{\rho}(\tau^\xi{}_x - \tau^\eta{}_x) \qquad (30)$$

$$\frac{\partial q_y}{\partial t} + \frac{\partial[\beta_y q_y^2/(\xi-\eta)]}{\partial y} + \frac{\partial[\beta_{xy} q_x q_y/(\xi-\eta)]}{\partial x} - v_\xi r$$

$$= -g(\xi-\eta)\left[\frac{\partial(\xi-\eta)}{\partial y} + \frac{\partial\eta}{\partial y}\right] + \frac{1}{\rho}(\tau^\xi{}_y - \tau^\eta{}_y) \qquad (31)$$

where q is the flow rate per unit width, τ^ξ is the shear stress at the free surface, τ^η is the shear stress at the bed surface, and β is the momentum correction factor to account for non-uniformity in the velocity distribution and is expressed as:

$$\beta = \frac{1}{h} \int_0^h \frac{u^2}{\bar{u}^2} \, dz \tag{32}$$

$\bar{u}$ is the vertically averaged velocity. The subscripts x and y are the directional indices. The detailed derivations of equations (29) - (30) are given in Appendix A.

The first two assumptions lead to a vertical hydrostatic pressure distribution for the flow. This is valid if the bed slope is not too steep and there is no abrupt change, e.g., hydraulic jumps or strongly curvilinear flow in a vertical plane, in flow (Henderson, 1966). The third assumption is proved to be valid by the scaling analysis of Sokolov (1973), except at a rigid wall where the horizontal shear may be of equal order of magnitude to the vertical shear.

For laminar flow, the viscous stress dominates and Reynolds' stress can be ignored. The equation for boundary shear stress at the bed is then given by

$$\tau^{\eta}_{x} = \rho \frac{f}{8} \frac{q_x (q_x^2 + q_y^2)^{1/2}}{(\xi-\eta)^2} \tag{33}$$

$$\tau^{\eta}_{y} = \rho \frac{f}{8} \frac{q_y (q_x^2 + q_y^2)^{1/2}}{(\xi-\eta)^2} \tag{34}$$

where f is the flow resistance factor. For laminar flow the flow resistance, f, is defined by the Darcy-Weisbach equation, equation (5) in chapter two.

For turbulent flow Reynolds' stress dominates and viscous stress may be negligible. The boundary shear stress can then be approximated by the Manning equation as

$$\tau^{\eta}_{x} = \rho g \frac{n^2}{(\xi-\eta)^{4/3}} q_x (q_x^2 + q_y^2)^{1/2} \qquad (35)$$

$$\tau^{\eta}_{y} = \rho g \frac{n^2}{(\xi-\eta)^{4/3}} q_y (q_x^2 + q_y^2)^{1/2} \qquad (36)$$

where n is the Manning roughness coefficient.

Both Darcy-Weisbach and Manning equations are derived for steady and uniform flow. Therefore the boundary shear stress equations given above may only be considered as an approximation. The coefficients Ko and n are typically determined by fitting field data, and the two parameters are tabulated in relation to surface conditions in Table 2.2.

The shear stress on the free surface is generally produced by two factors: rain droplets and wind. While the influence of wind on overland flow may be negligible, the impact of rainfall can be significant. As raindrops fall into flowing water, they generate splashing craters on the water surface, and turbulence in the flow. These can cause energy loss and increase flow resistance (Yoon and Wenzel,

1971). The impact is greater for shallow water and laminar flow but less for deep water and turbulent flow. As the water gets deeper and flow gets more turbulent, the impact of rainfall on flow resistance may be negligible (Shen and Li, 1973). Shen and Li (1973) obtained an empirical relationship, equations (7) and (8) in chapter two, between rainfall intensity and Darcy-Weisbach resistance parameter f through a non-linear regression of the results of flume experiments. However, since their empirical study was only for a laboratory flume of very smooth surface, the applicability of the relationship on natural surfaces is very limited.

In this study, a simple description of the relationship between rainfall impact and flow resistance is presented. It assumes that the retardance effect of rainfall is predominantly caused by the momentum exchange between individual rain droplets and flowing water. Rainfall splashing and the effects of spatial interference between individual rain droplets are ignored. When a rain droplet with zero velocity component in the downslope flow direction falls into the layer of overland flow, it will be accelerated by the flowing water in the direction of flow until the moment when its velocity becomes compatible with the velocity of the overland flow. During this process, it is assumed that the rain droplet maintains its

shape. The drag force exerted on the droplet by the flowing water can be expressed as

$$F_{Dx} = \frac{C_D}{2} A_v \rho (u-u_d) |V-V_d| \qquad (37)$$

where F_{Dx} is the component of the drag force acting on the droplet, C_D is the drag coefficient, A_v is the droplet cross-section area projected on a plane normal to the x direction, u_d is the x component of the droplet velocity, V and V_d are the resultant velocities of the flow and the droplet, respectively. On the other hand, the motion of the droplet must obey Newton's second law, i.e.,

$$F_x = \frac{d(m_d u_d)}{dt} \qquad (38)$$

where F_x is the external force acting on the droplet and m_d is the mass of the droplet.

Provided that the slope gradient is small, conservation of momentum for the droplet leads to

$$F_{Dx} = F_x \qquad (39)$$

i.e.

$$\frac{C_D}{2} A_v \rho (u-u_d) |V-V_d| = \frac{d(m_d u_d)}{dt} \qquad (40)$$

integration of the equation with respect to time and for a unit area of the flow field yields the following expression of surface shear stress due to rainfall

$$\tau^{\xi}_{x} = -\rho r \frac{q_x}{(\xi-\eta)} \tag{41}$$

Similarly, the y component shear stress is

$$\tau^{\xi}_{y} = -\rho r \frac{q_y}{(\xi-\eta)} \tag{42}$$

Substitution of the boundary shear stress equations for the water surface and bed surface into equations (29), (30) and (31) produces a closure form of a system of non-linear partial differential equations. For numerical solution, the system of partial differential equations may be written in matrix form

$$\frac{\partial H}{\partial t} + \frac{\partial U}{\partial x} + \frac{\partial V}{\partial y} = E \tag{43}$$

where

$$H = \begin{bmatrix} (\xi - \eta) \\ q_x \\ q_y \end{bmatrix} \tag{43.a}$$

$$U = \begin{bmatrix} q_x \\ \dfrac{\beta_x q_x^2}{(\xi - \eta)} + \dfrac{g}{2}(\xi - \eta)^2 \\ \dfrac{\beta_{xy} q_x q_y}{(\xi - \eta)} \end{bmatrix} \tag{43.b}$$

$$V = \begin{bmatrix} q_y \\ \dfrac{\beta_y q_y^2}{(\xi - \eta)} + \dfrac{g}{2}(\xi - \eta)^2 \\ \dfrac{\beta_{xy} q_x q_y}{(\xi - \eta)} \end{bmatrix} \tag{43.c}$$

$$E = \begin{bmatrix} (r - f) \\ E_1 \\ E_2 \end{bmatrix} \tag{43.d}$$

where E_1 and E_2 are the terms on the right hand sides of equations (30) and (31), respectively.

The model developed above allows an explicit incorporation of spatially variable hillslope features, e.g., infiltration (f), surface roughness (K_o) and microtopography (η). Because of its complexity, this system of partial differential equations has no known analytical solution and may only be solved by numerical methods.

3.3 Numerical Approach

Many numerical models have been developed for describing deep water flow, such as occurs in estuaries and lakes. In these models, a hydrodynamic equation of two or even three dimensions has been solved using numerical methods. However, due to some physical and mathematical difficulties, numerical schemes suitable for deep water flow are not reliable when applied to overland flow. The difficulties result from the following physical phenomena:

1) Overland flow is shallow. It is not uncommon for the depth of overland flow to be less than centimeters or even millimeters. So, a very small magnitude of computational oscillation may result in a negative computed flow depth, causing instability in the numerical solution.

2) For the case of deep water, the bed shear stress is very small in relation to the other fluid forces, so its impact on the stability of the numerical solutions is small. In overland flow the bed shear stress is large in comparison with other forces and often causes some numerical difficulties and instability.

3) Ground surface topography and variation of local slope gradient have significant impact. The vertical amplitude of microtopography is often of the same order of magnitude as or even larger than overland flow depth. Therefore, the surface variation of overland flow is largely dictated by the local slope gradient of microtopography. This strong

dependency of overland flow on microtopography may cause significant disturbance to the overland flow, i.e., regions of rapidly varying flow. This presents a great difficulty for numerical formulation and causes numerical instability for the solution.

4) Rainfall and infiltration represent a significant mathematical "source" and "sink", respectively.

The numerical method used in this study is based on the MacCormack finite-difference scheme, which was developed for simulating aerodynamic problems (MacCormack, 1971). This scheme possesses some advantages over many commonly used schemes in terms of its ability to handle discontinuities and shock waves in the flow. The scheme is an explicit, two-step, finite difference scheme. For each time step, the solution is composed of a sequence of predictor-corrector steps. In the predictor step, the method first obtains an approximate solution at a half time step $t_{n+\frac{1}{2}}$ for the computational point (i,j) using a forward difference for the spatial derivatives. This approximate solution is then modified using a backward difference to get an improved solution for the corrector step at time step $t_{n+\frac{1}{2}}$. These procedures are then repeated to obtain the solution at the second half time step t_{n+1}. To render the solution symmetrical, at the time step t_{n+1} instead of first using a forward difference and then a backward difference, the reverse procedure is followed.

Application of this cyclical procedure to equation (43) yields the following difference equations.

At time t_n:

predictor (backward difference)

$$\bar{H}^{n+\frac{1}{2}}_{i,j} = H^{n}_{i,j} - \frac{\Delta t}{2\Delta x}(U^{n}_{i,j} - U^{n}_{i-1,j}) - \frac{\Delta t}{2\Delta y}(V^{n}_{i,j} - V^{n}_{i,j-1}) + \frac{\Delta t E^{n}_{i,j}}{2} \tag{44}$$

corrector (forward difference)

$$H^{n+\frac{1}{2}}_{i,j} = \frac{1}{2}\left[H^{n}_{i,j} + \bar{H}^{n+\frac{1}{2}}_{i,j} - \frac{\Delta t}{2\Delta x}(\bar{U}^{n+\frac{1}{2}}_{i+1,j} - \bar{U}^{n+\frac{1}{2}}_{i,j}) - \frac{\Delta t}{2\Delta y}(\bar{V}^{n+\frac{1}{2}}_{i,j+1} - \bar{V}^{n+\frac{1}{2}}_{i,j}) + \frac{\Delta t E^{n+\frac{1}{2}}_{i,j}}{2}\right] \tag{45}$$

At time t_{n+1}

predictor (forward difference)

$$\bar{H}^{n+1}_{i,j} = H^{n+\frac{1}{2}}_{i,j} - \frac{\Delta t}{2\Delta x}(U^{n+\frac{1}{2}}_{i+1,j} - U^{n+\frac{1}{2}}_{i,j}) - \frac{\Delta t}{2\Delta y}(V^{n+\frac{1}{2}}_{i,j+1} - V^{n+\frac{1}{2}}_{i,j}) + \frac{\Delta t E^{n+\frac{1}{2}}_{i,j}}{2} \tag{46}$$

corrector (backward difference)

$$H^{n+1}_{i,j} = \frac{1}{2}\left[H^{n+\frac{1}{2}}_{i,j} + \bar{H}^{n+1}_{i,j} - \frac{\Delta t}{2\Delta x}(\bar{U}^{n+1}_{i,j} - \bar{U}^{n+1}_{i-1,j}) - \frac{\Delta t}{2\Delta y}(\bar{V}^{n+1}_{i,j} - \bar{V}^{n+1}_{i,j-1}) + \frac{\Delta t E^{n+1}_{i,j}}{2}\right] \tag{47}$$

where those variables with the overhead bars are obtained from the predictor step and those without the overhead bars are from the corrector step.

It has been shown (MacCormack, 1969) that the scheme is of second-order accuracy in both time and space, although each separate approximation of the predictor and corrector is of first-order accuracy in space. While the numerical properties of the scheme have not been completely analyzed in the general non-linear form, the convergence and stability properties of the scheme for the linearized set of the equations have been studied by MacCormack (1971). The Courant-Friedrich-Lewry (CFL) stability condition for the linearized equation is

$$\Delta t = C_n \left[\frac{u_{max}}{\Delta x} + \frac{v_{max}}{\Delta y} + c\left[\frac{1}{\Delta x^2} + \frac{1}{\Delta y^2} \right]^{1/2} \right]^{-1} \qquad (48)$$

where C_n is the desired Courant number and c is the wave celerity, defined as $c = (gh)^{\frac{1}{2}}$. A von Neumann stability analysis by Anderson et al. (1984) showed that the scheme was stable when $C_n \leq 1$. However, it is important to note that a difference scheme shown to be stable by linear analysis may still experience numerical instability in the solution of non-linear problems. In fact, as demonstrated by the examples presented later in this chapter, the stability condition for non-linear equation (43) is far more restrictive than that provided by Anderson et al.

3.4 Boundary and Initial Conditions

Finite-difference equations (44) - (47) give the solutions for the interior nodes. The solutions at the boundary nodes, however, require special treatment. Two kinds of boundary conditions were considered in this study: closed boundary and open boundary. At a closed boundary, both the normal and tangential velocities vanish because of the no-penetration and no-slip conditions. Therefore, the mathematical expressions at closed boundaries can be expressed as

$$q_x(t) = 0 \tag{49}$$

$$q_y(t) = 0 \tag{50}$$

The water depth at this boundary fluctuates depending on the flow inside the boundary. At an open boundary, the proper boundary conditions are described by Brutsaert (1971), Liggett and Woolhiser (1967), Verboom et al. (1982) and Lai (1986). If flow immediately upslope from the boundary is subcritical, one condition, critical flow, may be defined at the boundary

$$h_c = [(q_x^2 + q_y^2)/g]^{1/3} \tag{51}$$

where, h_c is the critical depth of the flow. If flow immediately upslope from the boundary is supercritical, no boundary condition is required. For unsteady overland

flow, the specified boundary conditions may change during the solution if the flow changes from subcritical to supercritical or vice versa.

Discussions of the numerical approximation of the boundary conditions for overland flow can be found in the literature of Liggett and Woolhiser (1967) and Liggett and Cunge (1975). These studies concluded that the characteristic method was the most accurate method for approximating the boundary conditions. Unfortunately, the characteristic method is too complicated to be used in a two-dimensional model, especially with spatially varying hillslope features. Therefore, simpler approximation schemes were used in this model and are discussed below.

At a closed boundary, the flow depths are approximated by an inward difference, which may be a forward or a backward difference, while the discharge at the boundary is specified as zero as mentioned above. At an open boundary, if the flow is subcritical, the discharge is determined by an inward difference and the depth is then determined by equation (50). If the flow is supercritical, both the discharge and depth are computed by an inward difference.

Field studies of overland flow are usually carried out on experimental plots of rectangular shape. For this case, the closed boundary is the border and the open boundary is the downslope boundary of the plot. The model

simulations discussed in the next chapter are for overland flow on such experimental plots. While all the boundary conditions for the experimental plots can be solved using the above described procedures, the author found that for a rectangular plot where the flow is predominantly downslope, the following approximation for the upper boundary condition will improve the stability of the solution. In this case, the computational boundary is not defined at the physical boundary but a small distance, D, downslope from it. Therefore, instead of using zero discharge at x = 0, a non-zero discharge at x = D, which is solely contributed by the lateral inflow from the length of D and obtained using the steady state kinematic wave equation, is used as the upslope boundary condition. Numerical experiments showed that this approximation for the upper boundary condition damped some computation oscillations near the upslope boundary, thus providing more stable solutions than if a zero discharge were to be used at the boundary. Since the values of D used are small, typically, 1 to 2 cm, its influence on the simulation results is negligible.

If overland flow initially starts on a dry slope surface, the initial conditions at the beginning of rainfall excess are defined throughout the domain as

$$h(t=0) = 0 \qquad (52)$$

$$q_x(t=0) = 0 \tag{53}$$

$$q_y(t=0) = 0 \tag{54}$$

The condition of zero depth induces a mathematical singularity at the beginning of the computation. Therefore, to start the computation, a thin film of water is assumed to be ponded prior to the initiation of overland flow. This assumption has been used by, e.g., Liggett and Woolhiser (1967), Brutsaert (1971) and Chow and Ben-Zvi (1973). The depth of this initial layer of water in the simulations, h_a, was small, less than one tenth of the average depth at steady state. The time required to build up this initial depth, t_a, is determined by the kinematic wave approximation, $t_a = h_a/(r-f)$, and is only a small fraction of the time required for hydrographs to reach steady state. This starting procedure allows the numerical solution of the hydrodynamic equation to begin at time $t = t_a$ where non-zero depths are known.

3.5 Limitations of the Model

The limitations of the hydrodynamic and numerical model (HyNuM) are the following.

1) The entire physical domain is flooded and there are no free boundaries. The model may not be applied to the cases where topographic heights protrude of the flow and where there are large patchy areas where the infiltration rate exceeds the rainfall rate. This approximation is

acceptable for the cases where hillslope surfaces are relatively smooth, e.g., many old landscape hillslopes and hillslopes with surface soils formed with fine parent materials in arid and semi-arid regions, and where rainfall intensities exceed infiltration rates.

2) At this state of development, only the spatial variation of steady infiltration rate, i.e., the saturated hydraulic conductivity, is considered, and unsteady infiltration is not allowed. As shown in Figure 2.2, during a rainstorm event, infiltration rate for most of soils reaches a more or less constant rate within a very short time period, generally less than 30 minutes, and the rainfall durations are usually much longer than the time necessary for infiltration to reach the more or less constant rate. Therefore, this approximation is acceptable for many rainfall overland flow cases, and especially, for the cases where the soil infiltration capacity is small and where the hillslope surfaces are previously wet before a rain storm or for overland flow during heavy rain storms.

3) The ground change with time due to soil erosion or deposition during a rainfall event is negligible.

4) Microtopography, infiltration, and surface roughness on a natural hillslope usually vary over distances of centimeters to meters. To resolve such a fine scale, the computational grid mesh must be even smaller. Due to the

enormous computation intensity and some stability requirements of the model, with the very small grid scale, the model simulation may be limited to a small area, e.g., a length scale less than 100 meters. For simulations on a hillslope with a scale larger than that, it is necessary to increase the computational grid scale. This may result in a poor representation of the spatial variations of hillslope features.

3.6 Model Comparisons and Tests

To evaluate the accuracy and application of the model, two sample problems were solved. The first example is for overland flow on a one-dimensional plane surface, for which the hydrodynamic equation has been solved numerically using the characteristic formulation and is shown to be very accurate (Liggett and Woolhiser, 1967). This example is necessarily simple, and was chosen to test the accuracy of the hydrodynamic model. In the second example, the case of overland flow on a three-plane cascade is simulated to test the model against experimental measurements and to show the model's shock-capturing ability. For this case model results and experimental results are compared. Model simulations for two-dimensional overland flow due to spatial variations in infiltration, surface roughness and microtopography will be presented in the next chapter.

Example 1: One-Dimensional Smooth Plane

Runoff hydrographs on a smooth impermeable plane are simulated using HyNuM, the characteristic method of Woolhiser and Liggett, and the KWE. The results are shown in Figure 3.2. These results were computed for the case defined by the following conditions:

total length of the plane:	L_o = 12 m
slope gradient:	So = 0.0936%
roughness parameter:	Ko = 24
rainfall intensity:	r = 10 cm/hr
kinematic wave number:	k = 1
Froude number:	F_o = 2

where k and F_o are defined in equations (15) and (16), respectively. The computation grid was take as Δx = 1.0 m, the time increment was Δt = 0.12 s, and the value of C_n was 0.799.

The results show that the agreement between HyNum and the characteristic solution is very good. Since the kinematic wave number k is much less than 10 for this case, the solution by the KWE is not satisfactory.

Example 2: Three-Plane Cascade

In the second example, the model was run on a three-plane cascade surface, which is described in Iwagaki's experiments (Iwagaki, 1955). Iwagaki conducted a series of rainfall runoff experiments in a laboratory flume, which

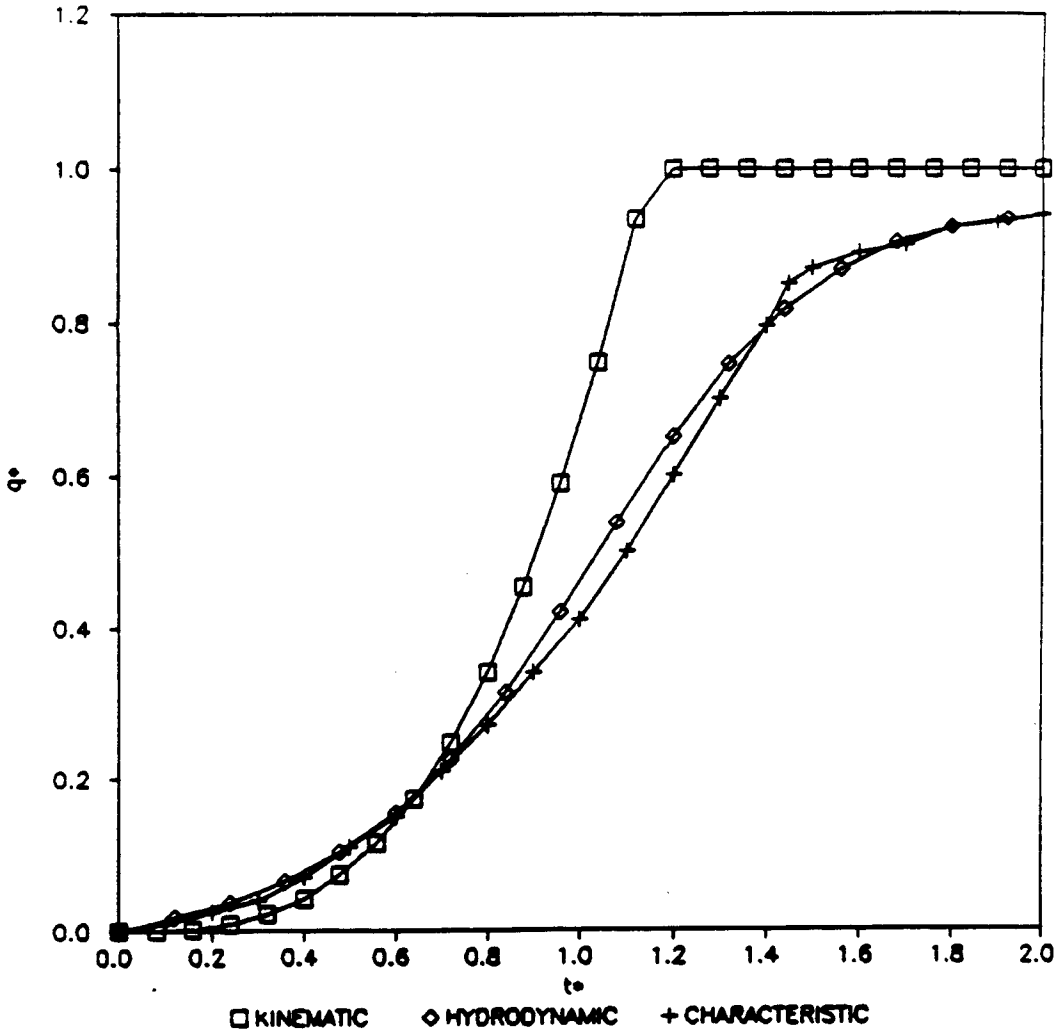

Figure 3.2 Comparison of the solution by the hydrodynamic model with the characteristic (Woolhiser and Liggett, 1967) and kinematic solutions for the Froude number $F_o = 2$ and the kinematic number $k = 1$. Dimensionless time $t^* = t\, u_o/L_o$; dimensionless discharge $q^* = q/(r\, L_o)$.

was made of aluminum plate which was very smooth. The flume, 24 meters long, was divided into three sections of equal length. Each section had a different slope. They were, from the upslope end to the downslope end, 0.020, 0.015 and 0.010, respectively. During the experiments, three different rainfall intensities of 389 cm/hr, 230 cm/hr and 288 cm/hr were simultaneously applied to the upper, middle and lower sections. The durations of the rainfall (t_r) for three different experimental runs were 10, 20 and 30 seconds. Under these flow conditions, it was observed that regions of rapidly varying flow were generated. These regions of rapidly varying flow were caused by faster upstream flow, which resulted from heavier rainfall input and a steeper slope, catching the slower downstream flow, which resulted from less intense rainfall and a smaller slope gradient.

In the computation, the spatial increment was taken as $\Delta x = 1.0$ m, the time increments for stable solution were $\Delta t = 0.012$ s for rainfall durations of 10 and 20 seconds and $\Delta t = 0.006$ s for rainfall duration of 30 seconds. The values of Cn are less than 0.2. From the results the calibrated Manning coefficient, $n = 0.006$, was obtained. The flow depth profiles computed by HyNuM show good agreement with those given by Iwagaki (Figure 3.3), although the water profiles computed by HyNum are slightly deeper than those of Iwagaki and have small computational

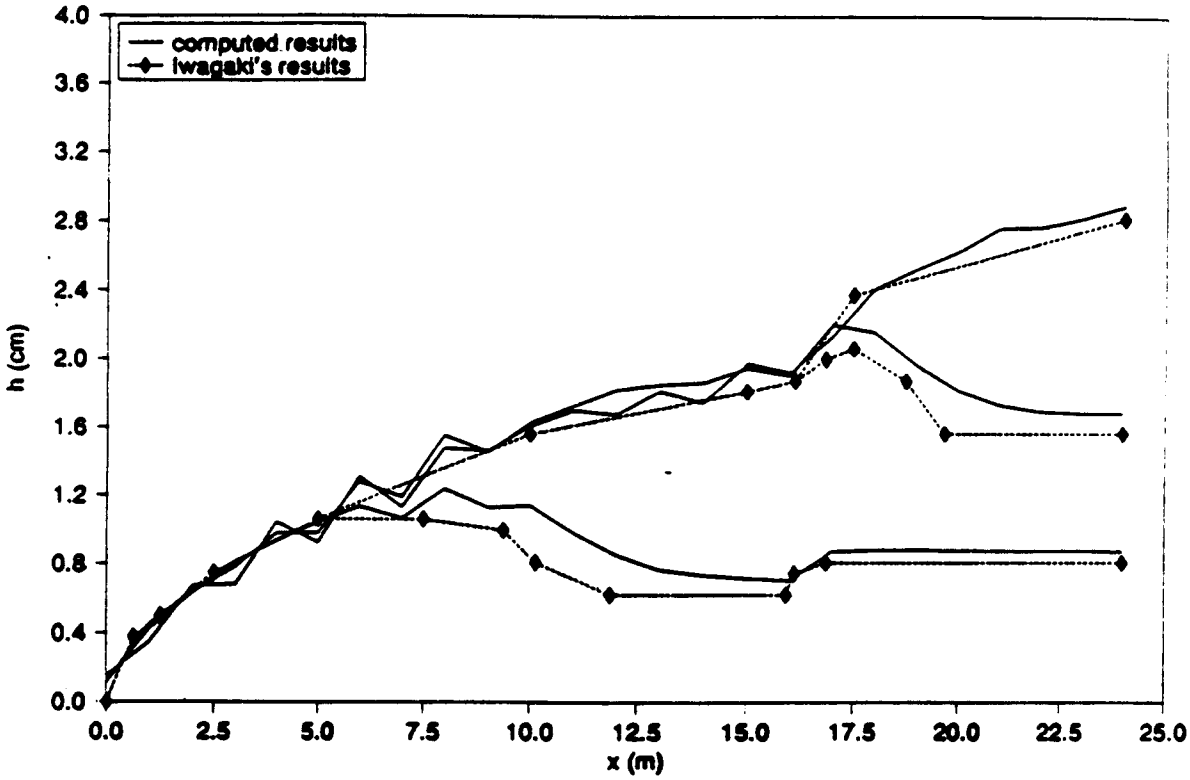

Figure 3.3 Comparison of the computed depth profiles at the cessation of rainfall on a three-plane cascade from the hydrodynamic model with Iwagaki's results (Iwagaki, 1955).

oscillations.

The computed hydrographs by both HyNuM and the kinematic shock fitting model (Borah et al., 1980) are compared with the experimental results of Iwagaki are shown in Figure 3.4. The model simulation was good for the cases with rainfall durations of 20 and 30 seconds, but not so good for rainfall duration of 10 seconds. From Figure 3.4 one can see that after rain stopped at 10 seconds the measured discharge slowly increased for about 5 seconds, then maintained a constant flow rate of approximately 26 cm^2/s for about 8 second, and then drastically rose to 75 cm^2/s at about 25 seconds, i.e., 15 seconds after the rainfall stopped. This drastically increased discharge at 15 seconds after cessation of rainfall was caused by the arrival of the upstream flood generated by a much heavier rainfall on the upstream segment. For the computed hydrograph and rainfall duration of 10 seconds, the timing of the discharge peak was delayed by about 5 seconds and the sharpness of the peak was reduced. These may be caused by the effects of damping and phase error of the numerical solution. Also, in Figure 3.4a the hydrodynamic solution shows a slight rise toward the end of the hydrograph. This shows a sign of the beginning of the numerical ocsillations. In general, the results show that the computed hydrographs by HyNum, especially, the non-equilibrium hydrographs, are in closer

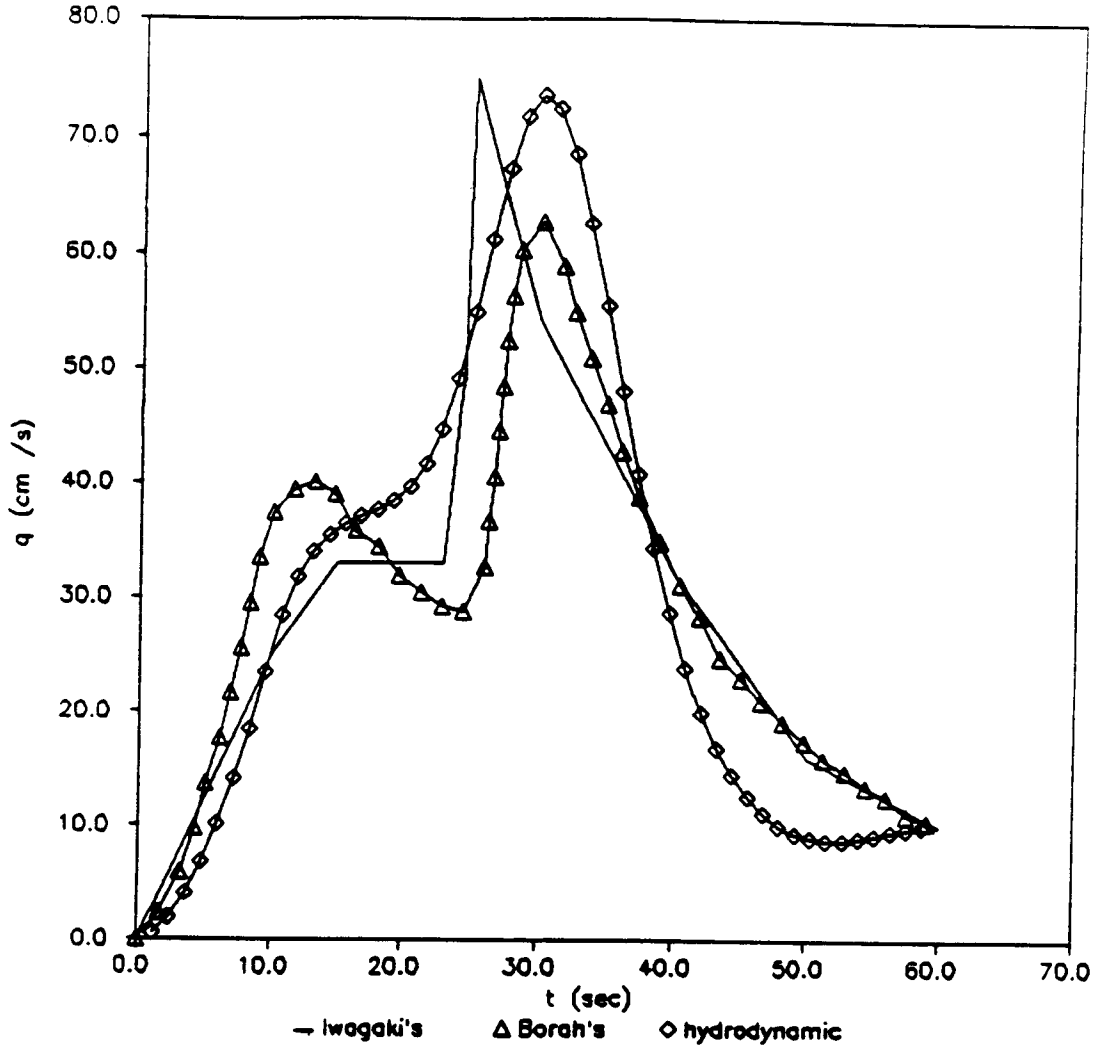

Figure 3.4 Comparison of the computed hydrographs on a three-plane cascade from the hydrodynamic model and kinematic shock-fitting model (Borah et al., 1980) with Iwagaki's results.
a) t_r = 10 seconds

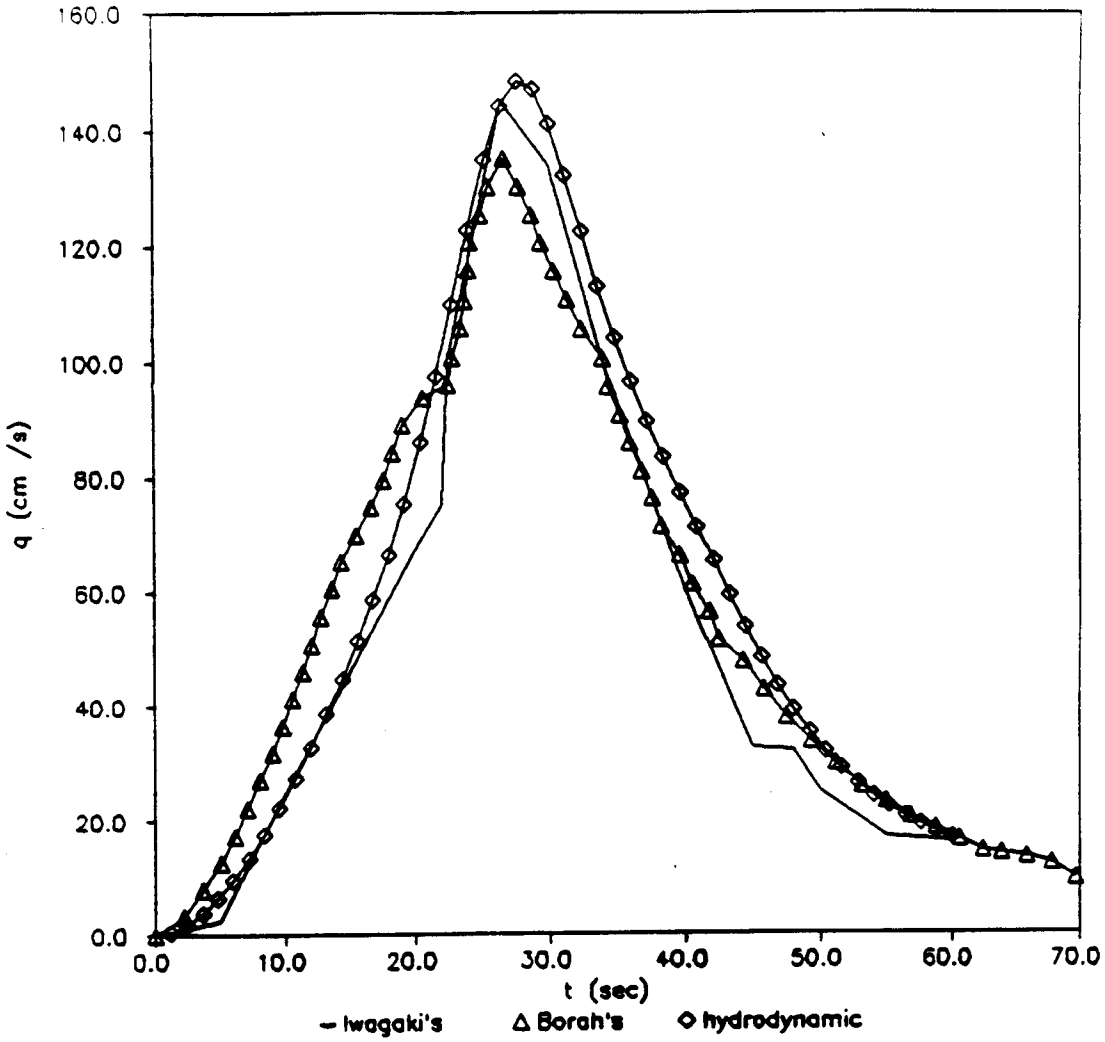

Figure 3.4 continued.
b) t_r = 20 seconds

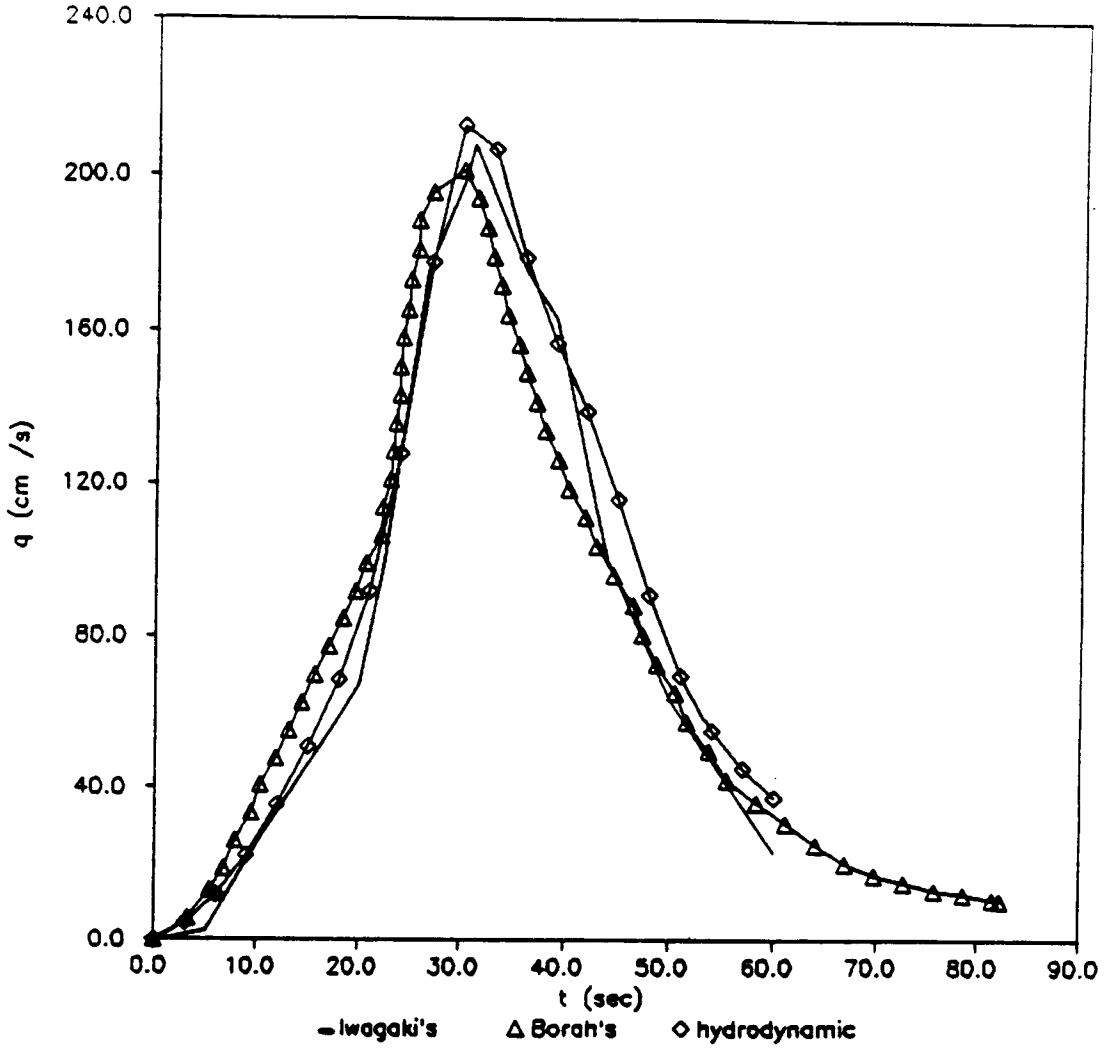

Figure 3.4 continued.
c) t_r = 30 seconds

agreement with Iwagaki's results than those computed with the kinematic shock fitting model.

3.7 Summary

A two-dimensional hydrodynamic and numerical model (HyNuM) for overland flow has been presented. The model allows explicit incorporation of spatial variations in some hillslope physical characteristics, which may be surface roughness, infiltration, and microtopography. The accuracy of the model has been tested by comparison with a characteristic solution and experimental data. The shock-capturing ability of the model has been tested using a plane-cascade surface with a non-uniform rainfall intensity. The results of these tests indicate that the model has good stability and convergence properties. The results of the tests presented in this study show promise. The model can be used to illustrate the influence of the spatial varying surface roughness, infiltration and microtopography on overland flow characteristics including distributions of flow depth and velocity and hydrographs. These simulations and the discussion of the impacts of these spatial variations on the characteristics of overland flow will be given in the next chapter.

Chapter Four

EFFECTS OF HILLSLOPE SPATIAL VARIATIONS ON OVERLAND FLOW

4.1 Review of Previous Work

The spatial variations of hillslope characteristics considered in this study include soil infiltration, surface roughness and microtopography. These variations have strong effects on overland flow. Previous studies have mostly emphasized spatial variation of infiltration and its effects on the hydrograph. Little attention has been paid to the effects of spatial variations of surface roughness and microtopography, and no attempt has been made to relate these spatial variations to measurable characteristics of overland flow.

The study by Wu et al. (1978) is one of a few studies that dealt with the effects of spatial variation of surface roughness on the hydrographs of overland flow. In their study, the effects of spatial variations of surface roughness were investigated for the surfaces consisting of two roughness elements: a butyl surface and a gravel surface. The value of K_o for a butyl surface is in the range of 24-50 and the value for a gravel surface in the range of 300-400. Physical experiments were conducted for rainfall runoff on the surfaces with different combinations of the two roughness elements and the overland flow hydrographs were recorded. The KWE was used

to reproduce the observed results by assuming a uniform surface with the equivalent uniform roughness (EUR) optimized from the observed results. The results suggested that the concept of EUR for a surface with nonuniform roughness distribution may be applied if the different roughness sub-areas are small in comparison with the total runoff area and uniformly and randomly distributed. However, for the case where the size of roughness elements is sufficiently large or not uniformly and randomly distributed, the computed hydrographs by the KWE using the optimized EURs deviated greatly from those observed. For this case, overland flow does not behave as if it is from a uniform surface, and, therefore, no EUR can be obtained for the KWE.

Smith and Hebbert (1979) conducted a study on the hydrologic effects of spatial variability of infiltration. In the study, Monte Carlo simulation was employed to analyze the effects of random distribution of soil infiltration properties on the hydrologic response of a hillslope. A distributed simulation model, consisting of the KWE and infiltration model by Smith and Parlange (1978), was used to demonstrate hydrograph bias due to deterministic and random variation of soil saturated hydraulic conductivity K_s. They found that as K_s decreased toward the downslope boundary, runoff decreased compared to the case where K_s increased downslope. Runon from an

upslope area with lower infiltration rate causes ponding with very little loss of volume was responsible for the higher runoff on surfaces with K_s increasing downslope. The opposite case allowed no such interaction. These results were obtained for cases where rainfall intensity was much larger than (7 to 14 times) saturated hydraulic conductivity.

Freeze (1980) used a stochastic-conceptual mathematical model of runoff processes on a hillslope to investigate the influence of the spatial properties of hillslope parameters on the statistical properties of the resulting runoff. The model used the method of Smith and Parlange (1978) to generate excess rainfall. The excess rainfall was then routed as overland flow by a simple travel time approach, in which the travel time of runoff from individual grids to the downslope boundary was randomly assigned, and the interaction of grids was ignored. In the model, the distribution of saturated hydraulic conductivity on a hillslope was viewed as a spatial stochastic process and represented by a log-normal probability density function with three parameters: distribution mean, standard deviation and spatial autocorrelation. The results indicated that each of these parameters exerts an influence on statistical properties of hillslope runoff. The distribution mean value is the most important parameter; the standard deviation is next

important; the autocorrelation is least important. Loague (1988) also investigated the effect of spatial variability on hillslope runoff by this stochastic-conceptual approach and showed that saturated hydraulic conductivity had a greater impact on the characteristics of hydrograph than other hillslope and rainfall properties.

Matias and Correia (1987) used a conceptual and deterministic rainfall runoff model in a Monte Carlo simulation to analyze the influence of the spatial variability of the saturated hydraulic conductivity on flow hydrographs. The rainfall excess rate was determined from the computations of infiltration, ponding and redistribution of water in the soil, based on the two-phase infiltration model by Morel-Seytoux (1978, 1982). Then the surface detention water was routed downslope as overland flow by a unit hydrograph approach. The saturated hydraulic conductivity in the study was defined by a log-normal probability distribution function. It was concluded that both the coefficient of variation and skewness of the spatially distributed saturated hydraulic conductivity have strong influence on the runoff hydrographs. The coefficient of variation is more important than the skewness. The effect of both parameters was attenuated with the increase of rainfall intensity.

Woolhiser and Goodrich (1988) used the a simple physical rainfall runoff model to study the impact of

rainfall intensity patterns and saturated hydraulic conductivity on overland flow. In their model, infiltration and excess rainfall were determined by the Smith and Parlange (1978) model and overland flow was routed by the KWE. Spatial variability of saturated hydraulic conductivity was represented in only the cross-slope strips. With the simple one-dimensional representation of spatial variability, the study was able to show the impact of the interaction of rainfall and soil hydraulic conductivity on overland hydrographs. Under heavy rainfall, more runoff was generated from a uniform surface with the mean value of the hydraulic conductivity distribution than that from a surface with spatial variable hydraulic conductivity. This is true until the rainfall intensity reduces to a certain value, under which more runoff is generated from a spatially variable surface and less or no runoff is generated from the uniform surface. These studies shed new light on the role of the spatial variability of infiltration and its interaction with rainfall input in determining the response of hillslope overland flow.

All these studies contribute to our understanding of the effects of hillslope spatial variations on the response of overland flow. However, because the overland flow models used in these previous studies are either based on empirical methods, e.g., those of Freeze (1980),

Matias and Correria (1987) and Loague (1988), or the one-dimensional KWE model, such as those by Wu et al. (1978), Smith and Hebbert (1979), and Woolhiser and Goodrich (1988), they were not able to incorporate realistic two-dimensional hillslope features into the models, and therefore, to examine the characteristics of overland flow, including variability of flow fields due to two-dimensional variability of hillslope properties.

4.2 Research Objectives

In this chapter, the effects of two-dimensional spatial variations in infiltration, surface roughness and microtopography on the characteristics of overland flow will be examined using the detailed simulations from HyNuM. I will examine the effects of the spatially variable hillslope properties on the characteristics of flow fields and hydrographs of overland flow. The results of the detailed simulation will be used to identify the role and relative importance of each spatial variable on the characteristics of overland flow. The analysis will address the sensitivity and variability of the flow fields and hydrographs, due to the scales of the variability of each hillslope variables, thus suggesting useful measures of hillslope characteristics for hydrological prediction.

During prediction of hydrographs using the KWE, the spatial variations of soil hydraulic conductivity, K_s,

surface roughness, K_o, and the variable microtopography are often ignored and represented by their mean values. Therefore, it is important and necessary to study the prediction bias caused in hydrographs by the approximation of spatially variable hillslopes by homogeneous plane surfaces.

The specific tasks to be carried out are:

(1) To generate a series of spatially variable fields for infiltration and surface roughness based on field measured and hypothetical random distributions, trending variation functions, and functions of trending variation with embedded randomness. For microtopography, a two-dimensional cosine-wave function will be used to generate a series of two-dimensional corrugated microtopographic surfaces. In addition, two microtopographic surfaces from Kenya savanna hillslopes measured by Aubry (1984) will be used for simulation.

(2) To use HyNuM to conduct systematic model simulations of overland flow on surfaces with spatially variable infiltration, surface roughness and microtopography provided in task (1). The simulation results will include detailed two-dimensional flow fields and hydrographs.

(3) To examine the effects of the spatial variations of infiltration, surface roughness and microtopography on the characteristics of overland flow using the results of

the detailed model simulations given in task (2). The conclusions about the effects of these variations for infiltration and surface roughness on the characteristics of overland flow, including the variability of the two-dimensional flow fields and hydrographs, will be drawn in terms of their statistical properties. The effects of microtopography on the characteristics of overland flow will be analyzed in terms the characteristic scales of the microtopography, e.g., the ratio of the vertical amplitude to the wave length of a consecutive topographic heights and depressions. The simulation results from the two natural microtopographic surfaces will also be analyzed to compare with the results from the hypothetical microtopographic surfaces.

(4) To examine the bias in predicting hydrographs due to the approximation of spatially variable hillslopes by homogeneous plane surfaces. To achieve this, the overland flow hydrographs will be generated using the KWE with the mean values of saturated hydraulic conductivity, surface roughness and mean slope gradient in place of the spatially variable saturated hydraulic conductivity, surface roughness and microtopography. The comparison of the hydrographs from the spatially variable surfaces using HyNuM with those computed from homogeneous plane surfaces with the KWE will be presented.

4.3 Representations of Hillslope Spatial Variations

4.3.1 Spatial Variation of Infiltration

For infiltration, the model simulations will ignore unsteady infiltration and only steady infiltration will be considered. Steady infiltration is represented by the saturated hydraulic conductivity, K_s.

Field studies have shown that saturated hydraulic conductivity on a hillslope varies significantly in space. While most studies indicate the spatial variation of saturated hydraulic conductivity to be a random process, some, e.g, Freeze and Cherry (1979), Smith and Hebbert (1979) and Grah et al. (1983), suggest that there may be a gradation of hydraulic properties through hillslope soil formation, thus resulting in a deterministic or trending variation. For example, the saturated hydraulic conductivity may have a downslope trending variation according to the downslope trending variation of soil textures which may be caused by the preferential sediment transport on hillslopes. On a hillslope, more complex patterns may exist, for example, the randomness may be embedded in systematic trends. In this section, the three variation patterns, random, trending, and trending with embedded randomness, will be studied.

Random variation: The saturated hydraulic conductivity K_s is usually thought to be log-normally distributed (see

Table 1 for summary of evidence) and may be described by the following function

$$Y = Ln(K_s) \tag{55}$$

$$Y \sim N(\mu_Y, \sigma_Y) \tag{56}$$

where Y is the log-arithmically transformed variate of K_s and distributed according to a normal probability distribution function, μ_Y is the mean of the transformed variate and σ_Y is the standard deviation of transformed variate. The mean μ_{Ks} and standard deviation σ_{Ks} for the arithmetic scale of Ks are related to the transformed parameters by

$$\mu_{Ks} = \exp(\mu_Y + \frac{1}{2}\sigma_Y^2) \tag{57}$$

$$\sigma_{Ks} = \exp(2\mu_Y+\sigma_Y^2)(\exp(\sigma_Y^2)-1) \tag{58}$$

Runoff from a plane 50 meters long and 10 meters wide was simulated based on a 1 meter by 1 meter spacing grid for a total of 561 grid points. The values of K_s are generated from the log-normal probability density function and randomly assigned to each of the 561 grid points on the plane. Three random variation patterns of K_s are generated from the log-normal distribution function based on three different values of σ_{Ks}. The combinations of the different variation patterns of K_s with spatially constant

slope gradients (S_x), surface roughness, and rainfall intensities are shown in Table B.1 (Appendix B).

Trending variation: Trending variation of saturated hydraulic conductivity may exist in either cross-slope or downslope directions. However, hillslope soil catena and vegetation distribution are more likely to result in trending variations of saturated hydraulic conductivity in the downslope direction than in the cross slope direction. In this study, trending variation in the downslope direction will be considered.

Downslope trending variations may take a variety of different forms. For the purpose of simulation, it is sufficient to examine the effects of trending variation of K_s using a linear variation. A similar linear variation of Ks was used by Smith and Hebbert (1979). The downslope trending variation is assumed to have the following form:

$$K_s = K_s^U + G\ x \qquad (59)$$

where K_s^U is the saturated hydraulic conductivity at the upper boundary of the plane, x is the downslope distance from the upper boundary, and G is the gradient of the variation and defined as

$$G = \frac{K_s^L - K_s^U}{L_o} \qquad (60)$$

where K_s^L is the saturated hydraulic conductivity at the lower boundary of the plane, and L_o is the total length of the slope. For the downslope increasing case, K_s^L is greater than K_s^U and G takes a positive value; for the downslope decreasing case, K_s^L is less than K_s^U and G takes a negative value.

Different variation patterns of K_s are generated and the combinations of these trending variations of K_s with spatially constant slope gradient, surface roughness and rainfall intensity are shown in Table B.2.

Trending variation with embedded randomness: The spatial variation of K_s for this case is composed of two parts and expressed by the following form

$$K_s = (K_s^U + G x) + \delta \qquad (61)$$

The first two terms represent a deterministic trend of linear variation in downslope direction. The term, δ, represents a random variation. For simplicity, it is assumed that δ is varied according to a uniform random distribution with mean μ_{Ks} and standard deviation σ_{Ks}. From the equation, the values of K_s are generated and assigned to each of the 561 grid points on a plane 50 meters long and 10 meters wide. Table B.3 lists the cases used for the simulation.

4.3.2 Spatial Variation of Surface Roughness

Spatial variation of surface roughness has been frequently observed in the field (e.g., Aubry, 1984), but has not been rigorously studied and summarized. For the purpose of parameter study, it is assumed that surface roughness also has random and trending variations and combinations of the two. The three spatial variations will be simulated for surface roughness.

Random variation: Due to lack of field knowledge about the nature of the spatial variation of the surface roughness on a hillslope surface, the specific distributions of hillslope surface roughness remain unknown. It is assumed in this study that the spatial variation of surface roughness is distributed according to a uniform probability distribution function, i.e.,

$$K_o = K_{omin} + (K_{omax} - K_{omin})\ \delta \qquad (62)$$

where K_{omin} is the minimum value of Ko, Ko_{max} is the maximum value of K_o, and δ is a random variable having a uniform (0,1) distribution. The mean, μ_{Ko}, and standard deviation, σ_{Ko}, for the function are

$$\mu_{Ko} = \frac{K_{omax} - K_{omin}}{2} \qquad (63)$$

$$\sigma_{Ko} = \frac{K_{omax} - K_{omin}}{\sqrt{12}} \qquad (64)$$

The random fields of surface roughness are generated on a 50 by 10 meter plane in the same way as those of randomly varying saturated hydraulic conductivity. Six random variation patterns of K_o are generated for model simulation, based on two different values of the distribution means, μ_{Ko}, and three different values of standard deviation, σ_{Ko}. Table B.4 shows the list of different combinations of these spatially variable roughness fields with other variables.

Trending variation: The effect of trending variation for surface roughness may again be sufficiently demonstrated by assuming the linear variation in both increasing and decreasing directions of the slope. Similar to the trending variation of saturated hydraulic conductivity, linear variation of surface roughness may be expressed by the following function:

$$K_o = K_o^U + G\ x \qquad (65)$$

where K_o^U is the surface roughness at the upper boundary of the plane, G is the gradient of the variation in surface roughness and is defined as

$$G = \frac{K_o^L - K_o^U}{L_o} \qquad (66)$$

where K_o^L is the saturated hydraulic conductivity at the lower boundary of the plane. For the downslope increasing case, K_o^L is greater than K_o^U and G takes positive values; for the downslope decreasing case, K_o^L is less than K_o^U and G takes negative values. Several trending variation surfaces are produced from equation (65). The cases for model simulation are listed in Table B.5.

Trending variation with embedded randomness: Similar to the cases of variable infiltration, it also assumed that surface roughness, K_o, is composed of two kinds of variations, a linear downslope trending variation and a uniform random variation, i.e.,

$$K_o = (K_o^U + G\ x) + \delta \qquad (67)$$

where δ is the uniform random distribution with mean μ_{Ko} and standard deviation σ_{Ko}. The variation fields of K_o are generated in the same way as those of K_s. The cases in Table B.6 are used for the simulation.

4.3.3 Hillslope Microtopography

Patterns of hillslope microtopography have been measured and the effects of the microtopography on the characteristics of overland flow have been studied (Emmett, 1970 and Aubry, 1984). These studies on experimental plots on hillslopes demonstrated the significant effects of microtopography on overland flow.

However, it is difficult to quantify and generalize these effects as functions of the characteristics of microtopography using natural hillslope microtopography, since observed microtopographic patterns of natural hillslopes are often very complicate and vary greatly from hillslope to hillslope and from region to region.

To quantify and generalize the microtopographic effect, a systematic representation or parameterization of microtopography of hillslopes is necessary. In this study, it is assumed that the microtopographic patterns may be approximated by the two-dimensional corrugated surface defined by the following mathematical function

$$Z = Z_o - xS_x - yS_y + a_x\cos(2\pi x/\lambda_x) + a_y\cos(2\pi y/\lambda_y) \qquad (68)$$

where Z is the ground surface elevation, Z_o is the ground surface elevation of the upper boundary, S is the slope gradient, a is the variable defining the amplitude of microtopography and λ is the wave length of micro-topography. The subscripts x and y index the downslope and cross-slope directions, respectively. This function emphasizes the roles of the vertical amplitude, expressed as $\epsilon = 2(a_x+a_y)$, and lateral extent of topographic perturbations which are represented by simple trigonometric waves with wave length of λ_x and λ_y. From the equation, different forms of microtopography may be generated according to the combinations of different

values of a_x, a_y, λ_x, λ_y, S_x and S_y. Two typical microtopographic surfaces are shown in Figure 4.1.

The effects of the microtopography generated from equation (68) can be examined by systematically varying each of the parameters. The microtopographic patterns, hillslope variables, and rainfall intensities used for model simulations are listed in Table B.7.

In addition to these hypothetical microtopographic surfaces, model simulations are performed for the observed microtopographic surfaces shown in Figure 4.2. These surfaces were measured by Aubry (1984) from Kenya Savanna hillslopes.

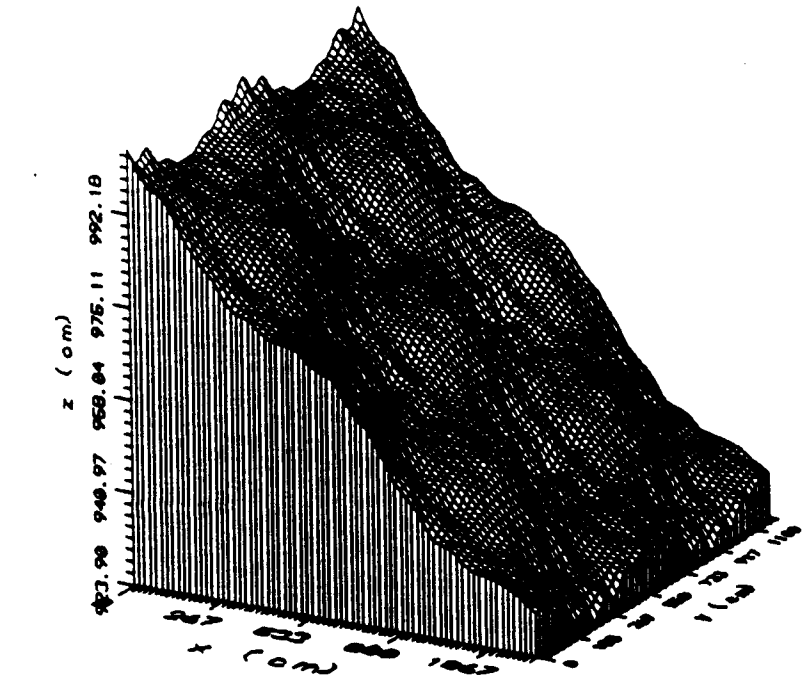

Lo=1200cm; Sx=5%; λx=600cm; λy=600cm; ϵ=6cm

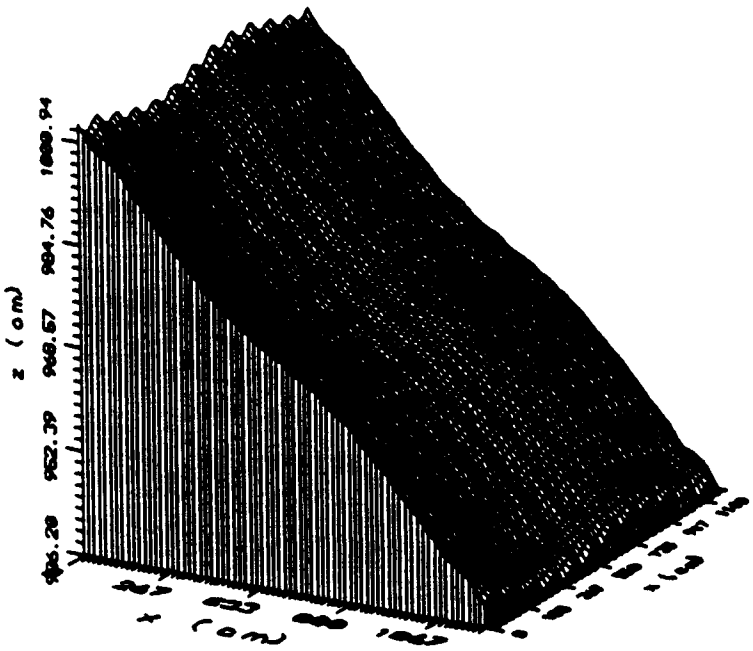

Lo=1200cm; Sx=5%; λx=1200cm; λy=1200cm; ϵ=6cm

Figure 4.1 Typical two-dimensional corrugated microtopographic surfaces generated by equation (68).

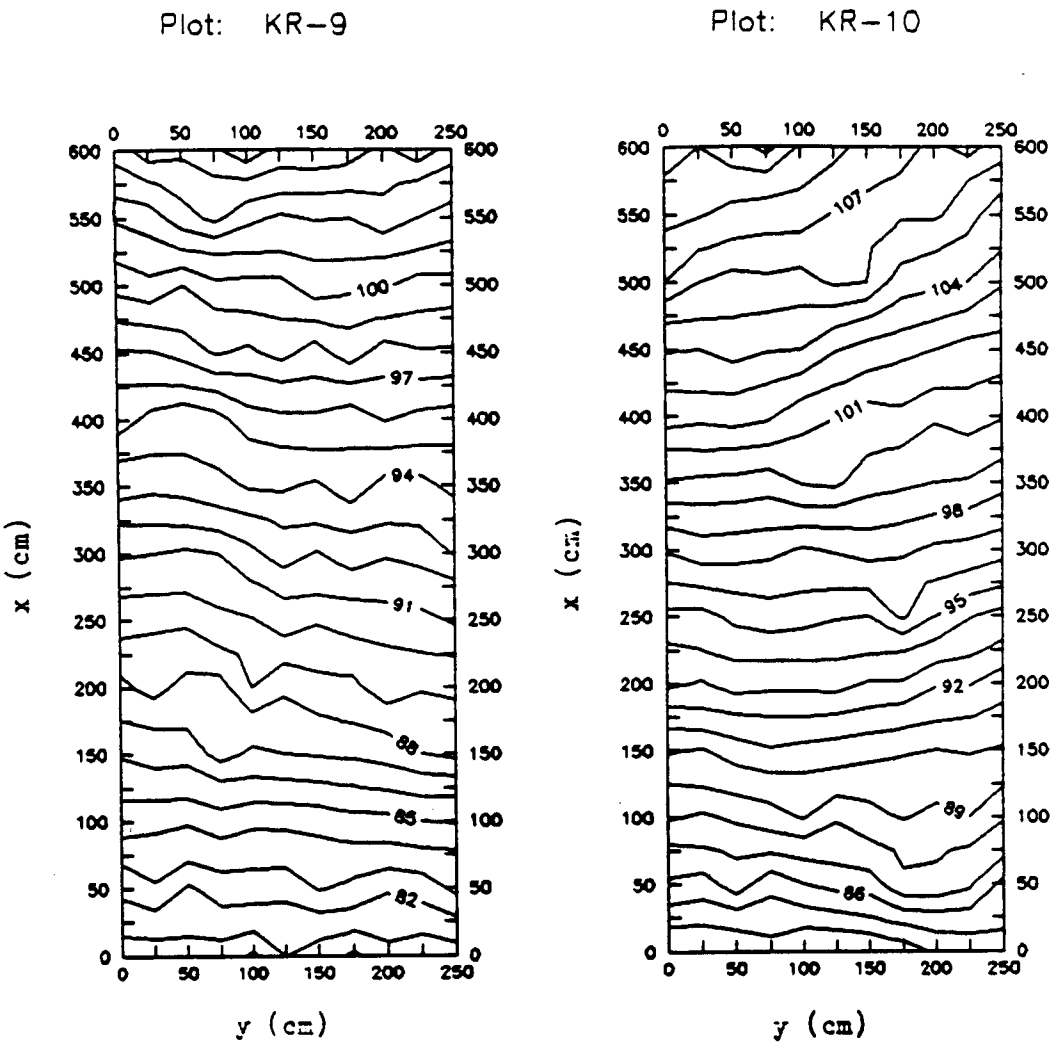

Figure 4.2 Microtopographic maps surveyed by Aubry (1985). The contour lines represent surface elevation in cm.

4.4 Analysis of the Simulation Results

In this section, the responses of overland flow from slope surfaces with spatially varying infiltration, surface roughness and microtopography are simulated using HyNuM. The cases simulated were given in Tables B.1 to B.7. Based on the simulation results, the effects of the spatial variation in infiltration, surface roughness and microtopography on the characteristics of overland flow along the flow paths and the characteristics of runoff hydrographs at the bottom of hillslopes will be analyzed. These cases are also simulated by the KWE from the corresponding homogeneous plane surfaces with the mean values of the hillslope properties, and the comparisons of overland flow fields and hydrographs from both the variables and homogeneous surfaces are presented.

4.4.1 Effects of Spatially Varying Infiltration

1) Effects of random variation

The cases listed in Table B.1 are simulated by HyNuM with spatially variable K_s and the KWE with the constant value, $K_s = \mu_{Ks}$. Two typical hydrographs from these simulations are shown in Figure 4.3. The hydrographs simulated from the variable K_s surface are matched very well by those computed with the KWE with $K_s = \mu_{Ks}$, although there are some numerical oscillations for the cases of spatially variable K_s surfaces around the steady

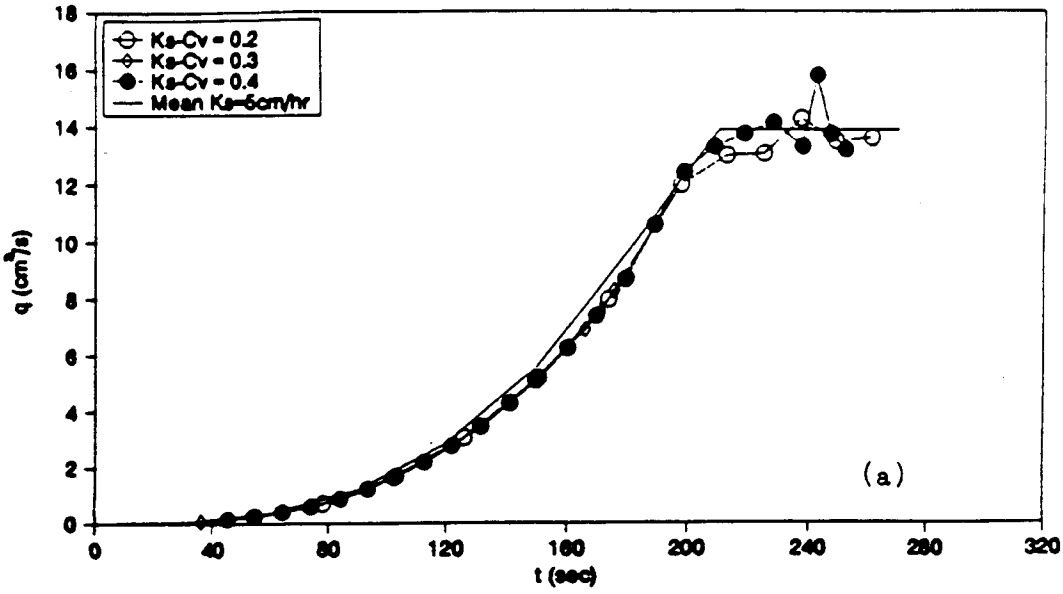

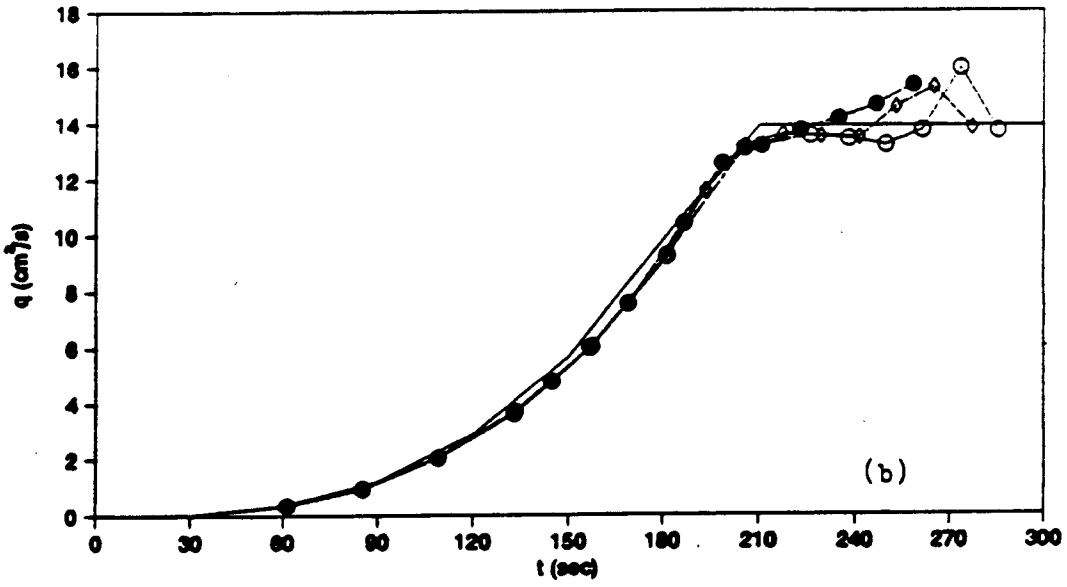

Figure 4.3 Comparison of computed hydrographs from a surface with spatially variable steady infiltration with those computed by using a uniform steady infiltration $K_s = \mu_{Ks}$.
a) $S_x = .05$; $V_o = 10$cm/hr; $K_o = 512$
b) $S_x = .05$; $V_o = 10$cm/hr; $K_o = 1000$

flow rate. For given slope and rainfall intensity, the characteristics of the hydrograph are determined by the distribution mean, μ_{Ks}. The spatial variation of K_s, represented by the standard deviation σ_{Ks}, does not affect the hydrographs. This indicates that for plane surfaces with randomly variable K_s, a simple KWE can be used to predict hydrographs using $K_s = \mu_{Ks}$ wherever the entire surface generates Hortonian runoff.

For each simulation, overland flow fields of depth and velocity are generated. The steady flow fields are used to analyze the effects of spatially variable K_s on the characteristics of overland flow along the flow paths. The typical flow fields for two of three random variation patterns of K_s with different σ_{Ks} are shown in Figure 4.4. The effects of the spatially variable K_s on the flow fields are rather obvious, especially, on the distribution of flow depth. Its influence in altering the flow direction is small, since the pressure gradient due to depth variation in the cross-slope direction is much smaller than that due to the downslope gradient.

Typical cross-slope profiles of mean depth, velocity and flow direction, and the corresponding cross-slope variations are shown in Figure 4.5. The velocity at each grid point is defined by its magnitude at the point

$$V = (u^2 + v^2)^{1/2} \qquad (69)$$

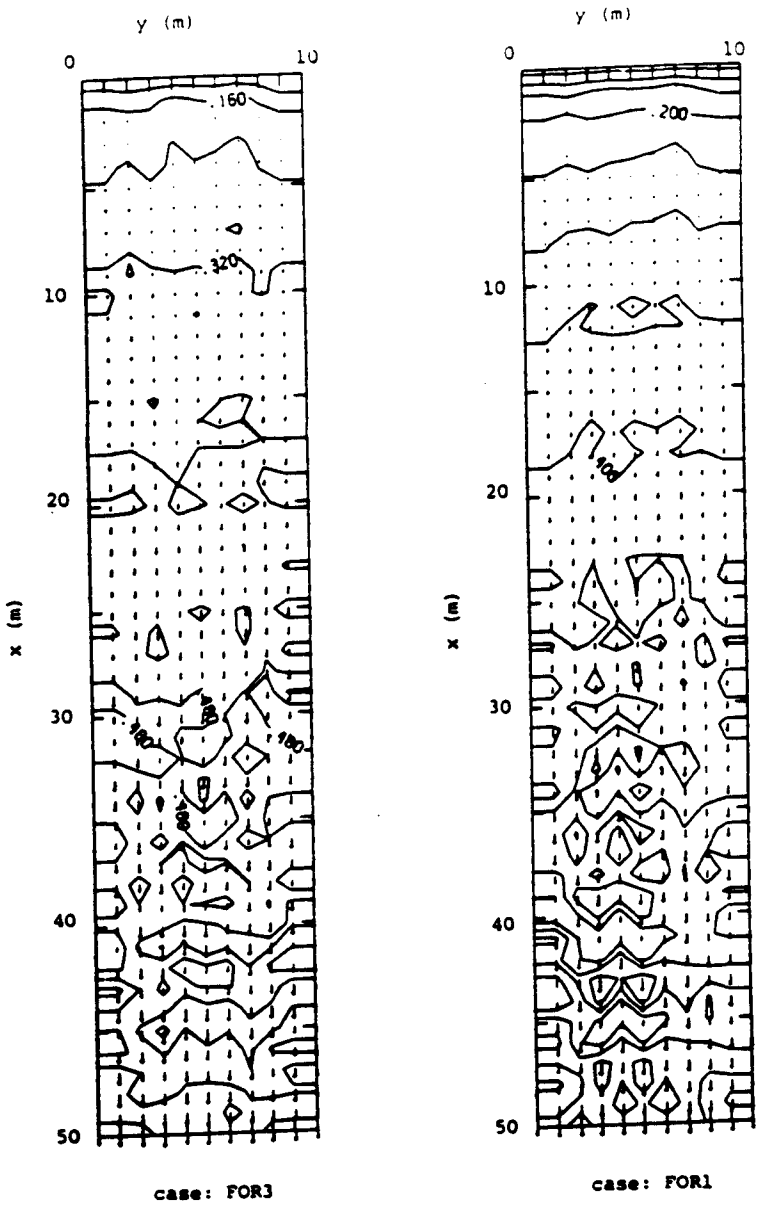

Figure 4.4 Computed steady state flow depth and velocity fields with spatially variable steady infiltration. The contour lines represent depth in cm and vectors represent velocity in cm/s.

FOR3: $S_y = .05$; $K_o = 512$; $V_o = 10$cm/hr; $CV_{Ks} = .4$

FOR1: $S_y = .05$; $K_o = 512$; $V_o = 10$cm/hr; $CV_{Ks} = .1$

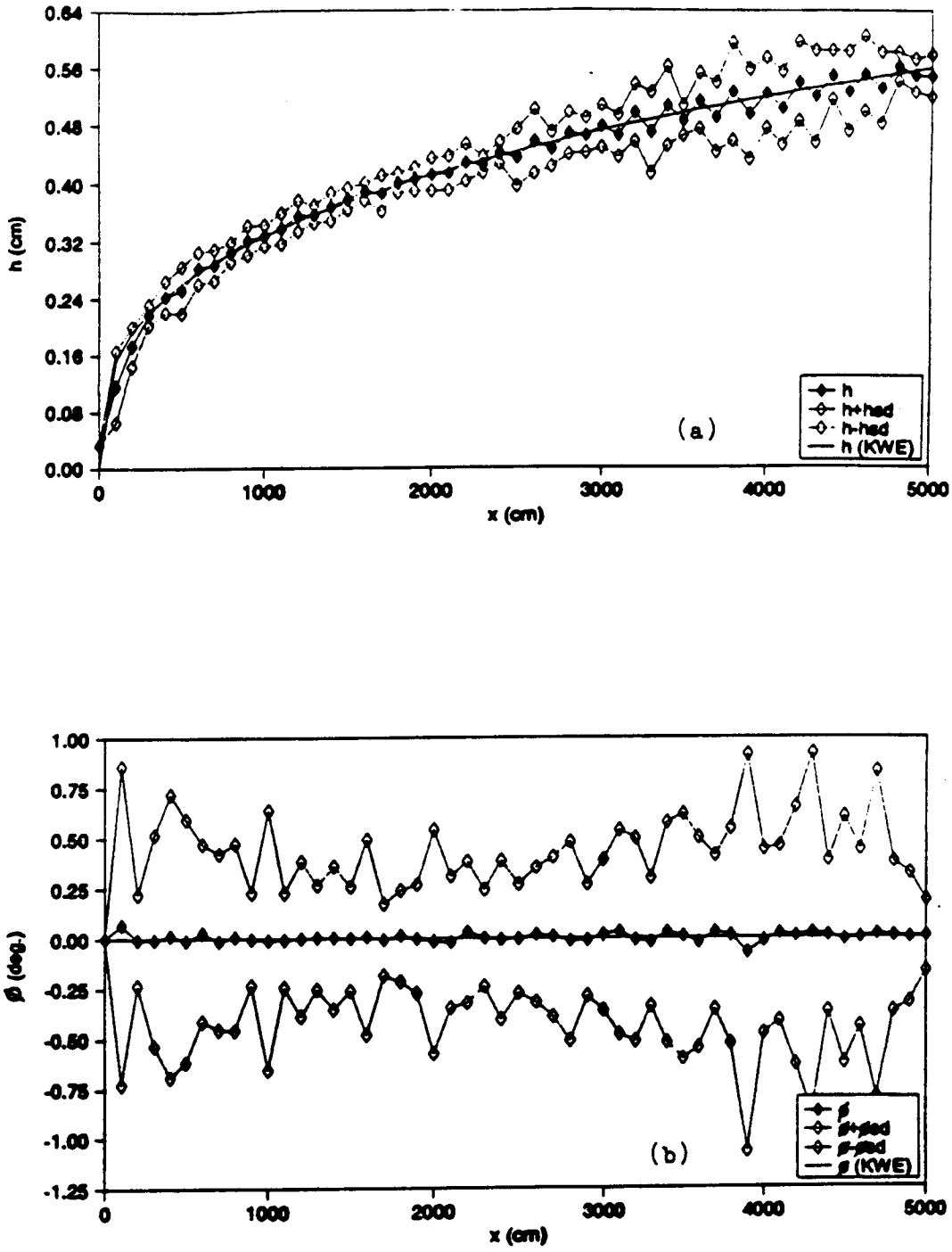

Figure 4.5 Comparison of the computed cross-slope mean profiles of depth, velocity and flow direction with spatially variable steady infiltration to those computed by assuming a uniform steady infiltration $K_s = \mu_{Ks}$ for $S_x = .10$, $K_o = 1000$, $V_o = 10$cm/hr, and $CV_{Ks} = .4$.
where hsd = σ_h; ϕsd = σ_ϕ; Vsd = σ_V
a) depth; b) flow direction

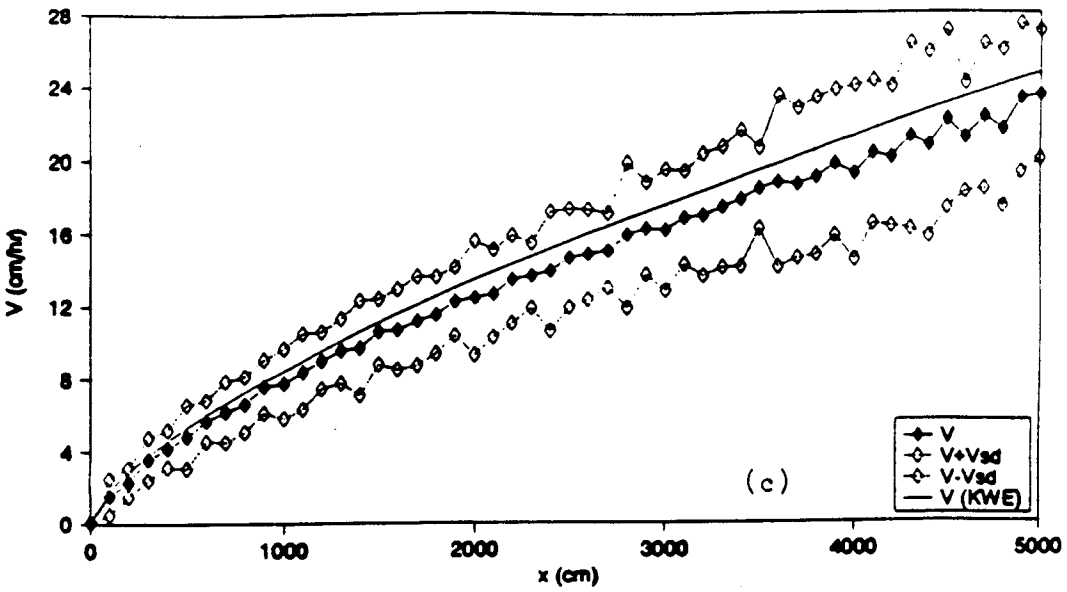

Figure 4.5 continued.
c) velocity

and the flow direction, ϕ, at each grid point is defined by

$$\phi = \tan^{-1}(u/v) \tag{70}$$

The results again show the cross-slope variations in flow fields due to spatially variable K_s.

To compare the impact of spatially variable K_s on the overland flow field under different rainfall, slope, and roughness conditions, the mean cross-slope deviations, σ_*, and mean cross-slope coefficient of variation, CV_*, are defined to reflect the overall spatial variabilities of the flow fields, and they are expressed as

$$\sigma_*^2 = \frac{1}{N} \sum_i \sum_j (\Omega_{ij} - \bar{\Omega}_i)^2 \tag{71}$$

$$CV_* = \frac{\sigma_*}{\bar{\Omega}} \tag{72}$$

where N is the total number of grid points, Ω_{ij} is the value of the variable of interest at node (i,j), $\bar{\Omega}_i$ is the cross-slope mean of the variable of interest in ith row, and $\bar{\Omega}$ is the mean of the variable for the whole flow field. Here, Ω may be h, V or ϕ.

The results for depth, velocity and flow directions are shown in Table 4.1. The variability of the flow, represented by the values of σ_{*h}, CV_{*h}, σ_{*V}, CV_{*V} and $\sigma_{*\phi}$,

Table 4.1 Computed mean cross-slope deviations in depth (σ_{*h}, CV_{*h}), velocity (σ_{*V}, CV_{*V}) and flow direction ($\sigma_{*\phi}$) for random variation in K_s

CASE	σ_{Ks} (cm/hr)	σ_{*h} (cm)	CV_{*h}	σ_{*V} (cm/s)	CV_{*V}	$\sigma_{*\phi}$ (deg)
r = 15 cm/hr; S_x = 5%; K_o = 512; μ_{Ks} = 5 cm/hr						
FOR1	1.0	.0379	.0745	3.23	.173	.60
FOR2	1.5	.0389	.0768	3.41	.185	.64
FOR3	2.0	.0523	.103	3.81	.203	.78
r = 15 cm/hr; S_x = 5%; K_o = 1000; μ_{Ks} = 5 cm/hr						
FOR4	1.0	.0167	.0262	1.57	.106	.44
FOR5	1.5	.0258	.0403	1.66	.112	.49
FOR6	2.0	.0332	.0514	1.79	.120	.55
r = 15 cm/hr; S_x = 10%; K_o = 512; μ_{Ks} = 5 cm/hr						
FOR21	1.0	.0549	.137	7.25	.314	.46
FOR22	1.5	.0730	.183	8.51	.365	.67
FOR23	2.0	.0797	.199	8.98	.379	.77
r = 15 cm/hr; S_x = 10%; K_o = 1000; μ_{Ks} = 5 cm/hr						
FOR28	1.0	.0261	.0517	3.16	.170	.33
FOR29	1.5	.0283	.0558	3.40	.183	.36
FOR30	2.0	.0425	.0842	3.82	.204	.45
r = 11 cm/hr; S_x = 5%; K_o = 1000; μ_{Ks} = 5 cm/hr						
FOR31	1.0	.0223	.0409	1.28	.121	.46
FOR32	1.5	.0332	.0606	1.43	.133	.55
FOR33	2.0	.0440	.0802	1.61	.149	.66

increases as the spatial variability of K_s, i.e., σ_{Ks}, increases. However, depending on mean excess rainfall rate ($V_o = r-\mu_{Ks}$), slope gradient of the plane and surface roughness, the influences of the spatially varying Ks on the cross-slope variations of the flow characteristics can be different.

The impact of spatially varying K_s on the spatial variability of the depth and velocity decreases as slope gradient decreases. With the decrease in slope gradients, flow depth increases and velocity decreases. It is these increased depth and decreased velocity that result in the decrease in spatial variability of flow fields. The variation of flow directions, however, increases as the local slope decreases. This is because that as slope increases, the influence of slope becomes dominant and the flow is forced along the slope direction. While at small slope, the influences of depth and velocity differentials due to spatially variable K_s increases and the flow direction may deviate more from the slope direction. Evidence of the impact of slope can be seen by comparing cases FOR1-3 with FOR21-23 or cases FOR4-6 with FOR28-30.

As surface roughness increases, the depth increases and velocity decreases. As a result, the spatial variability of the flow field becomes smaller for rougher surfaces than that on smoother surface for the same spatially variable K_s surface. This is illustrated by

comparing cases FOR1-3 with FOR4-6 or cases FOR21-23 with FOR28-30.

The influence of the excess rate of rainfall rate is somewhat complicated since both flow depth and velocity become greater as the excess rate of rainfall increases. Comparison of cases FOR4-6 with FOR31-33 shows that while the values of σ_{*V}, CV_{*V}, CV_{*h} and $\sigma_{*\phi}$ decrease as the excess rate of rainfall increases, the value σ_{*h} increases with the excess rate of rainfall.

The simulation results suggest that conditions that favor increasing flow depth and decreasing flow velocity reduce the spatial variability of the flow fields due to spatially varying K_s. The reasons for this are not immediately clear from the two-dimensional hydrodynamic equation (equations 29 - 31). To understand the physics behind these, one needs to understand the behavior of the dependent variables, e.g., depth and velocity, as the functions of the independent variables, such as, slope and surface roughness, and the relationships among the dependent variables themselves though detailed examinations of equations (29) - (31). This is beyond the scope of this research.

From Figure 4.5, it is clear that the KWE with $K_s = \mu_{Ks}$ approximates the mean depth and velocity profiles from the variable K_s surfaces quiet well, but it slightly overestimates the velocity profiles at steady state. The

reason is that the mean velocity for the variable surface is obtained by directly averaging the variable cross-slope velocity, while the mean velocity for the assumed plane is computed using the mean cross-slope depth. Because of the non-linear relationship between depth and velocity, for a given discharge the velocity computed from the mean depth will be greater than that by directly averaging the variable cross-slope velocity. For both depth and velocity profiles, the KWE fails to predict the substantial cross-slope variations.

2) Effects of trending variation

The cases of trending variation listed in Table B.2 were simulated using HyNuM. First, the model simulation are for equilibrium hydrographs, and the results are shown in Figure 4.6. The shapes of the hydrographs are different for the surfaces with downslope increasing K_s and downslope decreasing K_s. In comparison with those generated by the KWE with constant values of $K_s = \mu_{Ks}$, the hydrographs from surfaces of downslope increasing K_s initially rise slower and then faster. This becomes more pronounced, as the gradient of variation, G, increases. For downslope decreasing K_s, the sequence of slow down and speed up of the rise of hydrograph is reversed.

Besides hydrograph shapes, the results show that the time to steady flow for the two different trending

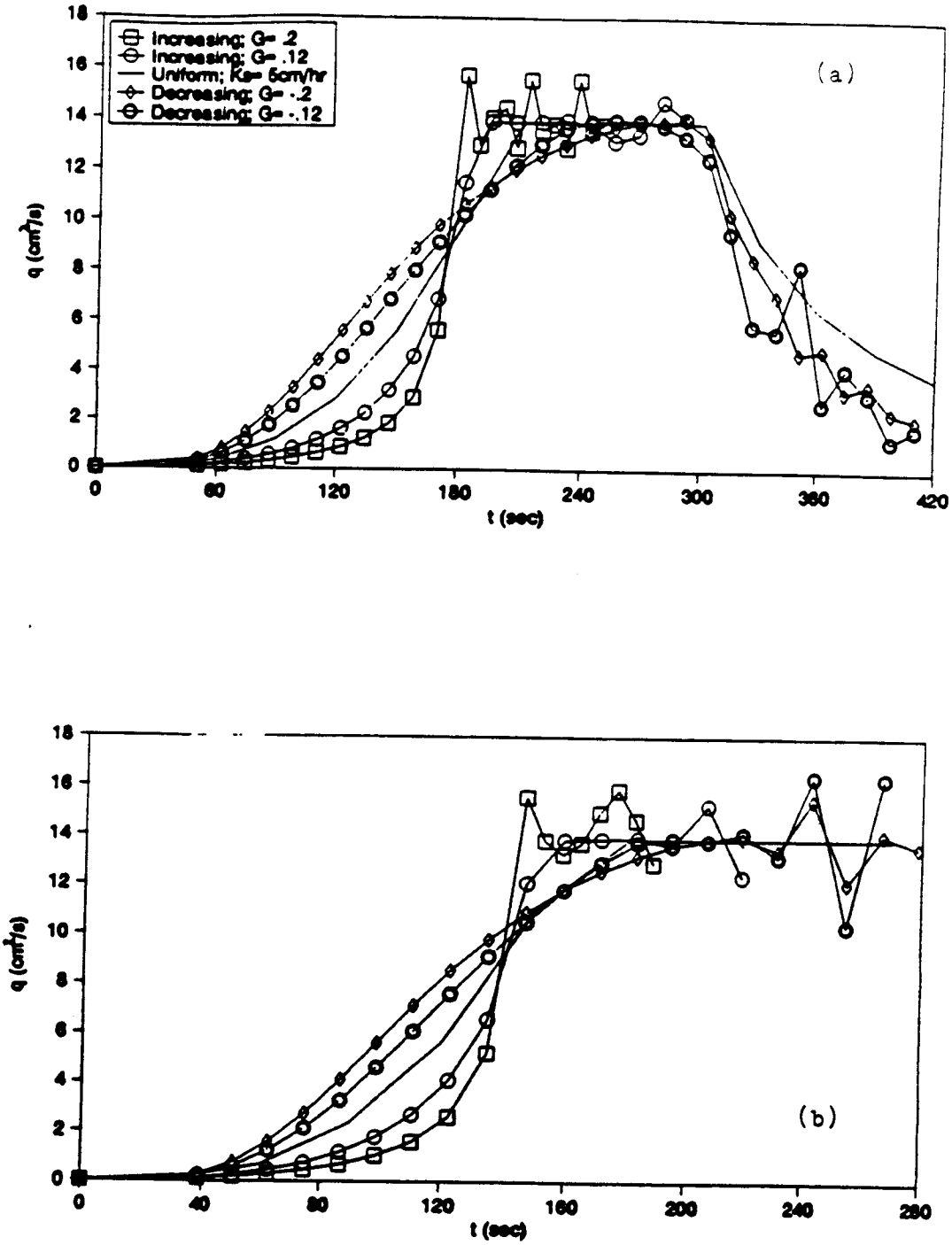

Figure 4.6 Comparison of computed steady state hydrographs from a surface with trending variation in steady infiltration to those computed by assuming a uniform steady infiltration $K_s = \mu_{Ks}$.
a) V_o = 10cm/hr; K_o = 512; S_x = .05
b) V_o = 10cm/hr; K_o = 512; S_x = .10

variations are also different. The ratios of the time to steady flow for the variable K_s surfaces (t_p^1) to those corresponding to uniform surfaces with $K_s = \mu_{Ks}$ (t_p^0) are shown in Table 4.2. For cases of downslope increasing K_s, the ratio of t_p^1/t_p^0 are all less than unity, while the ratio of t_p^1/t_p^0 for downslope decreasing K_s are all greater than unity. The results indicate that runoff reaches steady state faster on surfaces with downslope increasing K_s, and slower on surfaces with downslope decreasing K_s. The larger the absolute values of G, the faster runoff reaches steady state for downslope increasing K_s, and the slower runoff reaches steady state for downslope decreasing K_s. For the cases simulated, the time to steady state is shortened by as much as 14% for case FI1 of downslope increasing K_s and delayed by as much as 28% for case FD13 of downslope decreasing K_s.

In comparison with uniform K_s surfaces, surfaces with downslope increasing K_s generate more water on the upper part of the slope and less water on the lower part of the slope. Therefore, surfaces with downslope increasing K_s contribute less water to the hydrographs than uniform K_s surfaces during the early stage of runoff. Thus, hydrographs for downslope increasing K_s surfaces rise slower initially. When water generated from the upper part of the slope arrives at the bottom of the slope, more water is contributing to the hydrographs from the surfaces

Table 4.2 Time to peak for steady state hydrographs from surfaces with trending variation in K_s (t_p^1) relative to that from uniform surfaces (t_p^o)

CASE	G (cm/hr/m)	t_p^1/t_p^o	CASE	G (cm/hr/m)	t_p^1/t_p^o
r = 15 cm/hr; S_x = 5%; K_o = 512; μ_{Ks} = 5 cm/hr					
FD1	-0.20	1.13	FI1	0.20	.86
FD2	-0.12	1.07	FI2	0.12	.92
FD3	-0.04	1.01	FI3	0.04	.99
r = 15 cm/hr; S_x = 5%; K_o = 1000; μ_{Ks} = 5 cm/hr					
FD4	-0.20	1.19	FI4	0.20	.88
FD5	-0.12	1.09	FI5	0.12	.92
FD6	-0.04	1.02	FI6	0.04	.98
r = 15 cm/hr; S_x = 10%; K_o = 512; μ_{Ks} = 5 cm/hr					
FD7	-0.20	1.13	FI7	0.20	.89
FD8	-0.12	1.09	FI8	0.12	.95
FD9	-0.04	1.02	FI9	0.04	.98
r = 15 cm/hr; S_x = 10%; K_o = 1000; μ_{Ks} = 5 cm/hr					
FD10	-0.20	1.18	FI10	0.20	.88
FD11	-0.12	1.08	FI11	0.12	.92
FD12	-0.04	1.02	FI12	0.04	.96
r = 11 cm/hr; S_x = 5%; K_o = 1000; μ_{Ks} = 5 cm/hr					
FD13	-0.20	1.28	FI13	0.20	.89
FD14	-0.12	1.23	FI14	0.12	.91
FD15	-0.04	1.09	FI15	0.04	.99

with downslope increasing K_s than from the uniform K_s surfaces. The hydrographs rise faster for surfaces with downslope increasing K_s than for uniform K_s surfaces. Because more water is generated from the upper part of the slope on the surface with downslope increasing K_s, a deeper and faster flow wave is created from the upper part of the slope and catches up with the downslope slower flow. Therefore, the concentration time or time to equilibrium discharge is shortened for the surface with downslope increasing K_s.

For surfaces with downslope decreasing K_s the opposite occurs. For this case, more water is generated on the lower part of slope and less water on the upper part of the slope relative to uniform K_s surfaces. Therefore, hydrographs initially rise faster, then slower on the surfaces with downslope decreasing K_s than on the uniform K_s surfaces. Since less water is generated on the upper part of the slope on the surfaces with downslope decreasing K_s than that on the corresponding uniform K_s surfaces, the flow is shallower and the velocity is smaller on the upper part of the slope of the surface with downslope decreasing K_s than on the uniform K_s surface. As a result, the concentration time or time to equilibrium discharge is longer for the surface with downslope decreasing K_s than that from uniform K_s surface.

The impact of the trending variations on the characteristics of non-equilibrium hydrographs is more significant. To show the impact, an arbitrary rainfall duration of $t_r = 0.75\ t_s^0$ is chosen for the simulation. The results are shown in Figure 4.7. The impact of downslope decreasing K_s is relatively simple. The peak discharges for these cases occur at about the time of cessation of rainfall, t_r, the same as those from spatially uniform surfaces with $K_s = \mu_{Ks}$. This is also indicated by the ratio of t_p^1/t_p^0 in Table 4.3, where t_p^1 and t_p^0 are the times to peak discharges from surfaces with downslope decreasing K_s and uniform surfaces of $K_s = \mu_{Ks}$, respectively. However, downslope decreasing K_s has caused higher peak discharges. This is indicated by the hydrographs in Figure 4.7 and the values of q_p^1/q_p^0 in Table 4.3, where q_p^1 is the peak discharges from downslope decreasing K_s and q_p^0 is the peak discharge on the spatially uniform surfaces with $K_s = \mu_{Ks}$. The results show that the peak discharge increases as the absolute value of G increases. Comparison of cases FD10-12 with cases FD13-15 indicates that for given values of slope and surface roughness, the percentage of increase in peak discharge from the corresponding uniform surface of $K_s = \mu_{Ks}$ becomes larger as the excess rainfall rate decreases. The maximum increase in peak discharge is as much as 72% for case FD13. These higher peak discharges for surfaces with

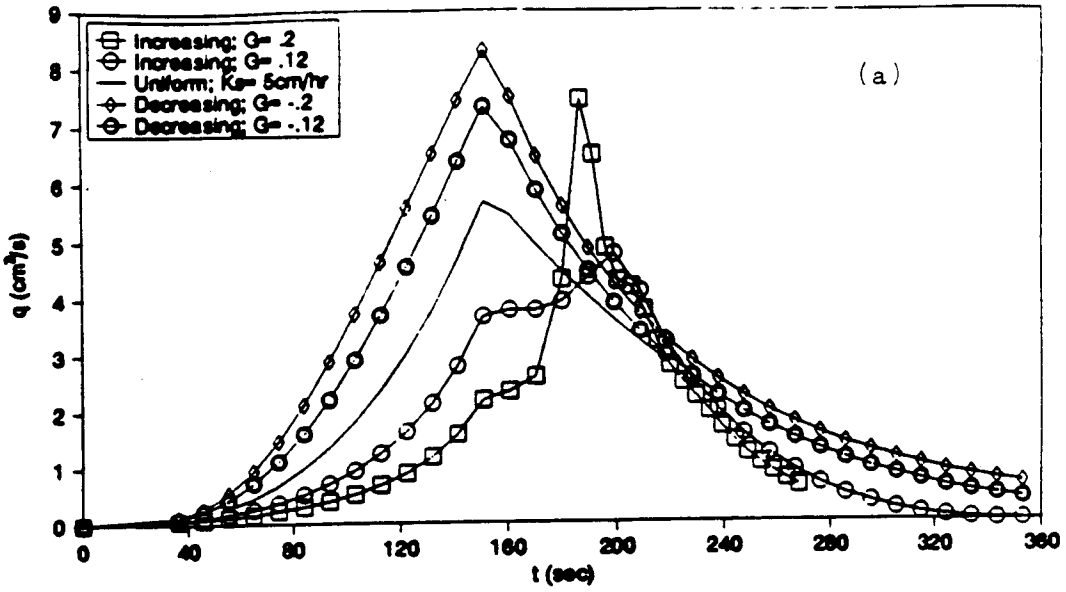

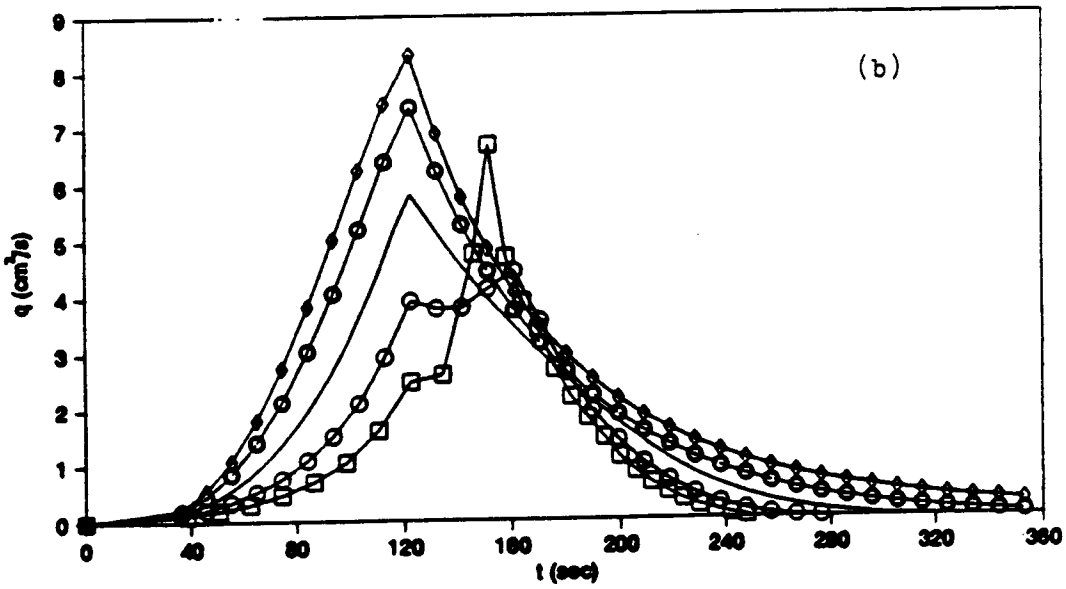

Figure 4.7 Comparison of computed hydrographs from a surface with trending variation in steady infiltration to those computed by assuming a uniform steady infiltration $K_s = \mu_{Ks}$.
a) V_o = 10cm/hr; K_o = 512; S_x = .05
b) V_o = 10cm/hr; K_o = 512; S_x = .10

Table 4.3 Peak and time to peak for hydrographs from surfaces with trending variation in K_s (q_p^1, t_p^1) relative to those from uniform surfaces (q_p^o, t_p^o)

CASE	G (cm/hr/m)	$\frac{t_p^1}{t_p^o}$	$\frac{q_p^1}{q_p^o}$	CASE	G (cm/hr/m)	$\frac{t_p^1}{t_p^o}$	$\frac{q_p^1}{q_p^o}$
r = 15 cm/hr; S_x = 5%; K_o = 512; μ_{Ks} = 5 cm/hr							
FD1	-0.20	.99	1.46	FI1	0.20	1.22	1.31
FD2	-0.12	.99	1.29	FI2	0.12	1.30	.84
FD3	-0.04	.99	1.10	FI3	0.04	.99	.89
r = 15 cm/hr; S_x = 5%; K_o = 1000; μ_{Ks} = 5 cm/hr							
FD4	-0.20	1.01	1.42	FI4	0.20	1.26	1.03
FD5	-0.12	1.01	1.26	FI5	0.12	1.30	.79
FD6	-0.04	1.01	1.09	FI6	0.04	1.02	.90
r = 15 cm/hr; S_x = 10%; K_o = 512; μ_{Ks} = 5 cm/hr							
FD7	-0.20	1.01	1.43	FI7	0.20	1.25	1.15
FD8	-0.12	1.01	1.27	FI8	0.12	1.33	.76
FD9	-0.04	1.01	1.09	FI9	0.04	1.01	.90
r = 15 cm/hr; S_x = 10%; K_o = 1000; μ_{Ks} = 5 cm/hr							
FD10	-0.20	1.00	1.44	FI10	0.20	1.26	1.04
FD11	-0.12	1.00	1.28	FI11	0.12	1.32	.72
FD12	-0.04	1.00	1.10	FI12	0.04	1.00	.89
r = 11 cm/hr; S_x = 5%; K_o = 1000; μ_{Ks} = 5 cm/hr							
FD13	-0.20	.99	1.72	FI13	0.20	1.17	2.03
FD14	-0.12	.99	1.46	FI14	0.12	1.24	.94
FD15	-0.04	.99	1.17	FI15	0.04	1.02	.81

downslope decreasing K_s are caused by the early contribution of runoff from the lower part of the slope where infiltration rates are smaller and more water is generated.

The influence of downslope increasing K_s on the hydrograph is complex. The peak discharges for these cases do not always occur at the time of rainfall cessation. The ratios of t_p^1/t_p^0 in Table 4.3 suggest that the times to peak discharge are generally delayed. For some cases, the delay in comparison with the corresponding uniform K_s surfaces is significant, e.g., as much as 33% for case FI8. The shapes of the hydrographs and the peak discharges are also different from those computed for the corresponding uniform surface. For the cases of $G < 0.12$ (cm/hr)/m, the peak discharges are smaller than those generated from the corresponding uniform surfaces. As G increases to 0.2 (cm/hr)/m, the time to peak discharge is still delayed, and the magnitudes of the peaks have significantly increased. For case FI15, the hydrograph from the downslope increasing K_s surface is even greater than that from downslope decreasing K_s surface, and the peak discharge is almost doubled that of the corresponding uniform K_s surface. The initial lower discharge results from the early contribution of runoff from the lower part of the slope where less water is generated because of larger infiltration rates. The noticeable increase of

discharge after the cessation of rainfall is caused by the arrival of flow waves from the upper part of the slope where infiltration rates are smaller and more water is generated.

Significant prediction errors result from assuming a homogeneous plane with $K_s = \mu_{Ks}$ when the slope has a trending variation in K_s. However, in the absence of cross-slope variations in K_s, the hydrographs from the trending variation in K_s may be approximated using a kinematic cascade model with the trending variation in K_s being assigned to each cascade element.

3) Effects of trending variation with embedded randomness

The effects of trending variation with embedded randomness in K_s are simulated for four different cases listed in Table B.3. Two of the resulting hydrographs are shown in Figure 4.8. These results are almost identical to those computed with only trending variation. This indicates that the characteristics of hydrographs are mainly influenced by the trending variation, and the embedded random variation has little impact on the hydrograph characteristics. Bias in hydrograph characteristics can result if the KWE model is used with spatially constant K_s.

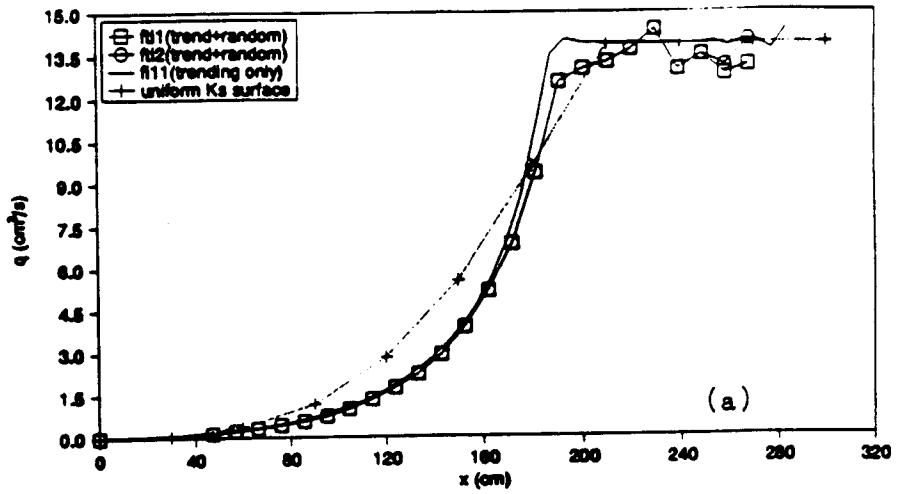

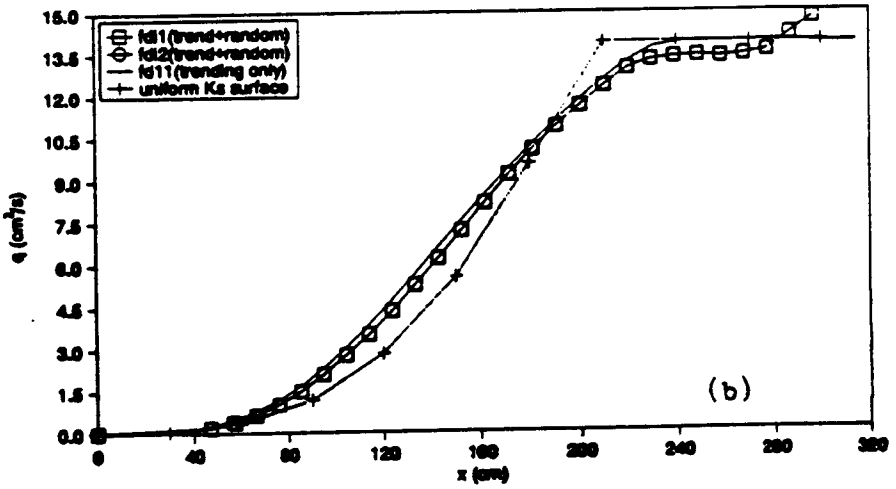

Figure 4.8 Comparison of computed steady state hydrographs from a surface with trending steady infiltration and embedded randomness to those computed by assuming a uniform steady infiltration $K_s = \mu_{Ks}$ for $S_x = .10$, $K_o = 1000$, and $V_o = 10$cm/hr.
a) downslope increasing and embedded randomness
b) downslope decreasing and embedded randomness

Embedded random variation strongly influences the flow fields. This is shown by the flow fields in Figure 4.9 and the cross-slope variation of depth, velocity and flow direction in Figures 4.10 and 4.11. The profiles simulated using the KWE model by assuming a constant value of $K_s = \mu_{Ks}$ approximated those from spatially variable K_s rather well. However, the cross-slope variability in flow can not be predicted by the KWE model. For the cases with small random variation in K_s, the cross-slope variability of the flow is relatively small. As the randomness in K_s, or σ_{Ks}, increases, the variability in the flow field can be significant as indicated by the results in the above section.

4.4.2 Effects of Spatial Variation in Surface Roughness

1) Effects of random variation

Simulations were performed on surfaces with spatially variable roughness, K_o, using HyNuM, and for a uniform plane with constant $K_o = \mu_{Ko}$ using the KWE. Figure 4.12 shows two simulated hydrographs. As for the results from the case of randomly variable K_s, the spatial variation of K_o, represented by σ_{Ko}, does not affect the hydrographs. For given values of slope, saturated hydraulic conductivity, and rainfall intensity, the resulting hydrographs are only influenced by the distribution mean, μ_{Ko}. For the randomly distributed K_o, the flow hydrographs

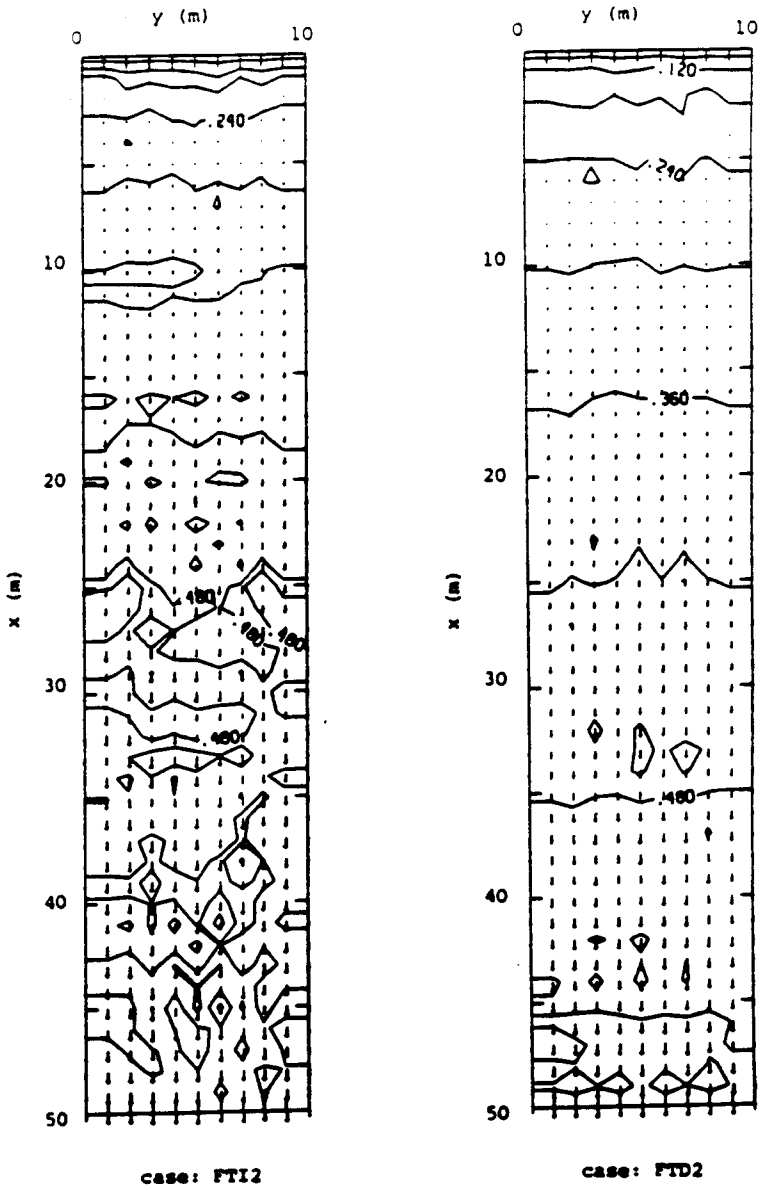

Figure 4.9 Computed steady state flow depth and velocity fields from a surface with downslope trending variation in steady infiltration and embedded randomness. The contour lines represent depth in cm and vectors represent velocity in cm/s.
FTI2: S_x = .10; V_o = 10cm/hr; G = .12(cm/hr)/m;
K_o = 1000; μ_{Ks} = 0cm/hr; σ_{Ks} = 1 cm/hr;
FTD2: S_x = .10; V_o = 10cm/hr; G = -.12(cm/hr)/m;
K_o = 1000; μ_{Ks} = 0cm/hr; σ_{Ks} = 1 cm/hr

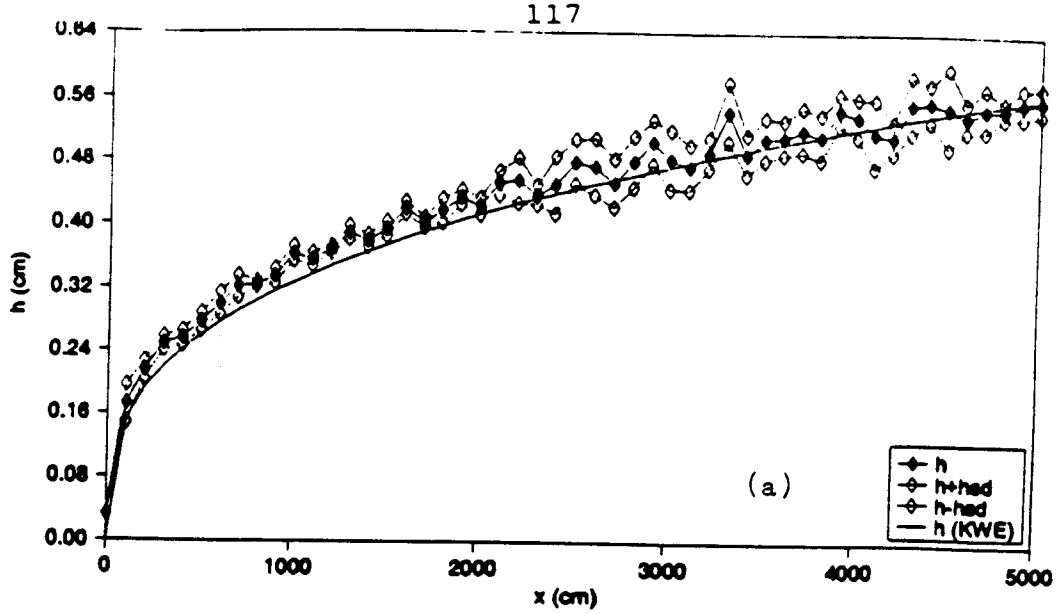

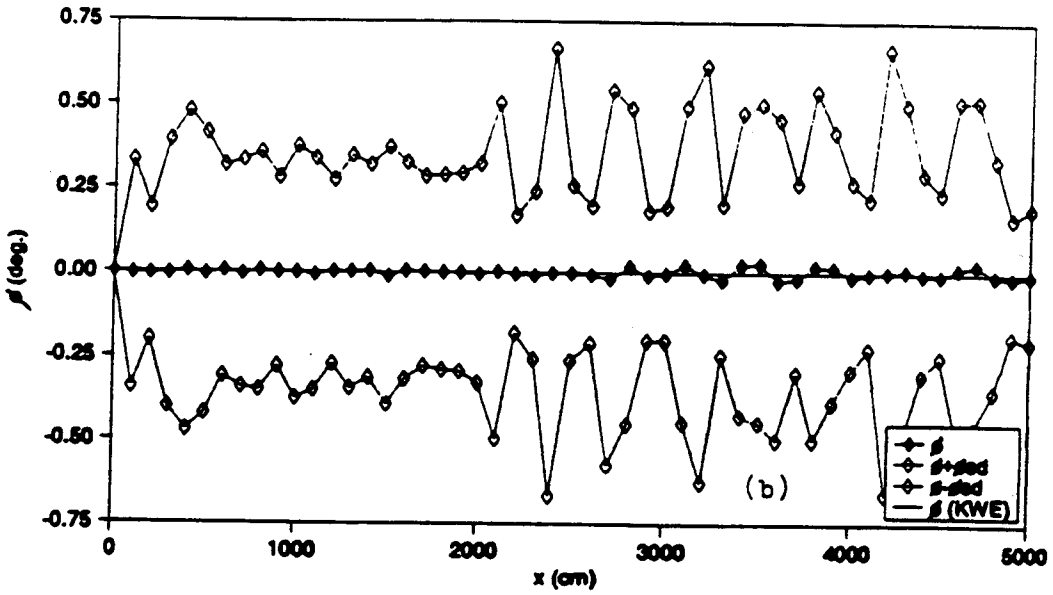

Figure 4.10 Comparison of the computed cross slope mean profiles of depth, velocity and flow direction on surfaces with downslope increasing steady infiltration and embedded randomness to those computed by assuming a uniform steady infiltration $K_s = \mu_{Ks}$ for $S_x = .10$, $K_o = 1000$, $V_o = 10$cm/hr, and $CV_{Ks} = .2$.
where hsd = σ_h; Vsd = σ_V; ϕsd = σ_ϕ
a) depth; b) flow direction

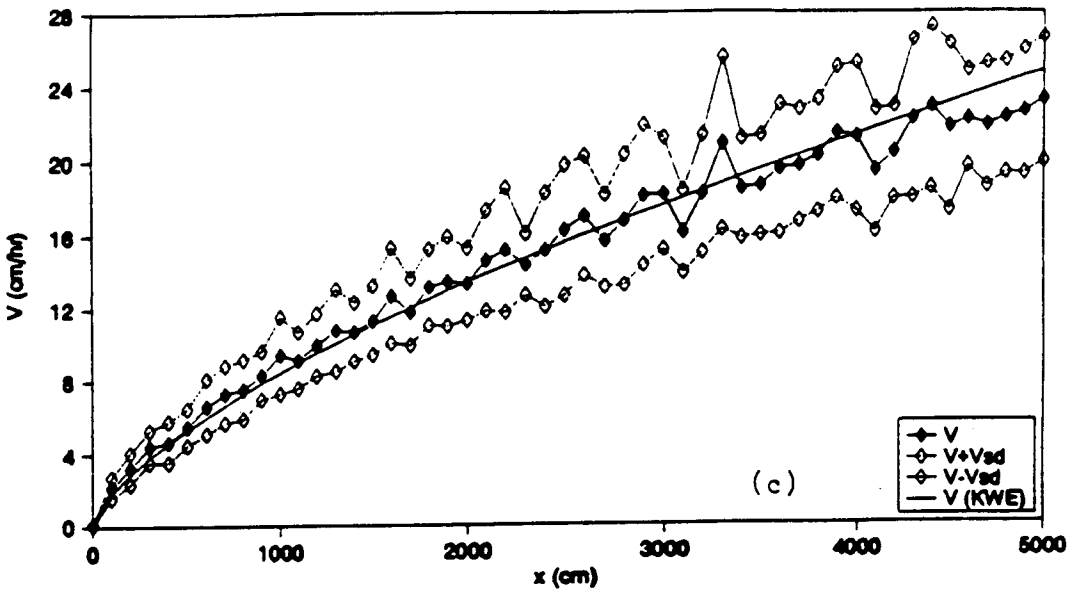

Figure 4.10 continued.
c) velocity

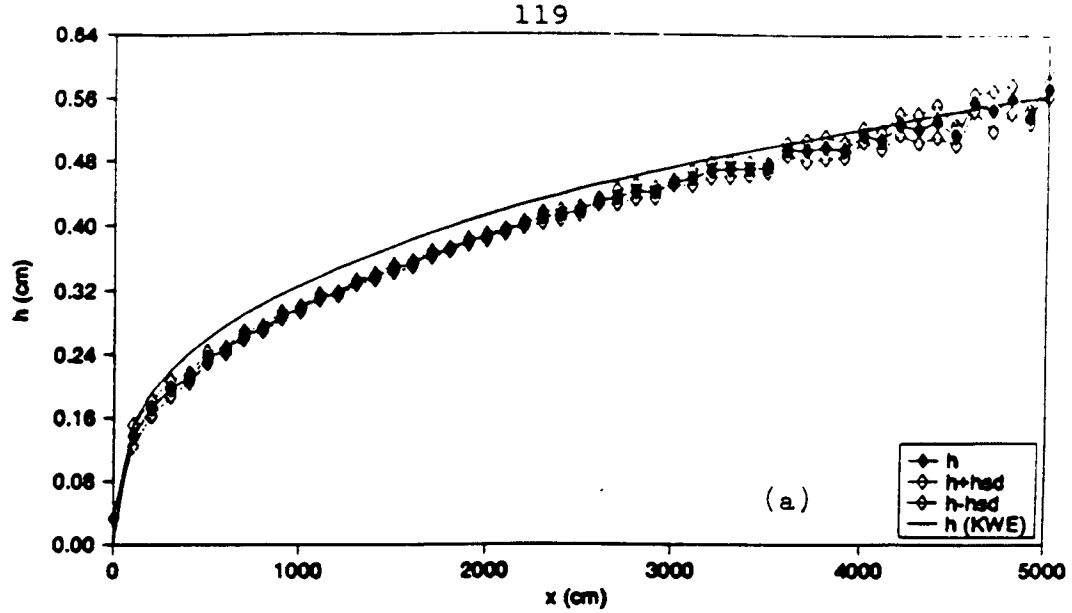

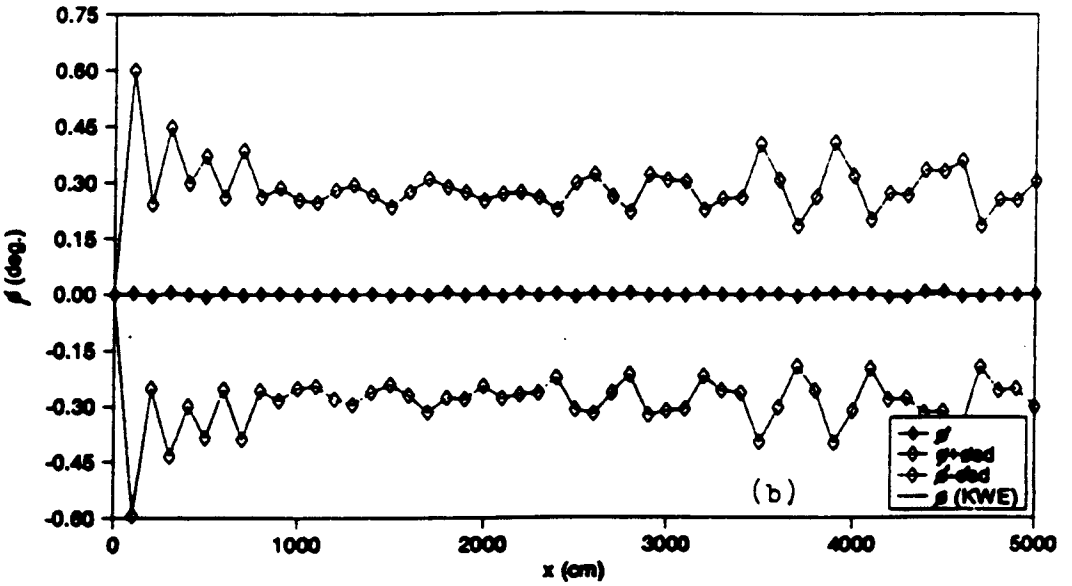

Figure 4.11 Comparison of the computed cross-slope mean profiles of depth, velocity and flow direction on surfaces with downslope decreasing steady infiltration and embedded randomness to those computed by assuming a uniform steady infiltration $K_s = \mu_{Ks}$ for $S_x = .10$, $K_o = 1000$, $V_o = 10$cm/hr, and $CV_{Ks} = .2$.
where hsd = σ_h; Vsd = σ_V; ϕsd = σ_ϕ
a) depth; b) flow direction

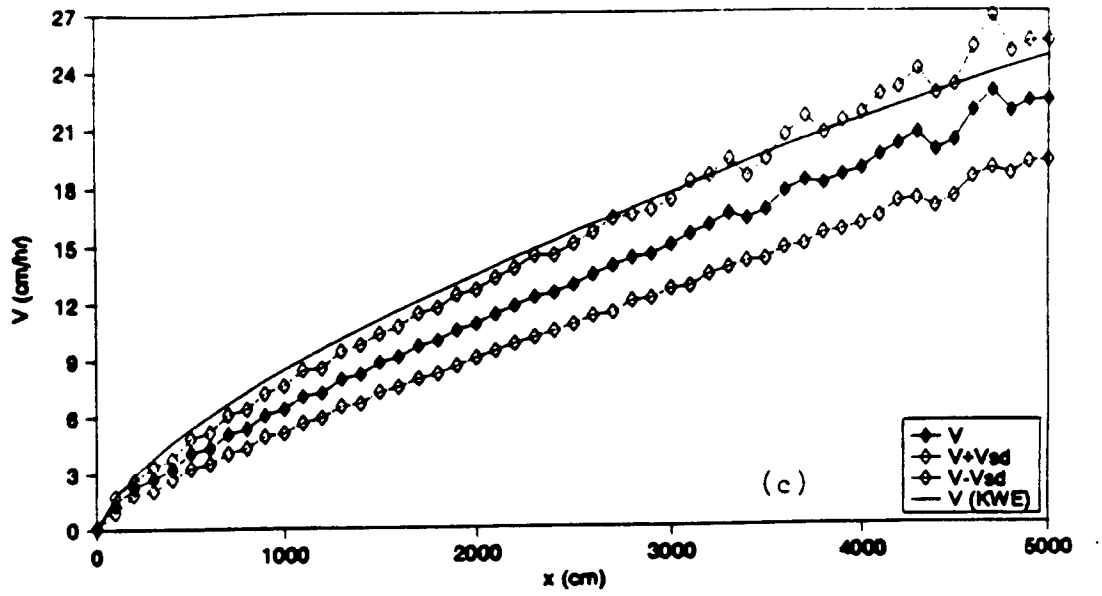

Figure 4.11 continued.
c) velocity

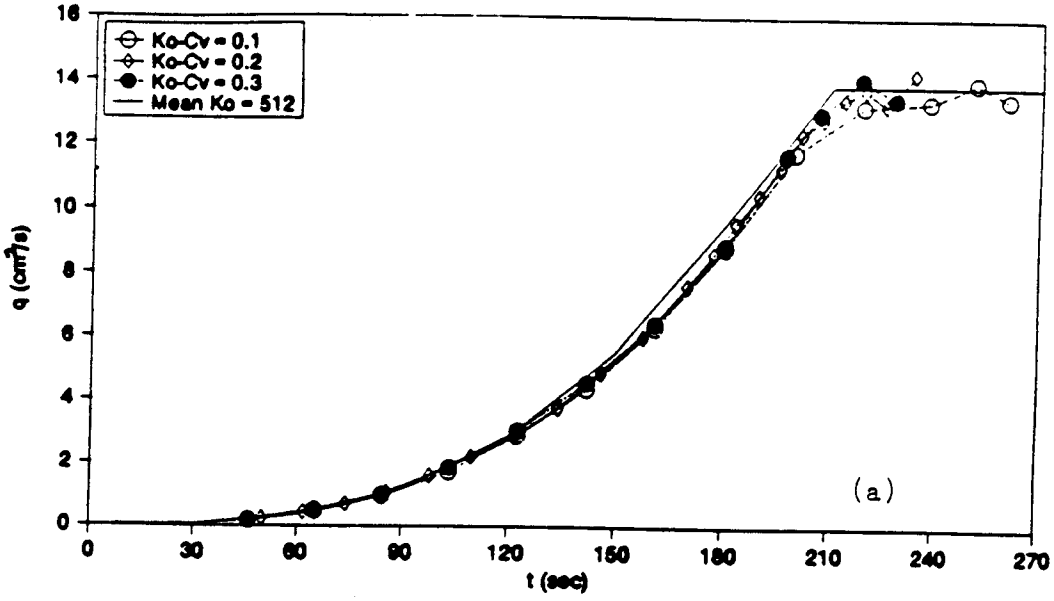

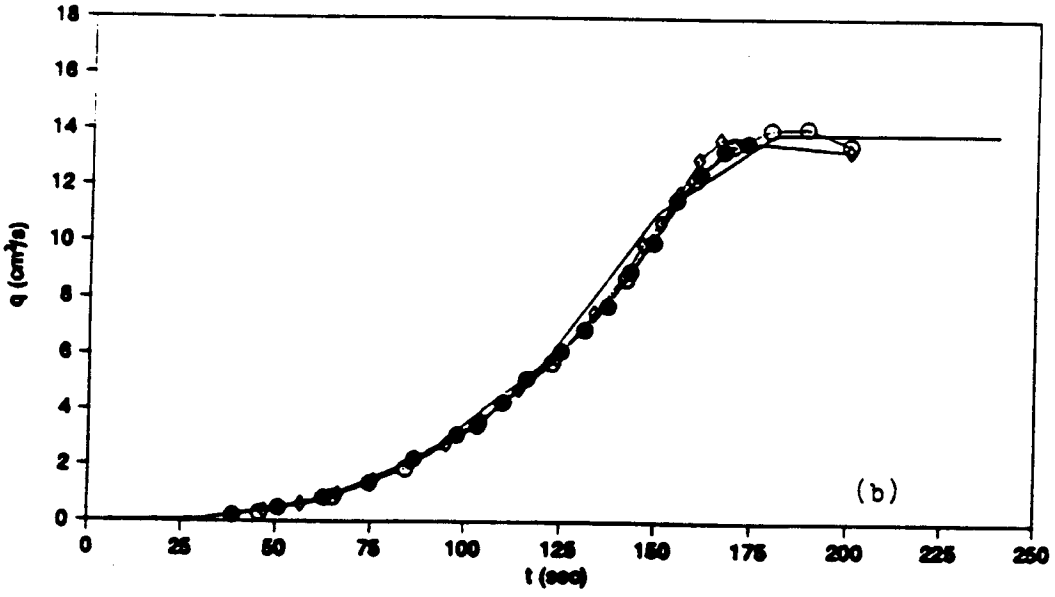

Figure 4.12 Comparison of computed hydrographs from a surface with spatially variable roughness to those computed by assuming a uniform roughness parameter $K_o = \mu_{Ko}$.
a) V_o = 10cm/hr; S_x = .05
b) V_o = 10cm/hr; S_x = .10

can be accurately predicted by the KWE with constant K_o = μ_{Ko}.

Two typical flow fields for the spatial distributions of K_o for different σ_{Ko} are plotted in Figure 4.13. The flow fields strongly reflect the spatial variation of K_o. The mean cross-slope flow depth, velocity and flow direction along with those computed by the KWE with K_o = μ_{Ko} are shown in Figure 4.14. The flow depth, velocity, and flow direction have considerable variations around their mean values. The variability of flow fields expressed in terms of σ_* and CV_* are presented in Table 4.4. For a given slope and excess rainfall rate, the spatial variability of the flow fields, represented by σ_{*h}, CV_{*h}, σ_{*V}, CV_{*V}, and $\sigma_{*\phi}$, increases with increasing σ_{Ko}.

The influences of spatially variable K_o on flow fields are different under different rainfall and hillslope conditions. For a given variation of surface roughness, σ_{Ko}, as the mean surface roughness, μ_{Ko}, increases, there is a reduction in the values of CV_{*h}, σ_{*V}, CV_{*V}, and $\sigma_{*\phi}$, except for the value of σ_{*h}. For smaller excess rainfall rate, e.g., V_o = 5cm/hr, σ_{*h} increases as μ_{Ko} increases, while for a larger excess rainfall rate, e.g., V_o = 10cm/hr, σ_{*h} decreases with increasing μ_{Ko}. The influence of surface slope is similar to the case with spatially varying K_s, i.e., as surface

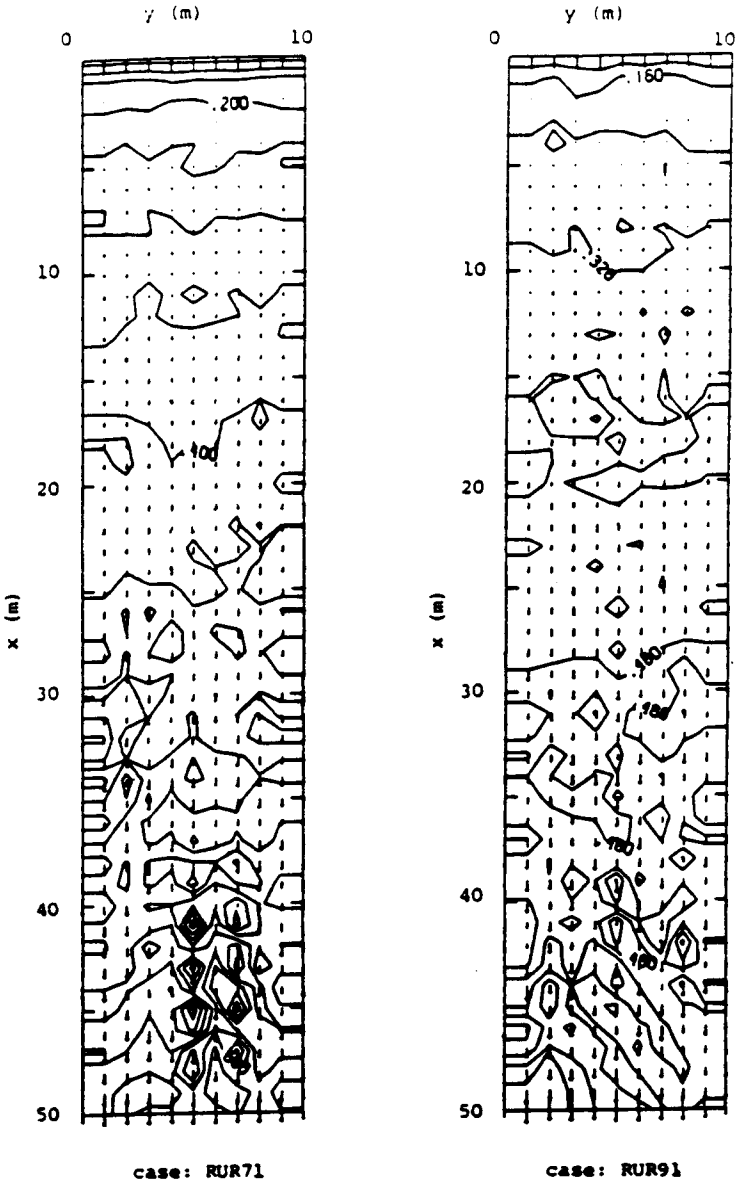

Figure 4.13 Computed steady state flow depth and velocity fields with spatially variable roughness. The contour lines represent depth in cm and vectors represent velocity in cm/s.
RUR71: S_x = .05; V_o = 10cm/hr; CV_{Ko} = .1
RUR91: S_x = .05; V_o = 10cm/hr; CV_{Ko} = .2

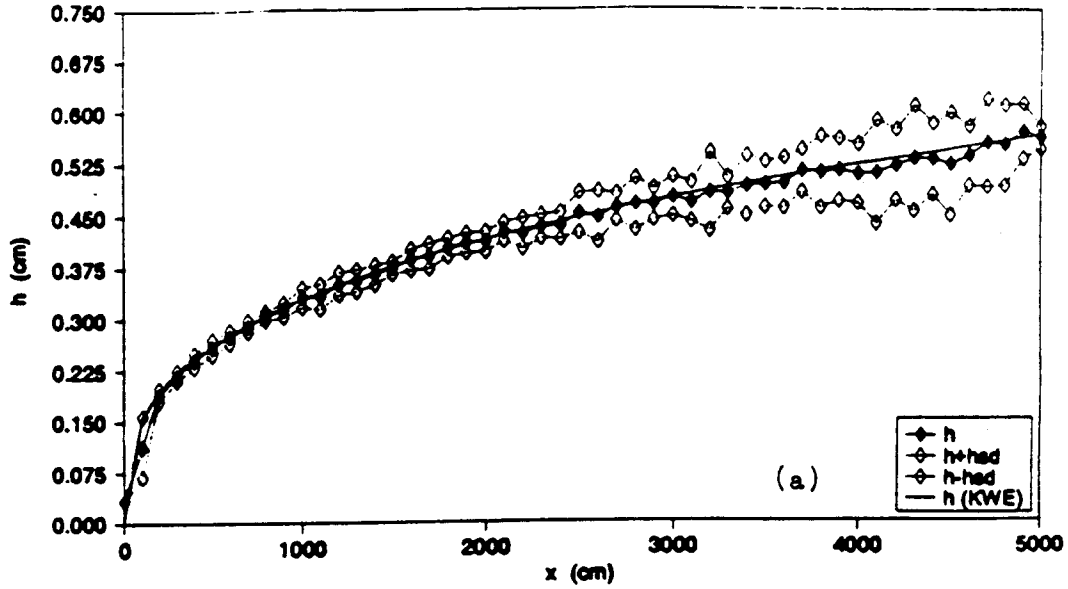

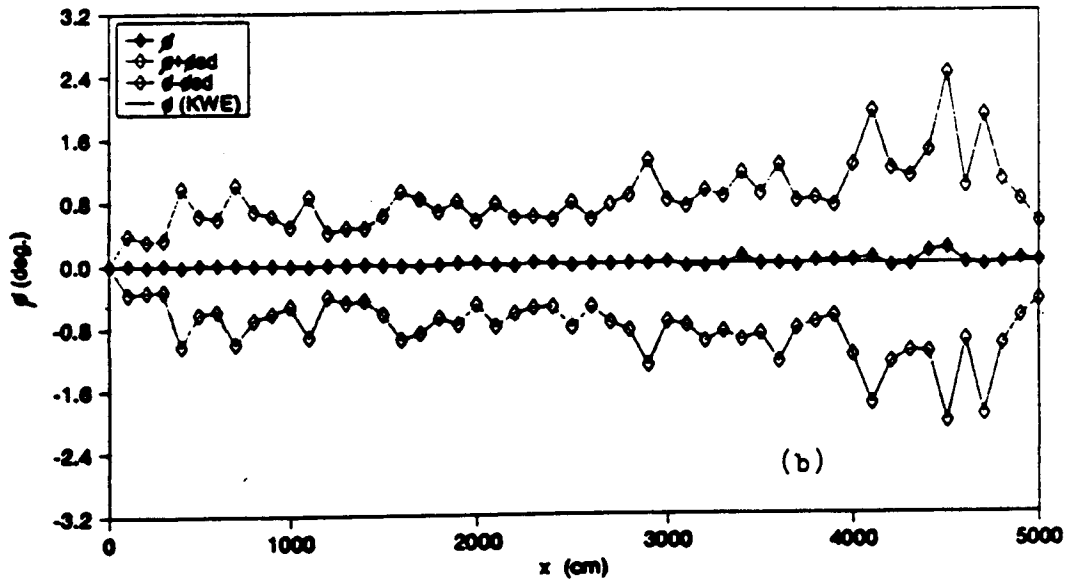

Figure 4.14 Comparison of the computed cross-slope mean profiles of depth, velocity and flow direction with spatially variable roughness to those computed by assuming a uniform roughness $K_o = \mu_{Ko}$ for $S_x = .05$, $V_o = 10$cm/hr, and $CV_{Ko} = .2$. where hsd = σ_h; Vsd = σ_V; ϕsd = σ_ϕ
a) depth; b) flow direction

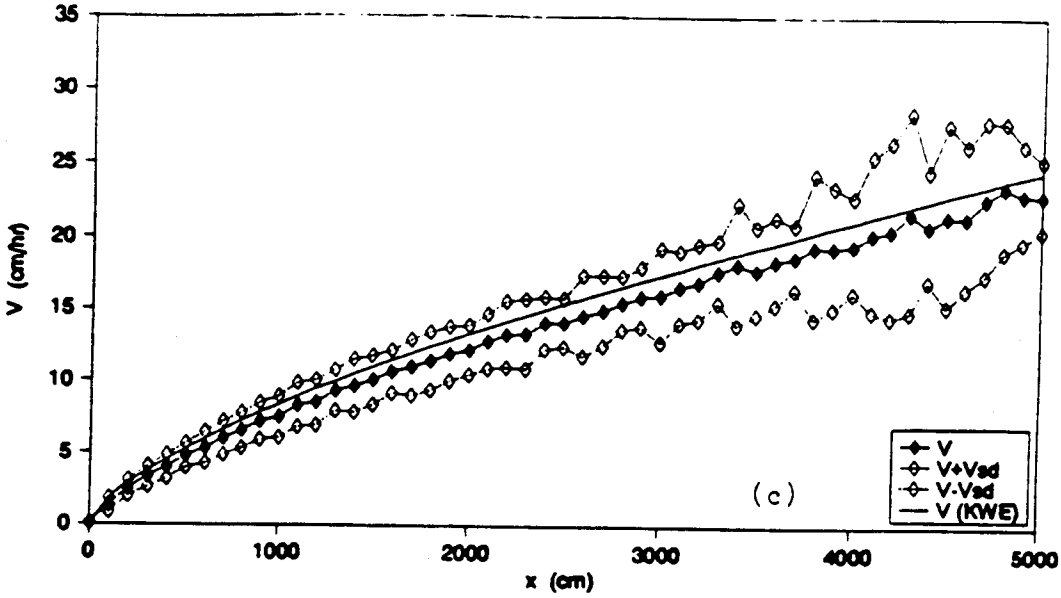

Figure 4.14 continued.
c) velocity

Table 4.4 Computed mean cross-slope deviations in depth (σ_{*h}, CV_{*h}), velocity (σ_{*V}, CV_{*V}) and flow direction ($\sigma_{*\phi}$) for random variation in K_o

CASE	σ_{Ko}	σ_{*h} (cm)	CV_{*h}	σ_{*V}	CV_{*V} (cm/s)	$\sigma_{*\phi}$ (deg)
r = 15 cm/hr; S_x = 5%; K_s = 5 cm/hr; μ_{Ko} = 512						
RUR71	51.2	.0434	.0852	3.73	.195	.864
RUR91	102.4	.0539	.107	4.06	.212	1.18
RUR81	153.6	.0789	.158	6.05	.315	2.69
r = 15 cm/hr; S_x = 5%; K_s = 5 cm/hr; μ_{Ko} = 1000						
RUR72	100	.0093	.0390	1.64	.111	.738
RUR92	200	.0439	.0699	1.81	.131	1.37
RUR82	300	.0818	.130	3.41	.218	2.08
r = 15 cm/hr; S_x = 5%; K_s = 10 cm/hr; μ_{Ko} = 512						
RUR212	51.2	.0154	.039	1.46	.126	.539
RUR232	102.4	.0281	.0703	1.75	.148	.983
RUR222	153.6	.0441	.110	2.20	.184	1.34
r = 15 cm/hr; S_x = 5%; K_s = 10 cm/hr; μ_{Ko} = 1000						
RUR112	100	.0190	.0380	1.10	.118	.653
RUR132	200	.0350	.0700	1.31	.138	1.28
RUR122	300	.0540	.110	1.77	.184	1.69
r = 15 cm/hr; S_x = 10%; K_s = 5 cm/hr; μ_{Ko} = 512						
RUR11	51.2	.0465	.120	6.33	.272	.403
RUR31	102.4	.0700	.176	9.11	.379	.726
RUR21	153.6	.0838	.210	-	-	-
r = 15 cm/hr; S_x = 10%; K_s = 5 cm/hr; μ_{Ko} = 1000						
RUR12	100	.0231	.0460	3.06	.164	.378
RUR32	200	.0478	.0878	3.92	.207	.647
RUR22	300	.0711	.140	4.93	.254	.765

Table 4.4 continued.

r = 15 cm/hr;	S_x = 10%;	K_s = 10 cm/hr;	μ_{Ko} = 512			
RUR41	51.2	.0137	.0430	2.56	.176	.270
RUR61	102.4	.0266	.0835	3.00	.201	.455
RUR51	153.6	.0346	.110	3.36	.226	.509
r = 15 cm/hr;	S_x = 10%;	K_s = 10 cm/hr;	μ_{Ko} = 1000			
RUR42	100	.0150	.0380	1.85	.158	.316
RUR62	200	.0285	.0718	2.18	.184	.565
RUR52	300	.0487	.110	2.46	.205	.760

slope decreases the spatial variability of the flow due to the spatially varying K_o becomes smaller. The only exception is the spatial variability of flow direction, which increases as slope decreases. The reason for this is due to the increasing impact of slope gradient as the slope gets steeper. As the flow depth increases and velocity decreases due to increasing mean surface roughness and decreasing slope, the variability of flow fields decreases. However, for the same hillslope conditions, as the excess rainfall rate increases, the variability of the flow fields due to spatially variable surface roughness increases, even though the flow depths become greater. This is caused by the increase of flow velocity with increasing excess rainfall rate. I have not been able to explain sufficiently the physics behind these findings for the reason given in section 4.4.1.

As for the cases of randomly variable K_s, the KWE with $K_o = \mu_{Ko}$ can provide good approximations of the mean flow depth and velocity, however, it can not predict the cross-slope variation of the flow fields.

2) Effects of trending variation

Simulated equilibrium hydrographs on surfaces with the trending variation of K_o (Table B.5) are shown in Figure 4.15. The impacts of the trending variation of K_o are similar to those of K_s. In comparison with those

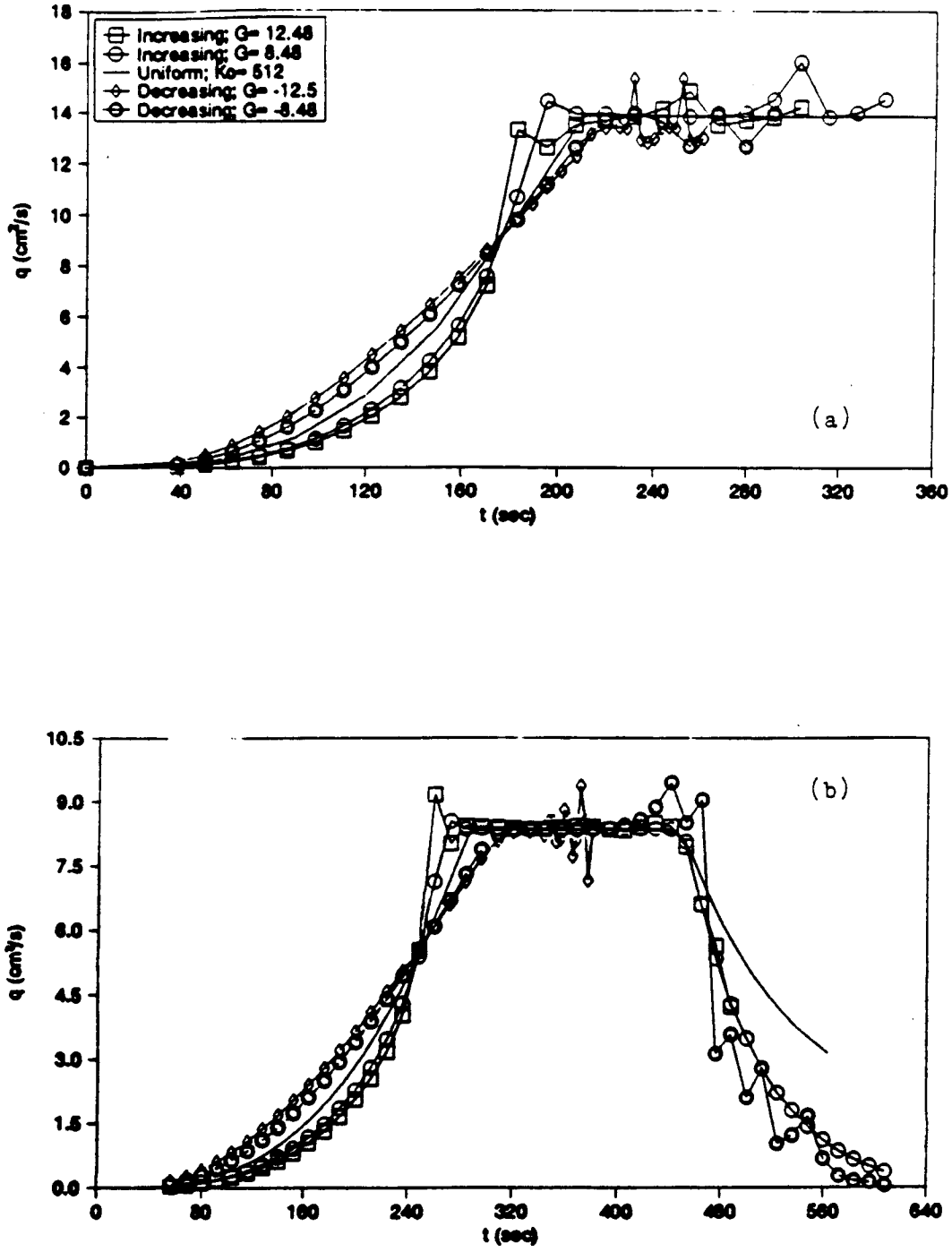

Figure 4.15 Comparison of computed steady state hydrographs from a surface with trending variation in roughness to those computed by assuming a uniform roughness $K_o = \mu_{K_o}$.
a) $S_x = .05$; $K_o = 512$; $V_o = 10$cm/hr
b) $S_x = .05$; $K_o = 512$; $V_o = 6$cm/hr

computed from the uniform surfaces with $K_o = \mu_{Ko}$, the hydrographs from downslope increasing K_o initially rise slower and then faster. This becomes more pronounced, as the gradient of variation, G, increases. For downslope decreasing K_o, the sequence of slow down and speed up of the hydrograph rise is reversed.

The time to steady flow also differs between the different trending variations. The ratios of the equilibrium times for variable K_o and uniform K_o surfaces are shown in Table 4.5. For downslope decreasing K_o, the ratios of t_p^1/t_p^0 are all greater than unity, while the ratios of t_p^1/t_p^0 for downslope increasing K_o are all less than unity. Therefore, the runoff reaches its steady flow faster on the surface with downslope increasing K_o than that from the uniform surface with $K_o = \mu_{Ko}$; on surfaces with downslope decreasing K_o flow equilibrates slower. The larger the absolute value of G, the faster runoff reaches the steady state for downslope increasing K_o and the slower runoff reaches the steady state for downslope decreasing K_o. For downslope increasing K_o, the time to steady state is shortened by as much as 12% (RI10), and for downslope decreasing K_o, the time to steady state is delayed by as much as 28% (RD10).

These effects of trending variation in K_o on the equilibrium hydrographs may be explained as follows. For a surface with downslope increasing K_o, the velocity

Table 4.5 Time to peak for steady state hydrographs from surfaces with trending variation in K_o (t_p^1) relative to that from uniform surfaces (t_p^o)

CASE	G (m^{-1})	t_p^1/t_p^0	CASE	G (m^{-1})	t_p^1/t_p^0
r = 15 cm/hr; S_x = 5%; K_S = 5 cm/hr; μ_{Ko} = 512					
RD1	-12.48	1.07	RI1	12.48	.89
RD2	-8.48	1.04	RI2	8.48	.93
RD3	-4.48	1.01	RI3	4.48	.95
r = 15 cm/hr; S_x = 10%; K_S = 5 cm/hr; μ_{Ko} = 512					
RD4	-12.48	1.05	RI4	12.48	.90
RD5	-8.48	1.04	RI5	8.48	.98
RD6	-4.48	1.04	RI6	4.48	.98
r = 11 cm/hr; S_x = 5%; K_S = 5 cm/hr; μ_{Ko} = 512					
RD7	-12.48	1.08	RI7	12.48	.91
RD8	-8.48	1.08	RI8	8.48	.95
RD9	-4.48	1.03	RI9	4.48	.99
r = 11 cm/hr; S_x = 5%; K_S = 5 cm/hr; μ_{Ko} = 1000					
RD10	-12.48	1.11	RI10	12.48	.88
RD11	-8.48	1.08	RI11	8.48	.94
RD12	-4.48	1.01	RI12	4.48	.95

decreases downslope. Therefore, there is less water flowing off the lower part of the slope from a surface with downslope increasing K_o than from a uniform K_o surface during the early stage of runoff. This results in an initially slower rise in hydrographs for the surface with downslope increasing K_o. However, as time elapses, the faster flow generated from the upper part of the slope with downslope increasing K_o starts catching up with the slower flow on the lower part of the slope, thus creating a flow shock wave with greater depth and velocity. As many of the waves continue arriving at the bottom of the slope, the rise of the hydrograph becomes faster for the surface with downslope increasing K_o. Also, because of the creation of the deeper and faster flow waves, the concentration time is shorted for the surface with downslope increasing K_o.

For surfaces with downslope decreasing K_o the opposite occurs. The flow velocity increases as K_o decreases downslope. Therefore, hydrographs initially rise faster, then slower on surfaces with downslope decreasing K_o than those from uniform K_o surfaces. With the slower flow on the upper part of the slope and faster flow on the lower part of the slope, no shock waves can be generated. As a result, the concentration time becomes longer for the surface with downslope decreasing K_o than that for the corresponding uniform K_o surface.

As for the trending variation of K_s, the impact of trending variation of K_o on non-equilibrium hydrographs are also more significant. The results for a rainfall duration of $t_r = 0.75\ t_s^0$ are shown in Figure 4.16. The peak discharges for cases of downslope decreasing K_o occur at about t_r, the same as those from uniform surfaces with $K_o = \mu_{Ko}$. This is also indicated by the ratio of t_p^1/t_p^0 in Table 4.5. Downslope decreasing K_o has caused significant increase in peak discharge. As the absolute values of G increase, the peak discharges increase from 7% to as much as 17% (Table 4.6) compared with those from uniform roughness surfaces with $K_o = \mu_{Ko}$. These higher peak discharges for surfaces with downslope decreasing K_o are caused by the early contribution of runoff from the lower part of the slope where the surfaces are smoother and water runs off the surfaces faster.

The hydrograph response for downslope increasing K_o is similar to that for downslope increasing K_s but the effect of trending variation of K_o is stronger than that of trending variation of K_s. The peak discharges for these cases do not always occur at the time of rainfall cessation. The the ratio of t_p^1/t_p^0 in Table 4.6 suggests that the time to peak discharge is generally delayed. The percentage of delay in comparison with the corresponding uniform K_o surface is as much as 32% for case RI2. Thus, the delay of peak discharge can be significant. The shapes

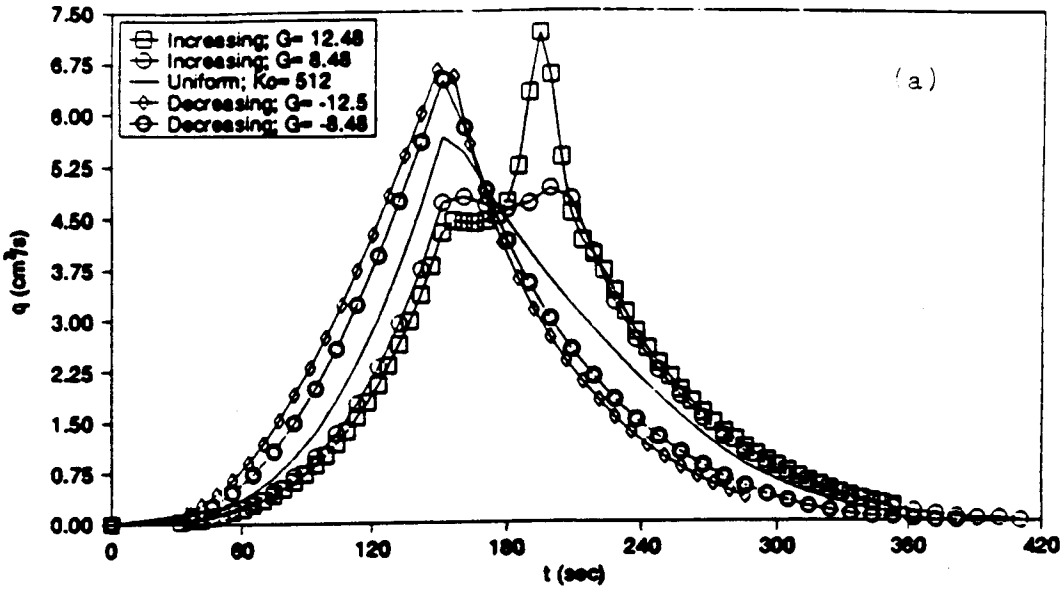

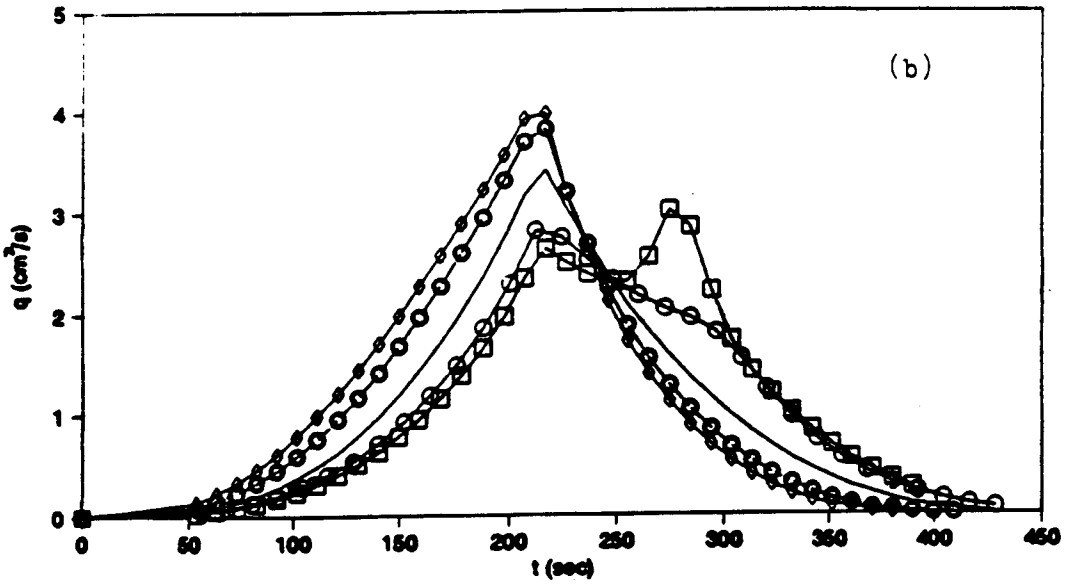

Figure 4.16 Comparison of computed hydrographs from a surface with trending variation in roughness to those computed by assuming a uniform roughness $K_o = \mu_{Ko}$.
a) $S_x = .05$; $K_o = 512$; $V_o = 10cm/hr$
b) $S_x = .05$; $K_o = 512$; $V_o = 6cm/hr$

Table 4.6 Peak and time to peak for hydrographs from surfaces with trending variation in K_o (q_p^1, t_p^1) relative to those from uniform surfaces (q_p^o, t_p^o)

CASE	G (m^{-1})	$\frac{t_p^1}{t_p^o}$	$\frac{q_p^1}{q_p^o}$	CASE	G (m^{-1})	$\frac{t_p^1}{t_p^o}$	$\frac{q_p^1}{q_p^o}$
r = 15 cm/hr; S_x = 5%; K_s = 5 cm/hr; μ_{Ko} = 512							
RD1	-12.48	.99	1.16	RI1	12.48	1.28	1.26
RD2	-8.48	1.00	1.15	RI2	8.48	1.32	.71
RD3	-4.48	1.01	1.11	RI3	4.48	1.00	.91
r = 15 cm/hr; S_x = 10%; K_s = 5 cm/hr; μ_{Ko} = 512							
RD4	-12.48	1.00	1.17	RI4	12.48	1.26	1.21
RD5	-8.48	1.00	1.12	RI5	8.48	1.30	.84
RD6	-4.48	1.00	1.07	RI6	4.48	1.00	.91
r = 11 cm/hr; S_x = 5%; K_s = 5 cm/hr; μ_{Ko} = 512							
RD7	-12.48	1.00	1.17	RI7	12.48	1.26	.96
RD8	-8.48	1.00	1.12	RI8	8.48	.98	.89
RD9	-4.48	1.00	1.07	RI9	4.48	1.00	1.00

of the hydrographs and the peak discharges are also different from those computed from the corresponding uniformly rough surface. As the values of G increases from 4.48/m to 12.48/m, the hydrographs change from single peaks to double peaks, and the higher peaks shift from the time immediately after rainfall cessation to that occurring some time after rainfall cessation. For smaller values of G, the peak discharges are smaller than those generated from the corresponding uniformly rough surfaces. For G = 12.48/m, the magnitudes of the peaks are larger than those from the corresponding uniform surfaces, and some are even greater that those from surfaces with downslope decreasing K_o, e.g., cases RI1 and RI4. The initial lower discharge results from the early contribution of runoff from the lower part of the slope where the surface is rougher and less water runs off the surface. The noticeable increase in discharge after the cessation of rainfall is caused by the arrival of the flow shock waves, which are produced by faster flow from the upper part of the slope catching up with the slower flow on the lower part of the slope.

From the results, one can see that the resultant hydrograph from the trending variation K_o surface can not generally be reproduced using the KWE with the constant values of $K_o = \mu_{Ko}$. Again, in the absence of the cross-slope variation in K_o, the above results simulated by the

two-dimensional model may also be approximated by a KWE based cascade model.

3) Effects of trending variation with embedded randomness

The effects of trending variation with embedded randomness in K_o are simulated for four different cases listed in Table B.6. The resulting hydrographs are shown in Figure 4.17. These results are almost identical to those computed with only trending variation. Clearly, the embedded variations in K_o exert no influence on the characteristics of the hydrograph. The hydrograph from the spatially variable K_o surface is mainly determined by its trending variation component. The embedded random variation, on the other hand, has a strong influence on the flow fields. The flow fields and the mean flow profiles in depth, velocity and flow direction along the spatially variable K_o surfaces are in Figures 4.18, 4.19, and 4.20.

Significant errors can be generated in both hydrographs and flow fields if the KWE is applied on the assumed homogeneous surfaces with Ko = μKo.

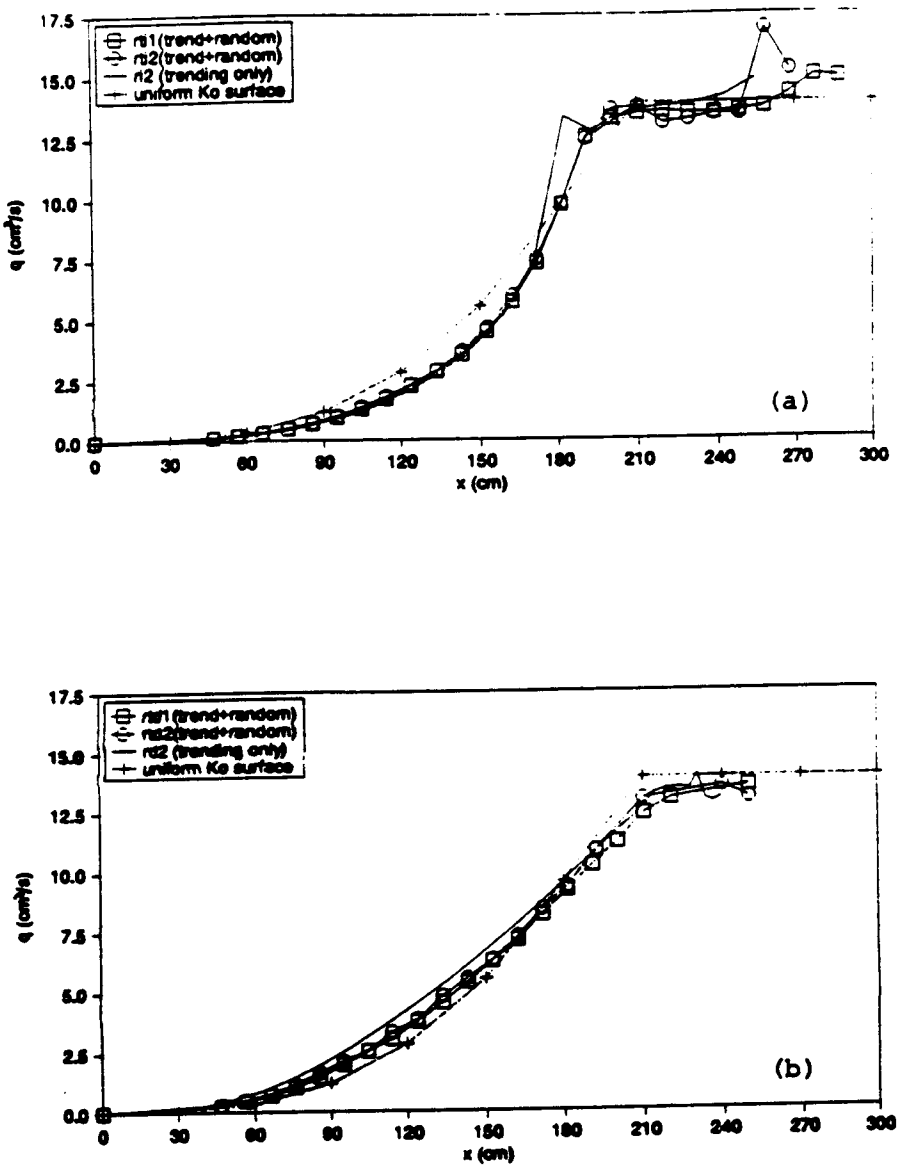

Figure 4.17 Comparison of computed steady state hydrographs from a surface with trending variation in roughness and embedded randomness to those computed by assuming a uniform roughness K_o = μ_{Ko} for S_x = .05, K_o = 512, and V_o = 10cm/hr.
a) downslope increasing and embedded randomness
b) downslope decreasing and embedded randomness

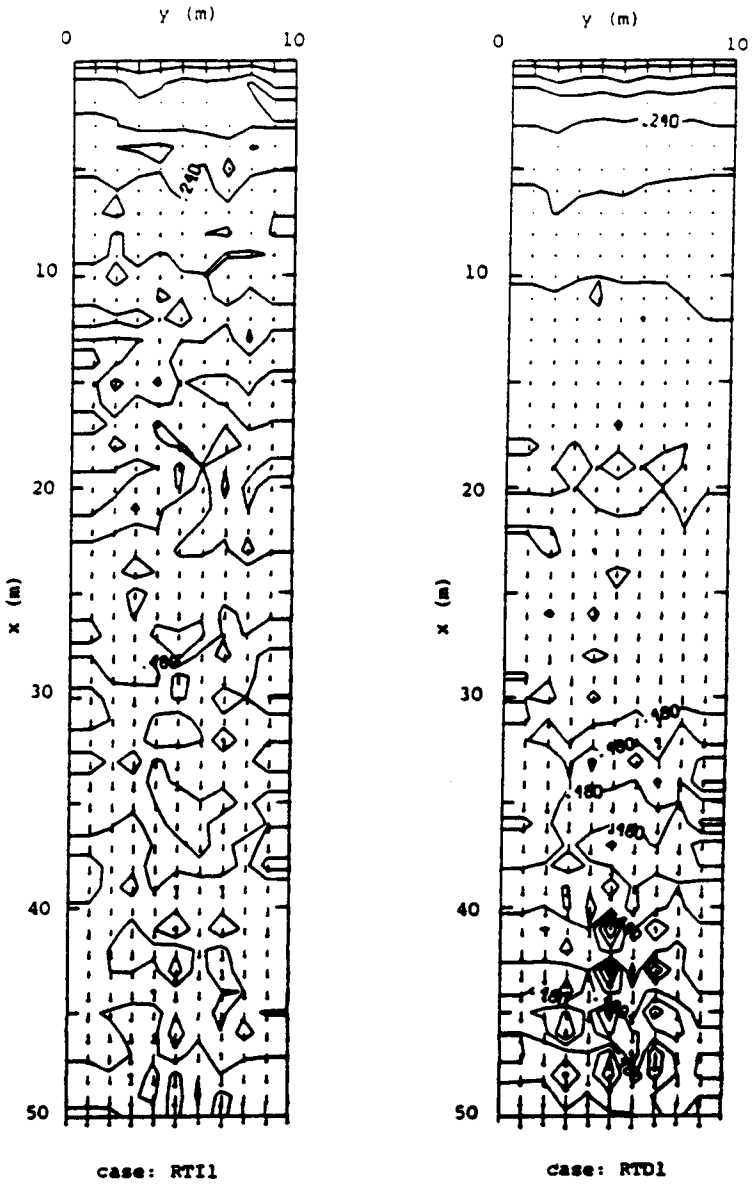

Figure 4.18 Computed steady state flow depth and velocity fields from a surface with downslope trending variation in roughness and embedded randomness. The contour lines represent depth in cm and vectors represent velocity in cm/s.
RTI1: S_x = .05; V_o = 10cm/hr; G = .0848;
μ_{Ko} = 0; σ_{Ko} = 51.2;
RTI1: S_x = .05; V_o = 10cm/hr; G = -.0848;
μ_{Ko} = 0; σ_{Ko} = 51.2

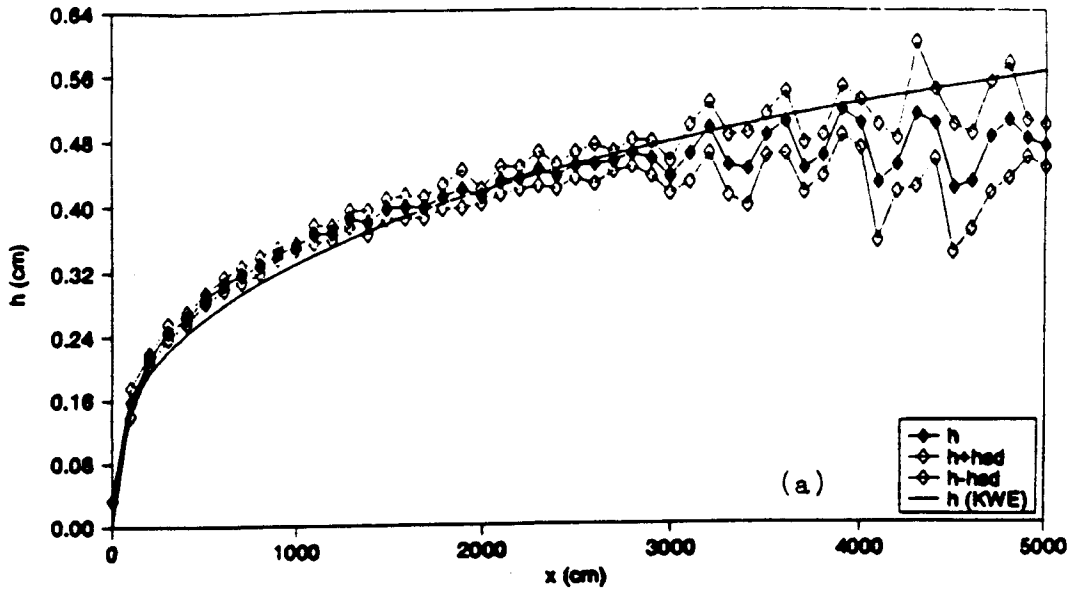

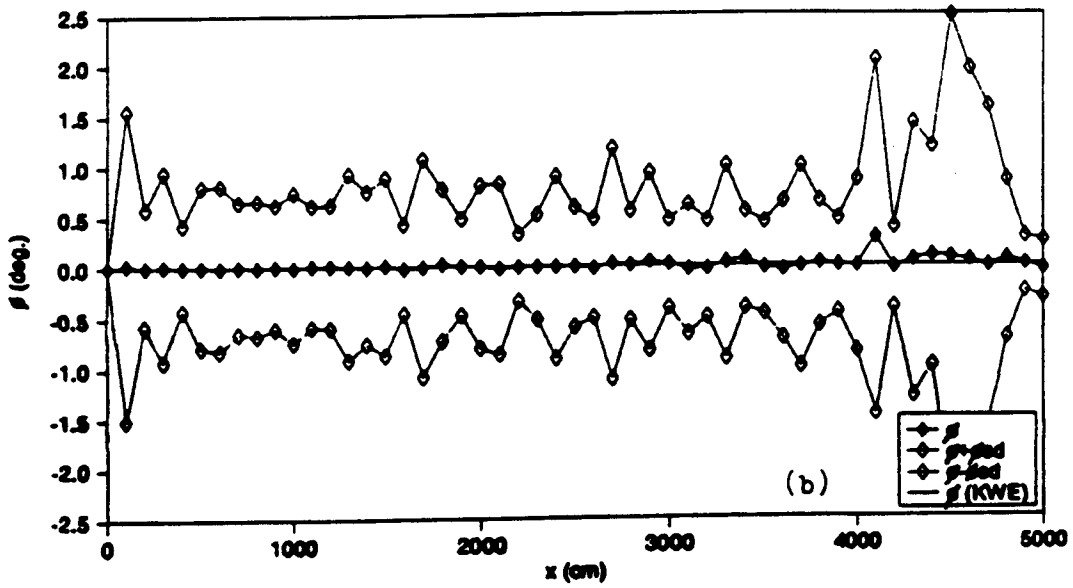

Figure 4.19 Comparison of the computed cross-slope mean profiles of depth, velocity and flow direction on surfaces with downslope increasing roughness and embedded randomness to those computed by assuming a uniform roughness $K_o = \mu_{Ko}$ for $S_x = .05$, $V_o = 10$cm/hr, $K_o = 512$, and $CV_{Ko} = .1$. where hsd = σ_h; Vsd = σ_V; ϕsd = σ_ϕ
a) depth; b) flow direction

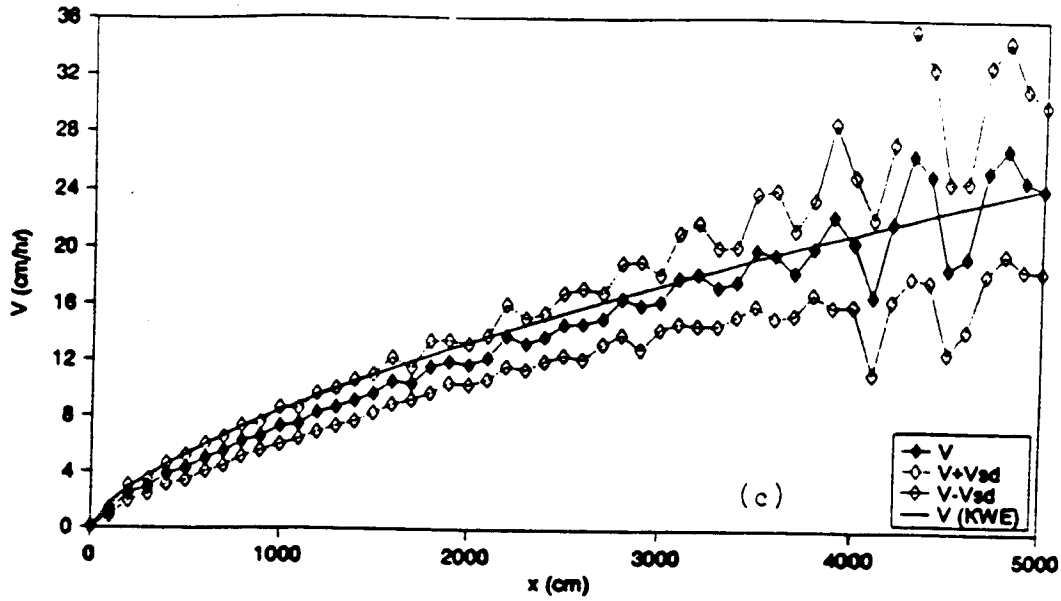

Figure 4.19 continued.
c) velocity

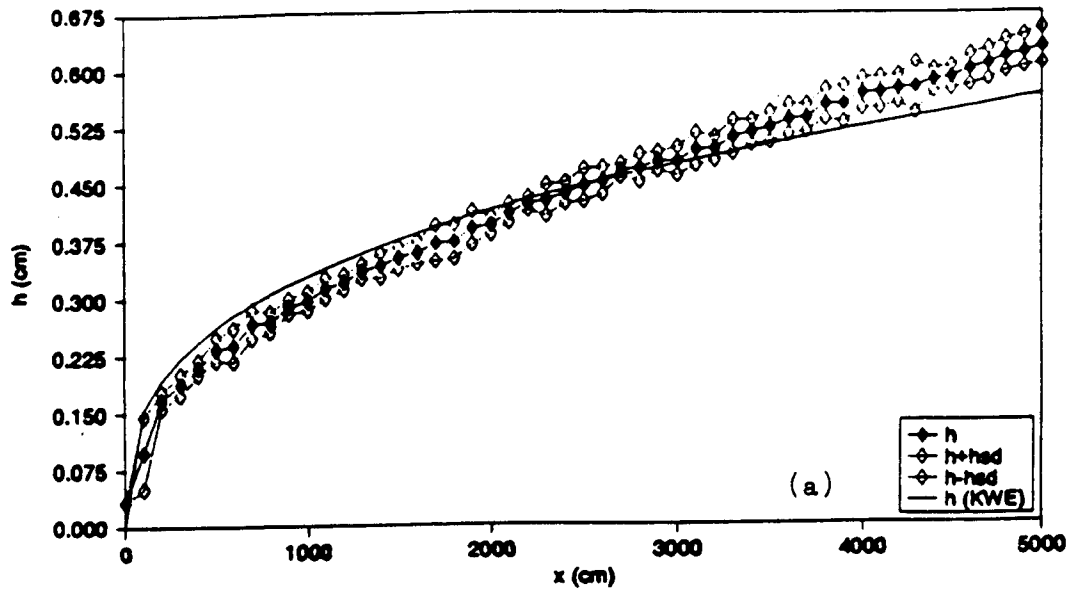

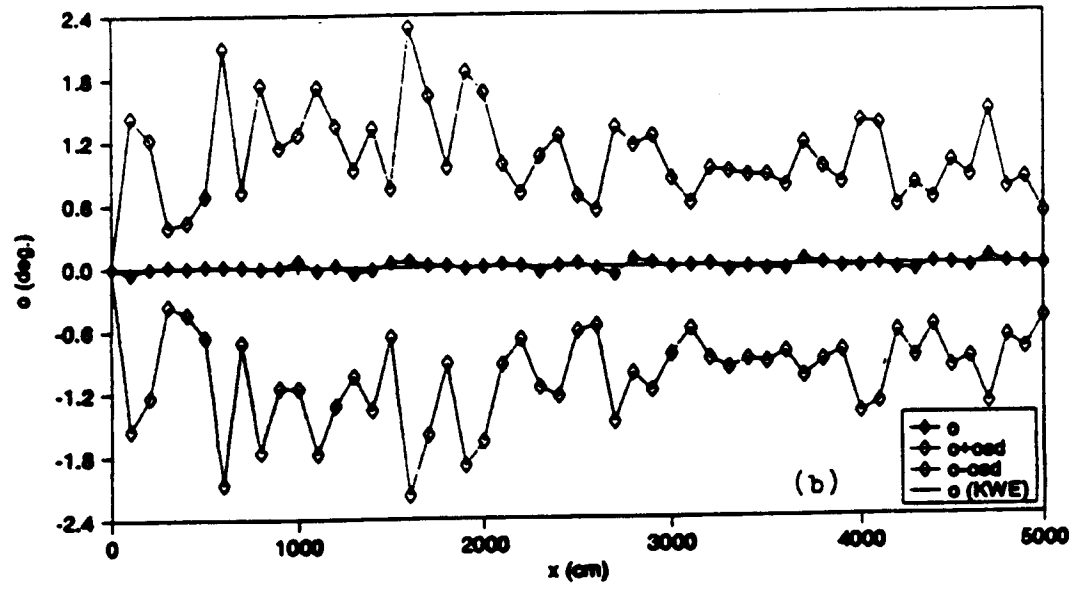

Figure 4.20 Comparison of the computed cross-slope mean profiles of depth, velocity and flow direction on surfaces with downslope decreasing roughness and embedded randomness to those computed by assuming a uniform roughness $K_o = \mu_{Ko}$ for $S_x = .05$, $V_o = 10$cm/hr, $K_o = 512$, and $CV_{Ko} = .1$. where hsd = σ_h; Vsd = σ_v; ϕsd = σ_ϕ
a) depth; b) flow direction

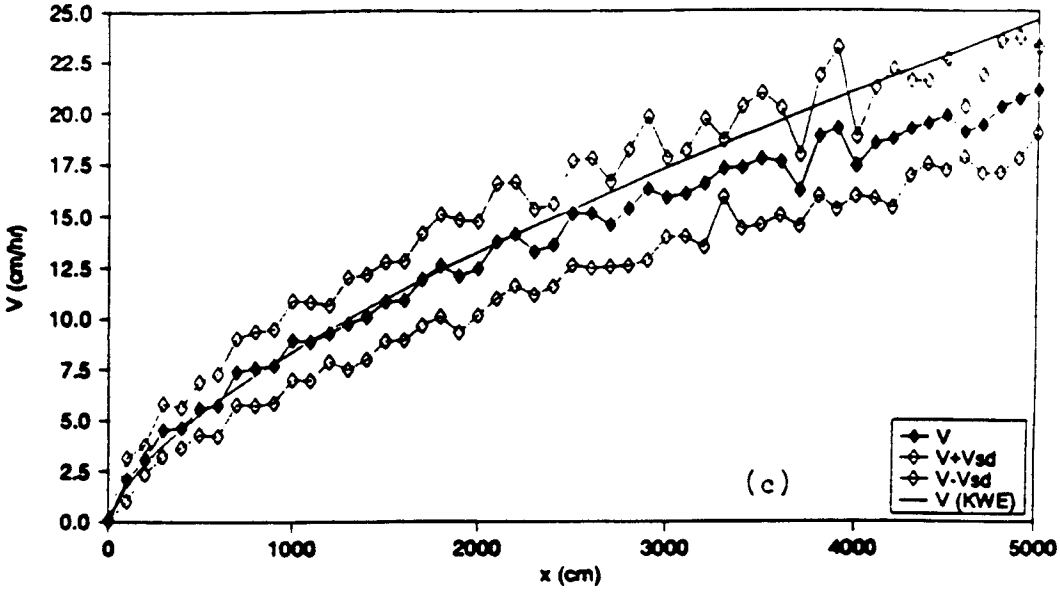

Figure 4.20 continued.
c) velocity

4.4.3 Effects of Hillslope Microtopography

1) Effects of two-dimensional corrugated microtopography

The effects of microtopography on hydrographs and flow fields are examined. The hydrographs from surface having two-dimensional microtopography with corrugations aligned both downslope and across the slope on a generally plane surface and those from corresponding smooth plane surfaces are shown in Figure 4.21. The computed hydrographs from the assumed planes having mean slope match those computed from the two-dimensional corrugated microtopographic surfaces quiet well. Clearly, the two-dimensional corrugated microtopography has no influence on the characteristics of the hydrograph. Although microtopographic heights slow down the flow velocity immediate upslope from them, they force the flow to concentrate into nearby depression paths where the flow is deeper and velocity is faster. For these cases, the geometry of the microtopographic heights and depressions are symmetrical. Therefore, the overall runoff rate and the "apparent" flow resistance, i.e., the overall flow resistance of the surface by back fitting the hydrograph, have not been altered due to the existence of the microtopography.

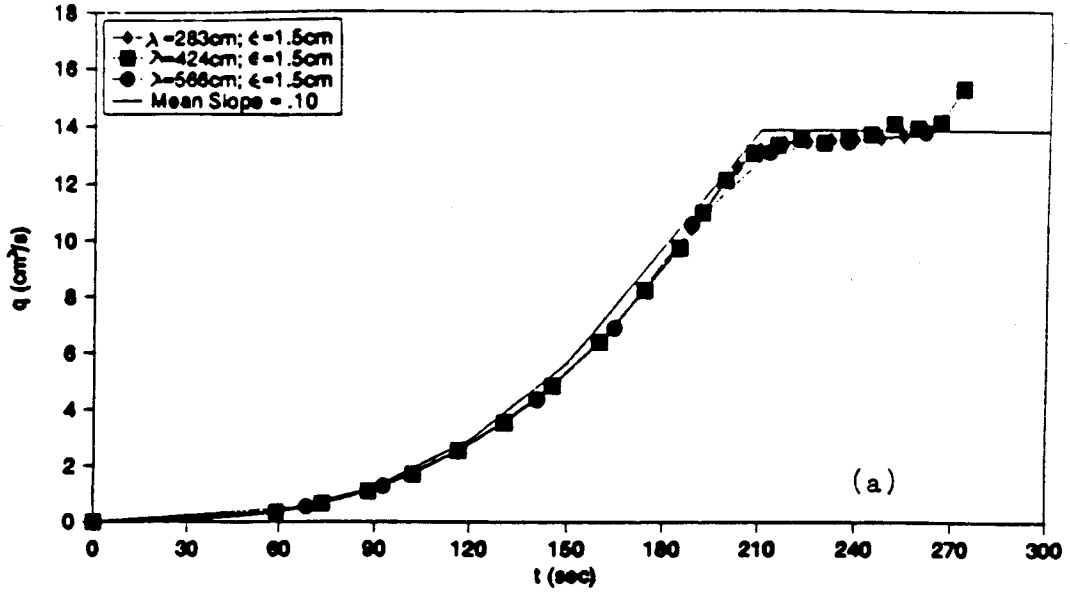

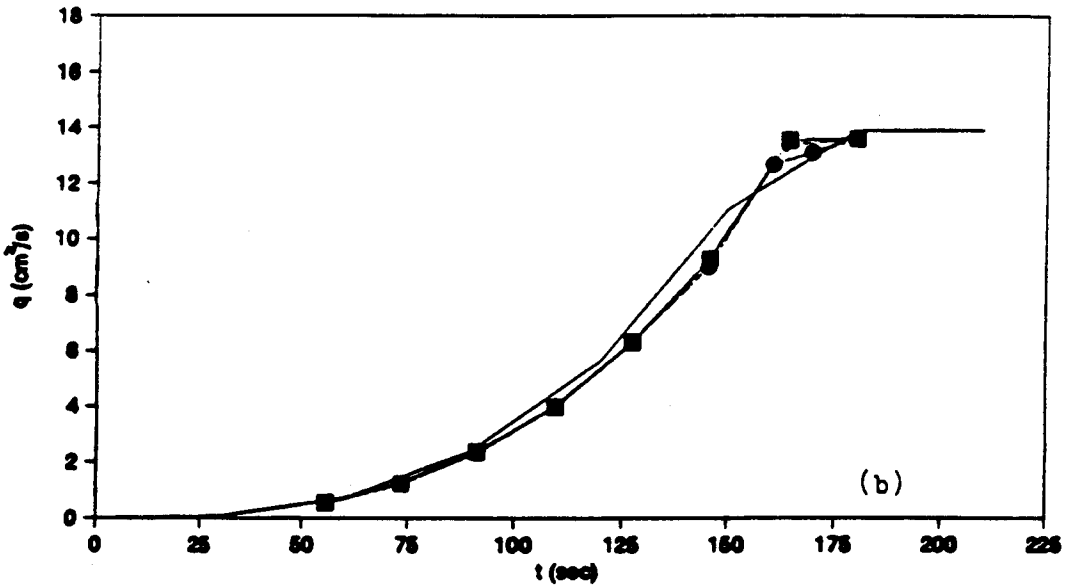

Figure 4.21 Comparison of computed hydrographs from surfaces with corrugations aligned in both the downslope and cross-slope directions to those computed by assuming a plane surface with a mean slope.
a) S_x = .10; V_o = 5cm/hr; K_o = 1000
b) S_x = .10; V_o = 10cm/hr; K_o = 512

These results are obtained on corrugated surfaces with large wave length ($\lambda > 2.83$ m) and relative small amplitude ($\epsilon < 6$ cm). In the simulations, the microtopographic heights are completely inundated. If the microtopographic amplitude, ϵ, is so large that the microtopographic heights protrude out of the flow, or if the corrugated wave length becomes so small that the microtopographic heights are acting as individual blockages, then the surface resistance to the flow would increase, and the rise of the hydrographs would be delayed. Unfortunately, due to the limitation of the numerical model, these cases could not be simulated.

In addition to the scales of microtopographic amplitudes and wave lengths, the geometric configurations of microtopography will also influence the characteristics of hydrographs. If the configuration is favorable for the convergence of flow, the effects of microtopography are to reduce the overall or "apparent" resistance of the surface; otherwise, the effects of microtopography are to increase the "apparent" resistance of the surface. These can be illustrated by the following example.

In this example, HyNuM is applied to two kinds of idealized microtopographic surfaces generated with equation (68). The first surface has corrugations aligned only downslope, and the second has corrugations aligned only across the slope (Figure 4.22). Clearly, the

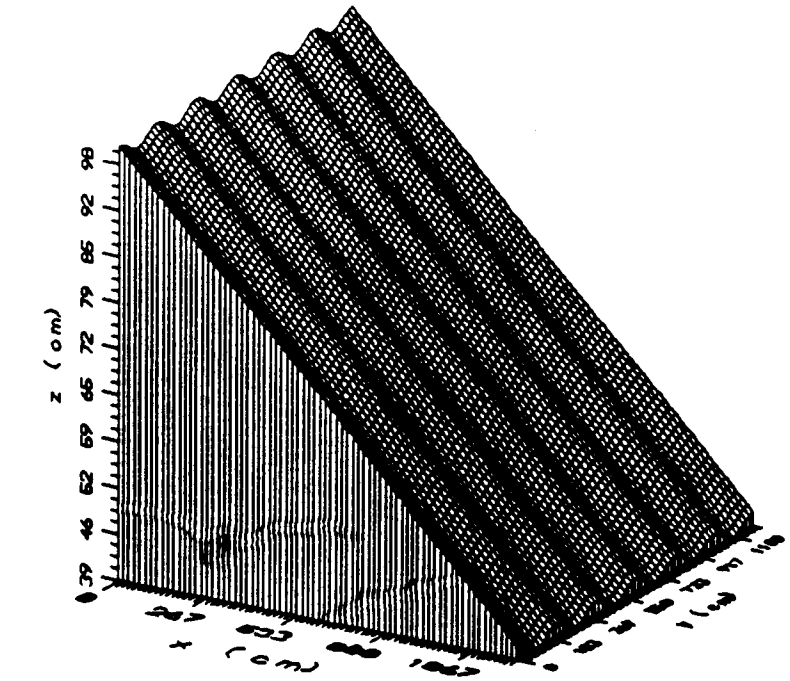

Lo = 1200cm; Sx = 5%; λy = 200cm; ϵ = 4cm

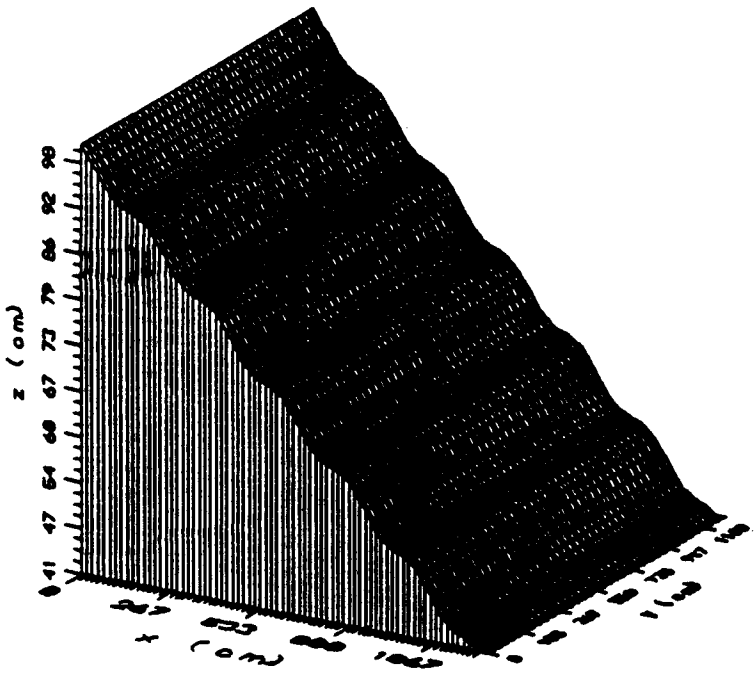

Lo = 1200cm; Sx = 5%; λx = 200cm; ϵ = 4cm

Figure 4.22 Surfaces with corrugations aligned only in the downslope or cross-slope direction.

geometric configuration of the first microtopographic surface is more favorable to the convergence of flow than is the second surface. The hydrographs generated from the two surfaces along with those computed from the assumed homogeneous planes are shown in Figure 4.23. These hydrographs were all generated with surface roughness parameter, K_o = 512.

For equilibrium hydrographs, the runoff reaches steady state faster on the first surface than those on the second surface or the assumed plane. The convergence of flow on the first surface results in a deeper and faster concentrated flow, and therefore, quicker runoff. To match the hydrograph generated on the first surface with that from the assumed homogeneous plane, the value of K_o should be reduced from 512 to 380; the "apparent" flow resistance due to the existence of the microtopography is reduced.

The change of K_o required to match the hydrograph from the second surface with that from the equivalent homogeneous plane is insignificant. As the flow approaches the "roll-wave" type microtopographic mount, while the velocity decreases, the depth increases; as the water flows over the microtopographic mount, although its velocity increases the flow depth becomes smaller. Since the flow velocity and depth compensate each other, the resultant flow rate has not been significantly altered. The effect of microtopography is greater for non-

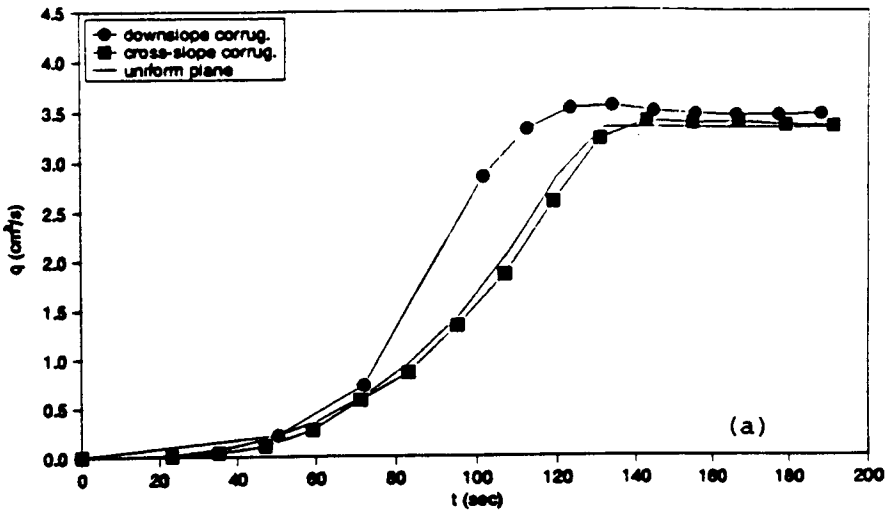

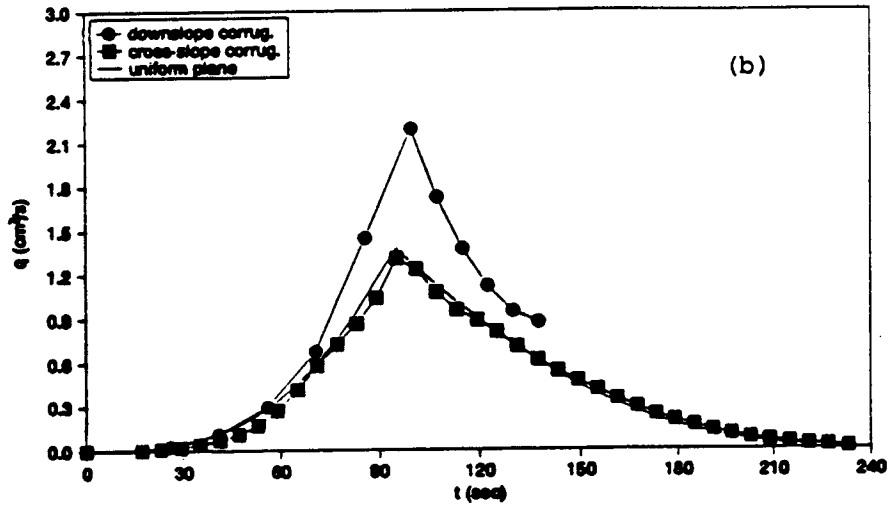

Figure 4.23 Comparison of computed hydrographs from two surfaces (Fig. 4.22) with corrugations aligned in the downslope and cross-slope directions for S_x = .05, V_o = 10cm/hr, and L_o = 1200cm.
a) equilibrium case
b) non-equilibrium case

equilibrium. The flow peak generated from the first surface is much higher than that computed from the second surface and the plane. The flow peak from the plane is slightly higher than that from the second surface.

For these cases, the assumed homogeneous plane may not be used in hydrograph prediction, because microtopography on natural hillslopes may take many forms. The effects of two natural microtopographic surface will be demonstrated later.

The effects of the two-dimensional microtopography with corrugations aligned both downslope and across the slope on the characteristics of overland flow fields is examined next. Two typical flow fields generated on the two-dimensional corrugated microtopographic surfaces are shown in Figure 4.24. The impact of microtopography on the flow directions is much stronger than is the case with spatially varying infiltration and surface roughness. The profiles of the mean cross-slope flow depth, velocity and flow direction along with those computed from the corresponding plane surfaces with mean slopes are shown in Figure 4.25. The depth, velocity, and flow direction simulated from the variable surfaces vary significantly around their mean values. The variability of the flow fields, represented by the values of CV_{*h}, σ_{*h}, CV_{*V}, σ_{*V} and $\sigma_{*\phi}$, is shown in Table 4.7. While the variations of depth and velocity for the cases simulated are about

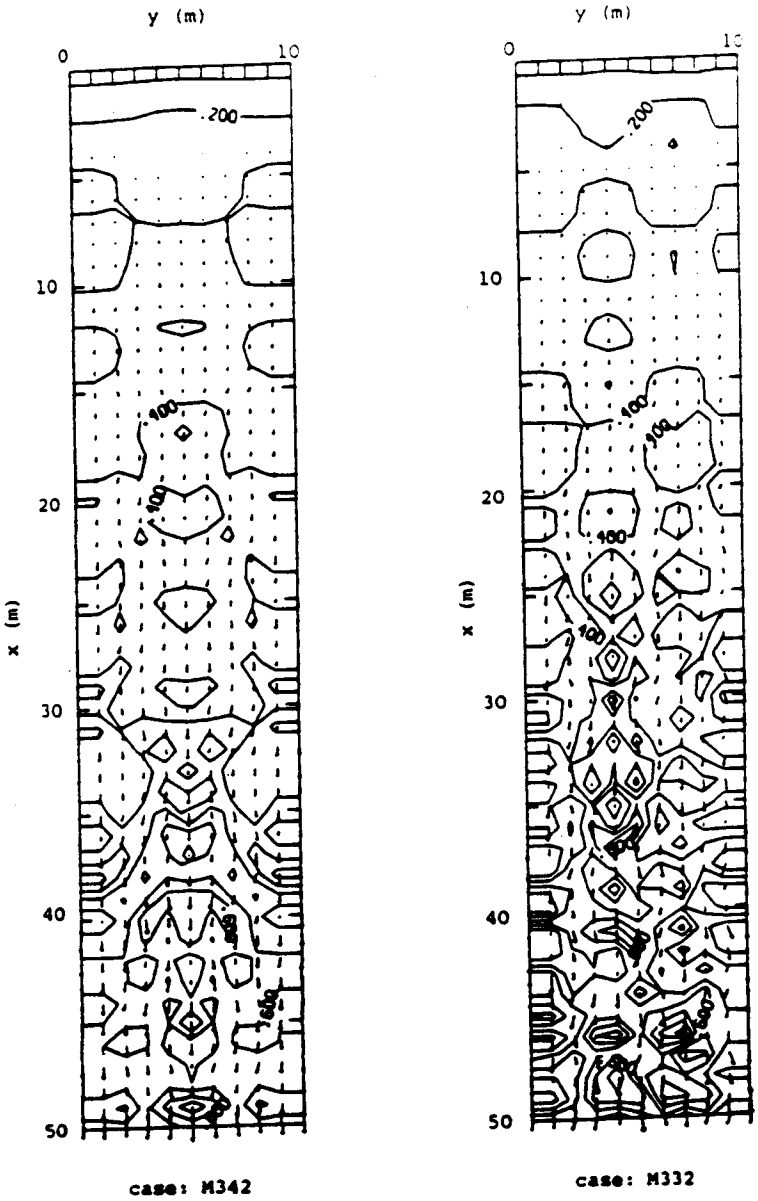

Figure 4.24 Computed steady state flow depth and velocity fields from surfaces with corrugations aligned in both the downslope and cross-slope directions. The contour lines represent depth in cm and vectors represent velocity in cm/s.

M342: $S_x = .05$; $V_o = 10$cm/hr; $K_o = 512$; $\epsilon = 4$cm; $\lambda_x = \lambda_y = 566$cm

M332: $S_x = .05$; $V_o = 10$cm/hr; $K_o = 512$; $\epsilon = 4$cm; $\lambda_x = \lambda_y = 424$cm

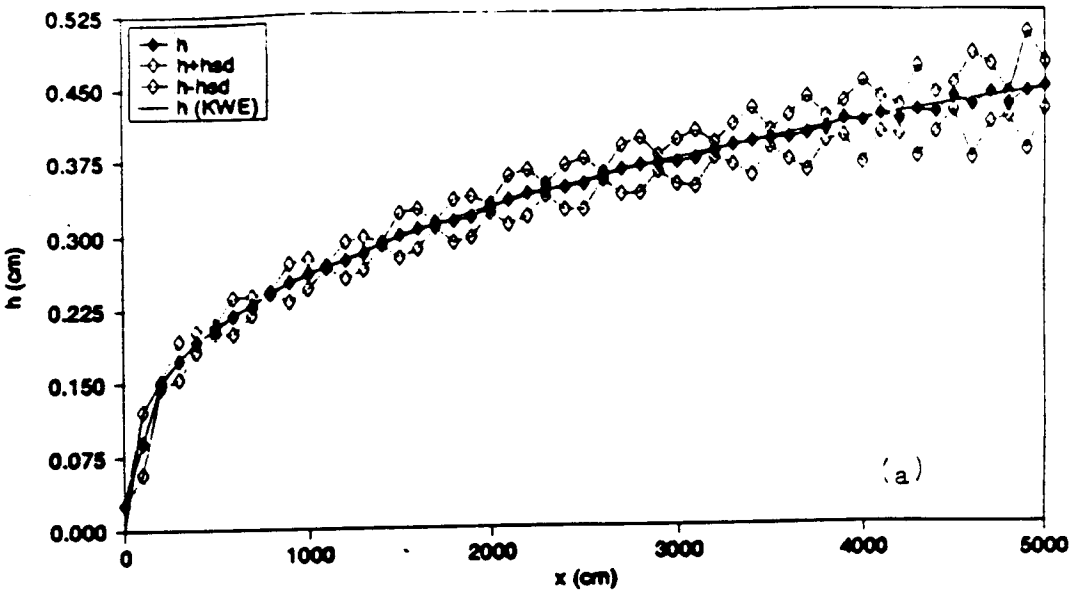

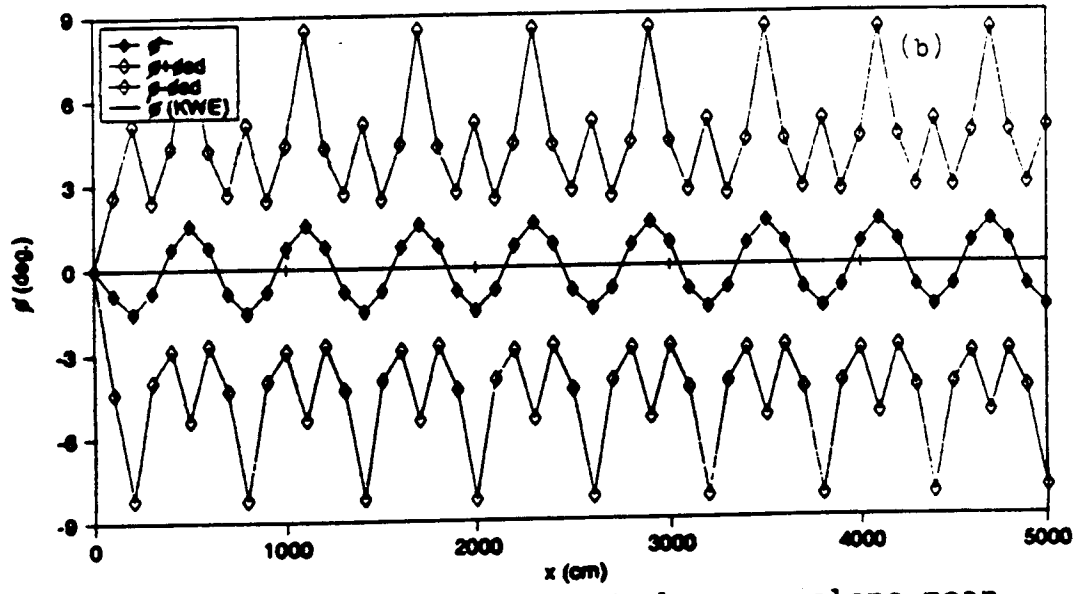

Figure 4.25 Comparison of the computed cross-slope mean profiles of depth, velocity and flow direction from surfaces with corrugations aligned in both the downslope and cross-slope directions to those computed by assuming a uniform plane with a mean slope for S_x = .10, K_o = 1000, V_o = 5cm/hr, and ϵ/λ = .0091.
where hsd = σ_h; Vsd = σ_v; ϕsd = σ_ϕ
a) depth; b) flow direction

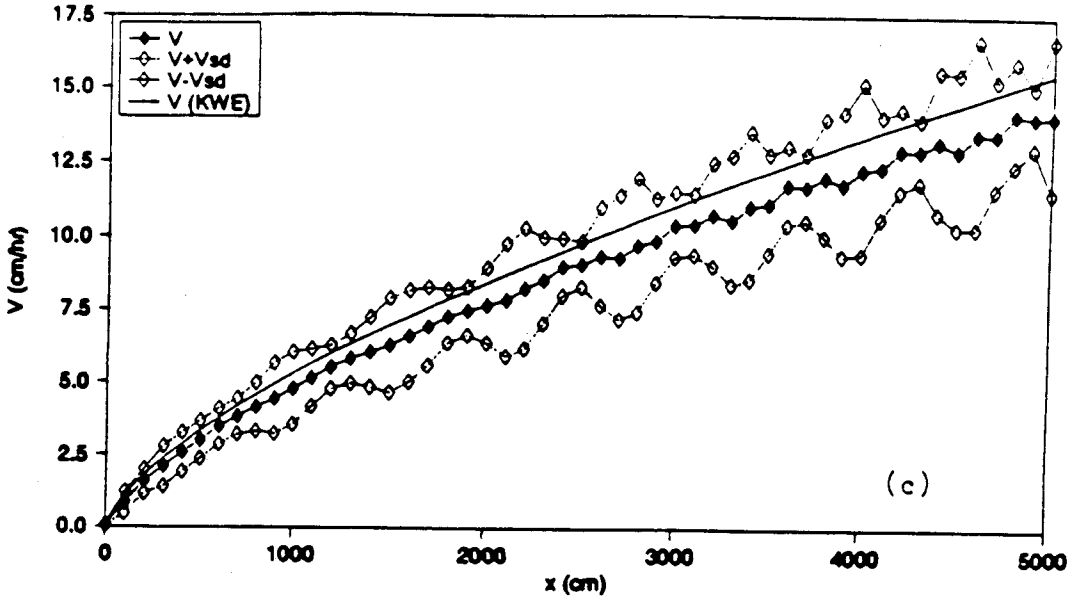

Figure 4.25 continued.
c) velocity

Table 4.7 Computed mean cross-slope deviations in depth (σ_{*h}, CV_{*h}), velocity (σ_{*v}, CV_{*v}) and flow direction ($\sigma_{*\phi}$) from the two-dimensional corrugated microtopography

CASE	ϵ (cm)	$\lambda_x=\lambda_y$ (cm)	σ_{*h} (cm)	CV_{*h}	σ_{*v} (cm/s)	CV_{*v}	$\sigma_{*\phi}$ (deg)
r = 15 cm/hr; S_x = 5%; K_s = 5 cm/hr; K_o = 512							
M321	2	283	.0405	.0874	2.76	.180	5.07
M331	2	424	.0474	.1010	3.07	.204	4.73
M341	2	566	.0384	.084	2.57	.182	3.30
M322	4	283	.0746	.1640	4.25	.277	9.96
M332	4	424	.0886	.1880	5.00	.303	9.54
M342	4	566	.0620	.1350	3.47	.227	3.56
M323	6	283	-	-	-	-	-
M333	6	424	.1030	.2260	5.58	.344	14.03
M343	6	566	.0796	.174	3.74	.239	9.73
r = 15 cm/hr; S_x = 5%; K_s = 5 cm/hr; K_o = 1000							
M361	2	283	.0376	.0673	1.56	.142	5.13
M371	2	424	.0321	.0565	1.41	.131	4.69
M381	2	566	.0296	.0525	1.36	.129	3.26
M362	4	283	.0729	.1290	2.47	.211	9.82
M372	4	424	.1010	.1780	3.28	.200	9.81
M382	4	566	.0567	.100	1.68	.150	6.53
M363	6	283	-	-	-	-	-
M373	6	424	.1011	.1780	3.28	.260	14.14
M383	6	566	.0867	.1540	2.25	.187	9.90
r = 15 cm/hr; S_x = 10%; K_s = 5 cm/hr; K_o = 512							
M21	2	283	.0326 (.501)	.0862 (.110)	4.77 (5.33)	.247 (.321)	2.66 (2.81)
M31	2	424	.0473	.1000	5.18	.274	2.43
M41	2	566	.0245	.0679	3.85	.215	1.62
M22	4	283	.0383	.1050	4.95	.260	6.75
M32	4	424	.0448	.1200	5.19	.275	4.68
M42	4	566	.0237	.0650	3.88	.213	3.15
M23	6	283	.0384	.1050	4.96	.261	7.36
M33	6	424	.0501	.1390	5.59	.285	7.36
M43	6	566	.0459	.1250	5.18	.271	5.27

Table 4.7 continued

r = 15 cm/hr; S_x = 10%; K_s = 5 cm/hr; K_o = 1000							
M61	2	283	.0260	.0544	2.79	.187	2.57
M71	2	424	.0258	.0548	2.63	.184	2.35
M81	2	566	.0244	.0518	2.43	.175	1.62
M62	4	283	.0356	.0823	3.00	.210	6.80
M72	4	424	.0371	.0798	2.91	.199	4.66
M82	4	566	.0279	.0619	2.44	.176	3.18
M63	6	283	.0476	.1050	3.05	.205	7.19
M73	6	424	.0482	.1040	3.29	.213	6.99
M83	6	566	.0358	.0800	2.53	.180	4.74
r = 15 cm/hr; S_x = 10%; K_s = 10 cm/hr; K_o = 512							
M101	2	283	.0097	.0339	2.10	.186	2.44
M111	2	424	.0100	.0342	2.07	.185	2.31
M121	2	566	.0092	.0318	1.99	.180	1.60
M102	4	283	.0246	.0868	2.60	.231	6.74
M112	4	424	.0237	.0802	2.35	.213	4.67
M122	4	566	.0180	.0630	2.07	.190	3.15
M103	6	283	.0247	.0650	2.56	.210	6.94
M113	6	424	.0270	.0935	2.36	.210	6.94
M123	6	566	.0226	.0795	2.13	.193	4.71

as those from surfaces with spatially varying K_s or K_o, the variations of flow directions are about one order of magnitude greater than those from spatially varying K_s or K_o surfaces.

For given microtopographic wave length, λ, the variability of flow fields, represented by the values of CV_{*h}, σ_{*h}, CV_{*V}, σ_{*V} and $\sigma_{*\phi}$, increases with increasing microtopographic amplitudes. For a given microtopographic amplitude, as the wave length of the microtopography is shortened, the variability of flow direction, $\sigma_{*\phi}$, increases, while the variation trends for flow depth and velocity are not consistent. For some cases, the values of CV_{*h}, σ_{*h}, CV_{*V} and σ_{*V} computed with λ = 424 cm are even greater than those computed with λ = 283 cm.

These results may not reflect the true impacts of microtopography on sheet flow. One would expect that as the wave length of the microtopography is reduced, with a fixed amplitude, the surfaces become more rugged, and therefore the spatial variation of the flow would be greater. The error may be introduced by the spatial resolution of the numerical solution. In the simulation, the same grid size of $\Delta x = \Delta y$ = 1 m was used for numerical solution of all three wave lengths. As the wave length of the microtopography gets shorter, the spatial resolution of the computational mesh grid is poorer. The net result is that more of the original features of the

microtopographic surfaces are smoothed out. This appears to be the reason that the flow fields computed on surfaces with λ = 283 cm have less variability than those computed from surfaces with λ = 424 cm. Since there are smoothing effects resulting from the computational spatial resolution, the microtopography with λ = 424 cm is rougher than that with λ = 566 cm. Consequently, the computed flow from the surfaces with λ = 424 cm are more variable than those from surfaces with λ = 566 cm. The spatial resolution error can be reduced by increasing the number of grid points, i.e., reducing the grid sizes. This is illustrated by case M21 in Table 4.7. The values inside () in Table 4.7 were simulated using $\Delta x = \Delta y = 0.5$ m. With this finer grid, the error introduced by the spatial resolution of the numerical solution was clearly reduced. Due to the constraints in time and computer availability, simulations with this finer mesh have not been done for the other cases.

The variabilities of the flow fields due to microtopography are different depending on excess rainfall rate, slope, and surface roughness. Comparison of cases M61-83 with cases M101-123 shows that as the excess rainfall rate increases, the spatial variability of the flow, reflected by all the values of CV_* and σ_*, increases. These results again show that deeper flow and greater flow velocity resulting from greater excess

rainfall rate cause more spatial variability in the flow. The influence of slope gradient on the spatial variability of the flow due to microtopography is different from those due to spatially variable K_s or K_o. The results show that as the slope gradient becomes smaller, while the variability of velocity, σ_{*V}, is reduced, the variability of flow depth, CV_{*h} and σ_{*h}, become larger even though the flow is deeper. The influence of slope on flow direction due to microtopography is similar to the influence due to spatially variable K_s or K_o, that is, as the slope becomes smaller, the variability of flow direction $\sigma_{*\phi}$ become larger. As the surface roughness, K_o, increases, the variability of the flow, represented by all the values of σ_* and CV_*, decreases. For the reason given in section 4.4.1, it is beyond the scope of this work to explain fully the physics behind these findings.

Above simulation results show strong influences of microtopography on overland flow. For surfaces with the corrugation aligned in the downslope direction, the characteristics of the hydrograph have been significantly affected. However, for the two-dimensional corrugated microtopography simulated, the influences of the microtopography are mainly on spatial variability of flow fields, and the influence on the hydrograph shape is negligible. For these cases, the KWE with an average slope can be used to predict the outflow hydrograph and the mean

characteristics profiles of the flow. However, spatial variability of the flow fields can not be predicted by the KWE with the assumed homogeneous planes.

2) Characteristics of sheet flow on natural microtopography

The patterns of the microtopography on natural hillslopes are complicated, and so are the responses of overland flow on such surfaces. To examine the impacts of microtopography of natural hillslope surfaces on the characteristics of overland flow, the model was applied to the two natural hillslope surfaces shown in Figure 4.2. These two microtopographic surfaces are chosen from the field study of Aubry (1984). Both of the plots are 6.0 m long and 2.5 m wide, and the average downslope gradients are 4.07% for plot KR-9 and 4.2% for plot KR-10. For numerical simulation, both plots were subjected to a hypothetical rainfall intensity of 15 cm/hr. An average infiltration rate of 5 cm/hr was assumed. In the simulation, the same mesh size as that used in field measurement, Δx = 0.5 m and Δy = 0.25 m, was chosen as the computational mesh size. Surface roughness K_o = 5000 was chosen for the simulation; the actual surfaces are short grass prairie surfaces.

The equilibrium hydrographs from the two plots along with those from the corresponding plane surfaces with the

average slopes are shown in Figure 4.26. One can see that the shapes of the hydrographs computed from variable microtopographic surfaces and the corresponding plane surfaces are different. The hydrograph for plot KR-9 rises to steady state much slower than for the corresponding plane surface. The ratio of t_p^1/t_p^o is about 1.48 (Table 4.8). The time to steady state from plot KR-10 is also longer than that from the corresponding plane surface, and the ratio of t_p^1/t_p^o is about 1.16 (Table 4.8). The hydrograph rise from plot KR-10 is initially faster then slower than that from the corresponding plane surface. This initial quick rise of the hydrograph is presumably caused by early concentrated runoff from the depression paths. In comparison with plot KR-10, plot KR-9 lacks concentrated depression paths, and therefore, there is no initial quick hydrograph rise from plot KR-9. For the simulated equilibrium hydrographs, the microtopographic effects of both plots give rise to the increase of the "apparent" flow resistance, and therefore, would increase the values of the back calculated surface roughness. To match the hydrographs from plots KR-9 and KR-10 by those computed from the corresponding planes, back fitted values of K_o would increase from 5000 to 9000 for plot KR-9 and 7800 for plot Kr-10.

The model was run to examine the influence of the microtopographic surfaces on non-equilibrium hydrograph,

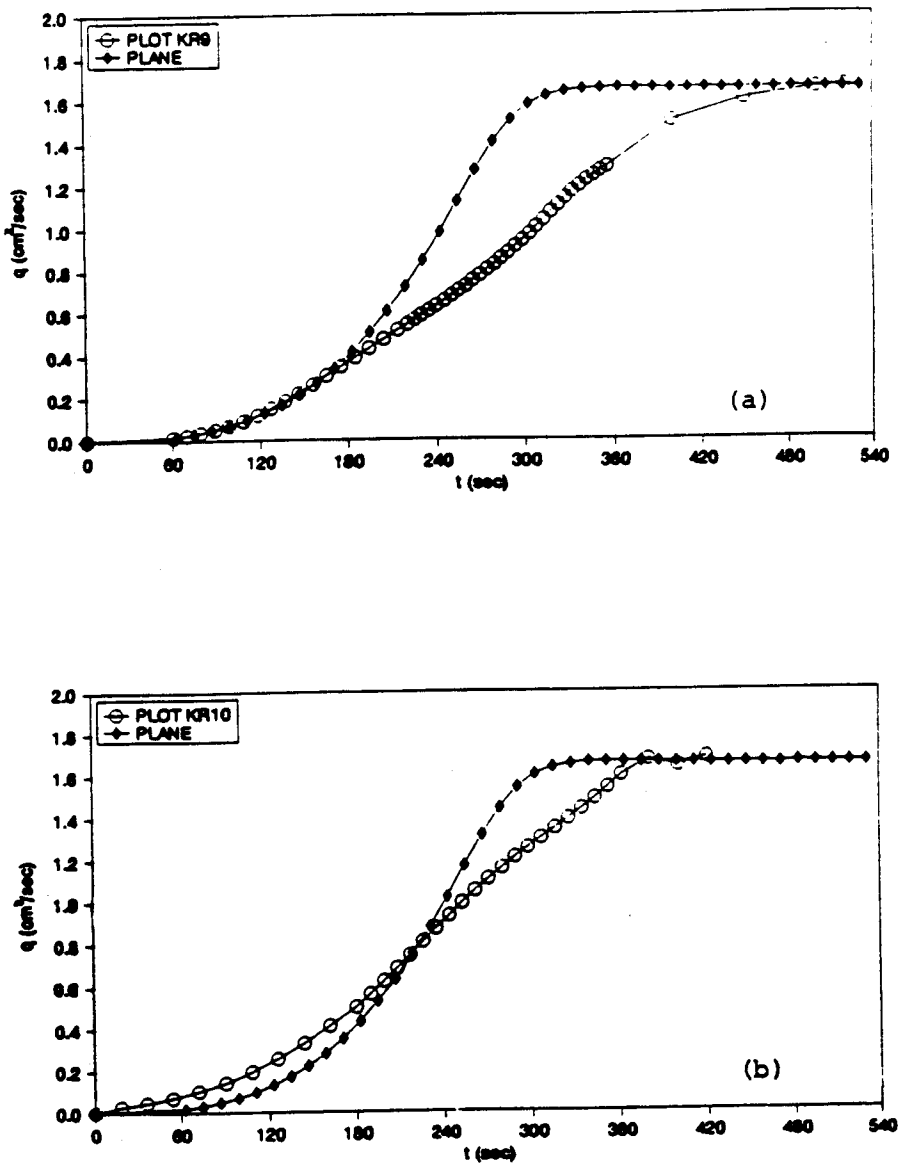

Figure 4.26 Comparison of computed steady state hydrographs from natual microtopographic surfaces to those computed by assuming a plane surface with a mean slope.
a) plot KR-9
b) plot KR-10

and the results are shown in Figure 4.27. The duration of rainfall was again taken as 75% of the time to steady state from the corresponding plane surfaces. For plot KR-9, the peak discharge occurred at the time of cessation of rainfall, the same as from the corresponding plane surface. However, the peak discharge from the microtopographic surface was smaller than computed from the corresponding plane surface. From Table 4.8, the ratio of q_p^1/q_p^0 is about 0.78. For plot KR-10, the time to peak discharge is also about at the end of rainfall but the peak discharge is higher than computed from the corresponding plane surface. From Table 4.8, the ratio of q_p^1/q_p^0 is about 1.1.

The results indicate that large errors may be generated in prediction of hydrographs on natural hillslopes if a one-dimensional model with the averaged slope is used. This is different from the cases of the two-dimension corrugated-microtopographic surfaces above, where the hydrographs computed for the corrugated microtopography were about same as those computed from the corresponding plane surfaces.

The computed flow fields for the two plots are shown in Figure 4.28. These flow fields clearly reflect the impact of the microtopography. Figures 4.29 and 4.30 shows the comparison of the averaged cross-slope depth, velocity and flow directions simulated on the two microtopographic

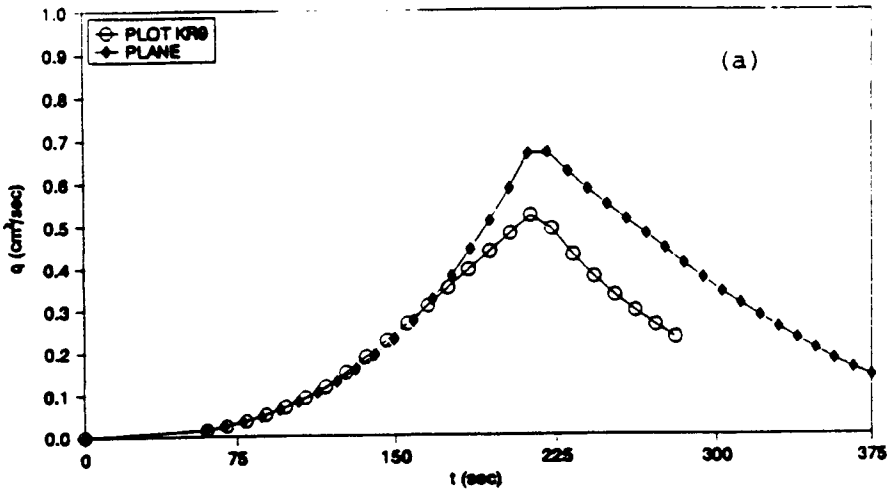

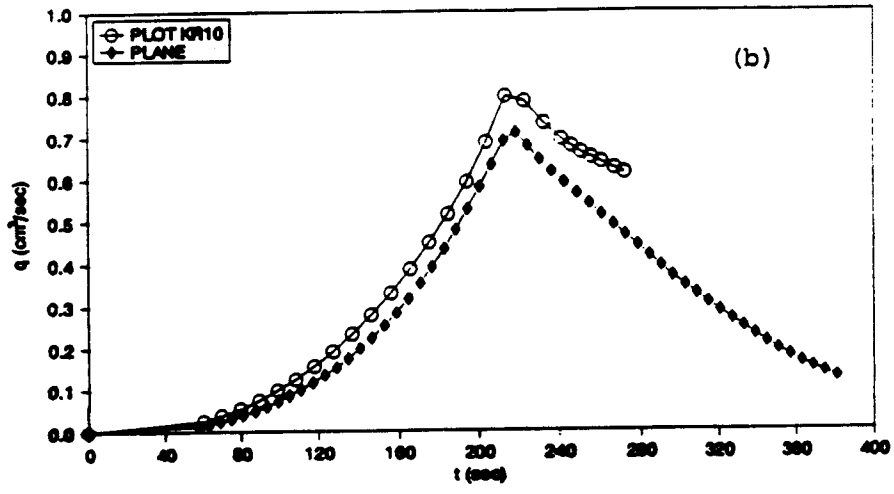

Figure 4.27 Comparison of the computed hydrographs from natual microtopographic surfaces to those computed by assuming a plane surface with a mean slope.
a) plot KR-9
b) plot KR-10

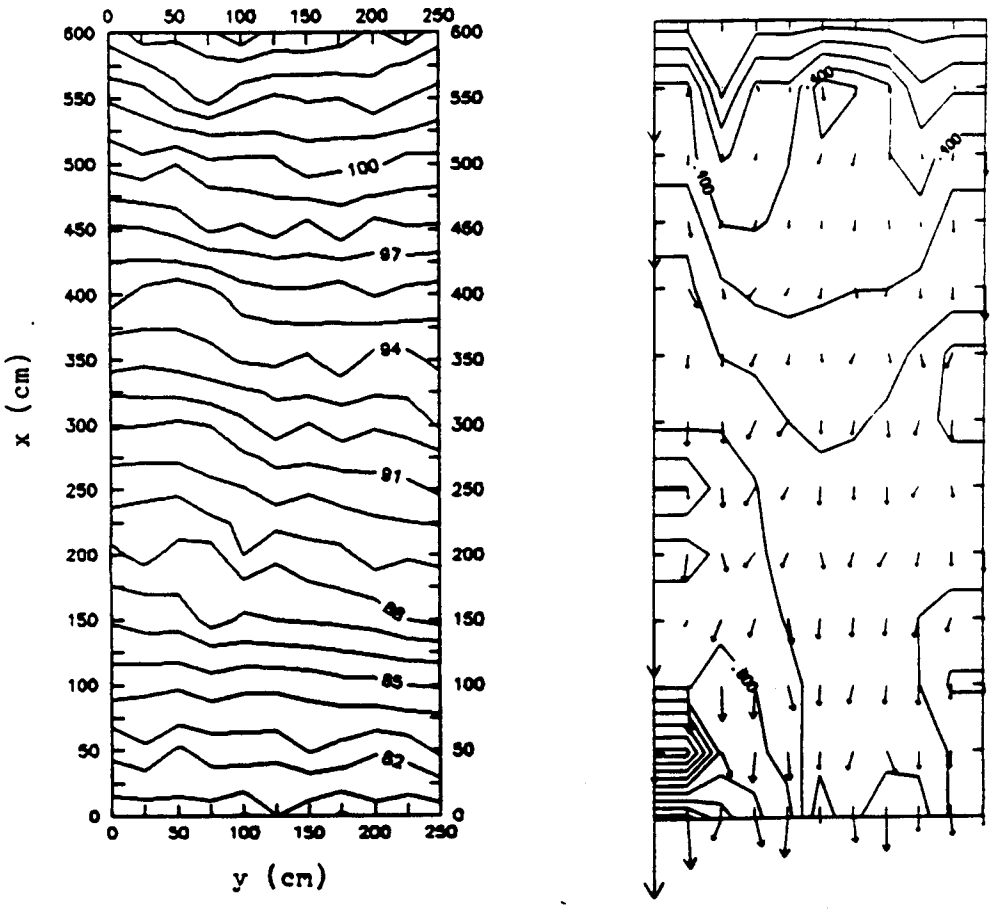

Figure 4.28 Computed steady state flow depth and velocity fields from natural microtopography. The contour lines represent depth in cm and vectors represent velocity in cm/s.
a) plot KR-9

Plot: KR-10

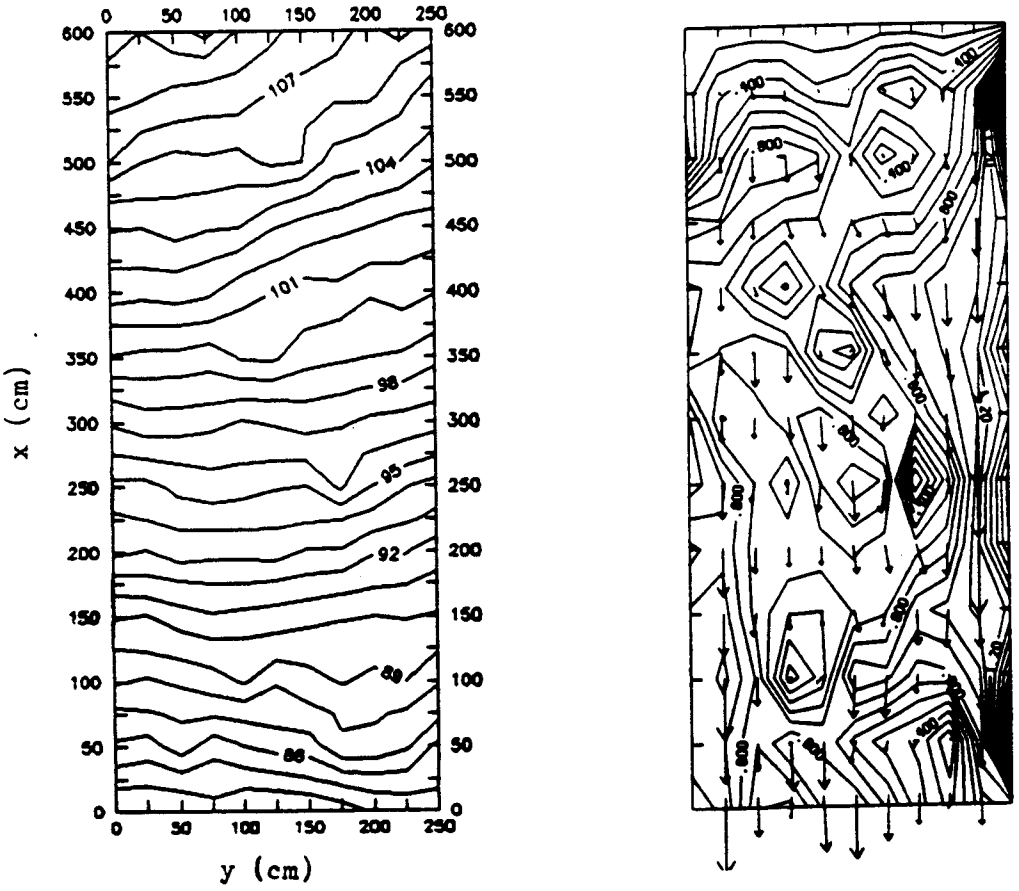

Figure 4.28 continued.
b) plot KR-10

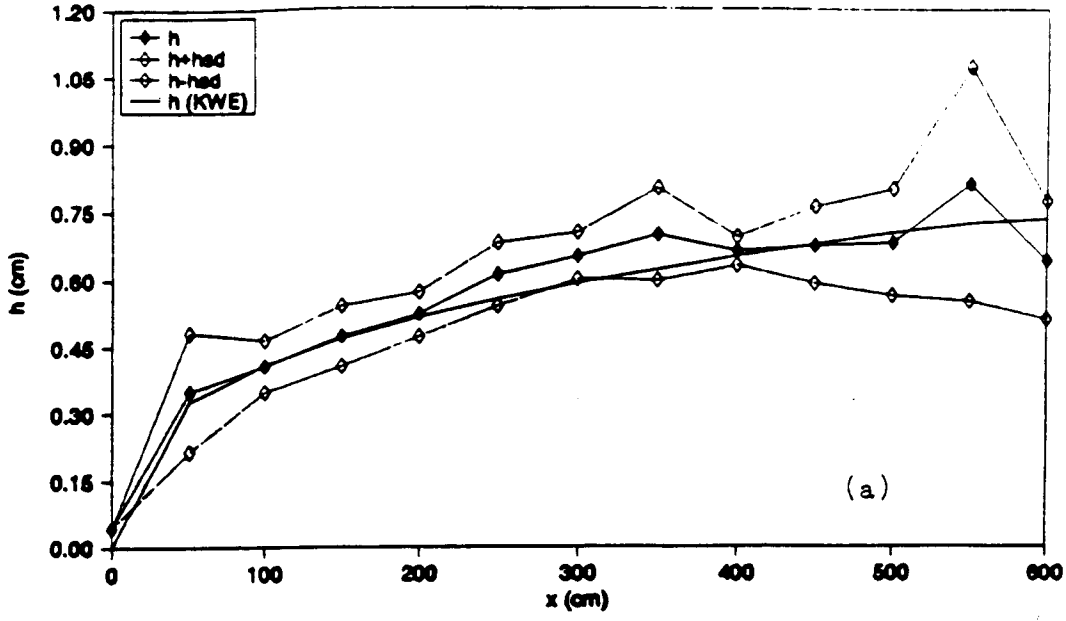

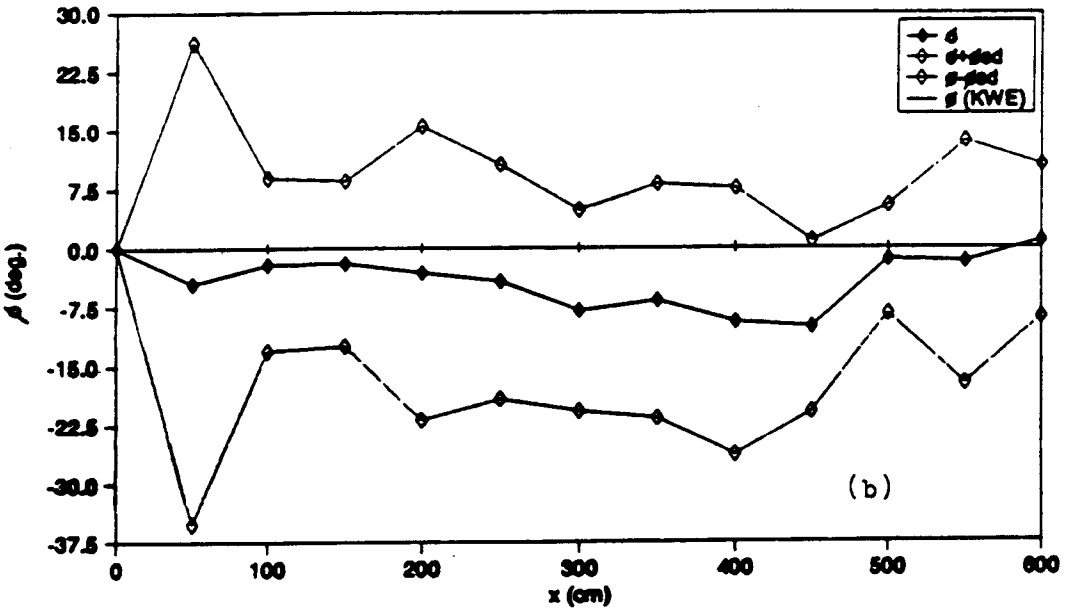

Figure 4.29 Comparison of the computed cross-slope mean profiles of depth, velocity and flow direction from the microtopography of plot KR-9 to those computed by assuming a uniform plane with a mean slope. where hsd = σ_h; Vsd = σ_V; ϕsd = σ_ϕ
a) depth; b) flow direction

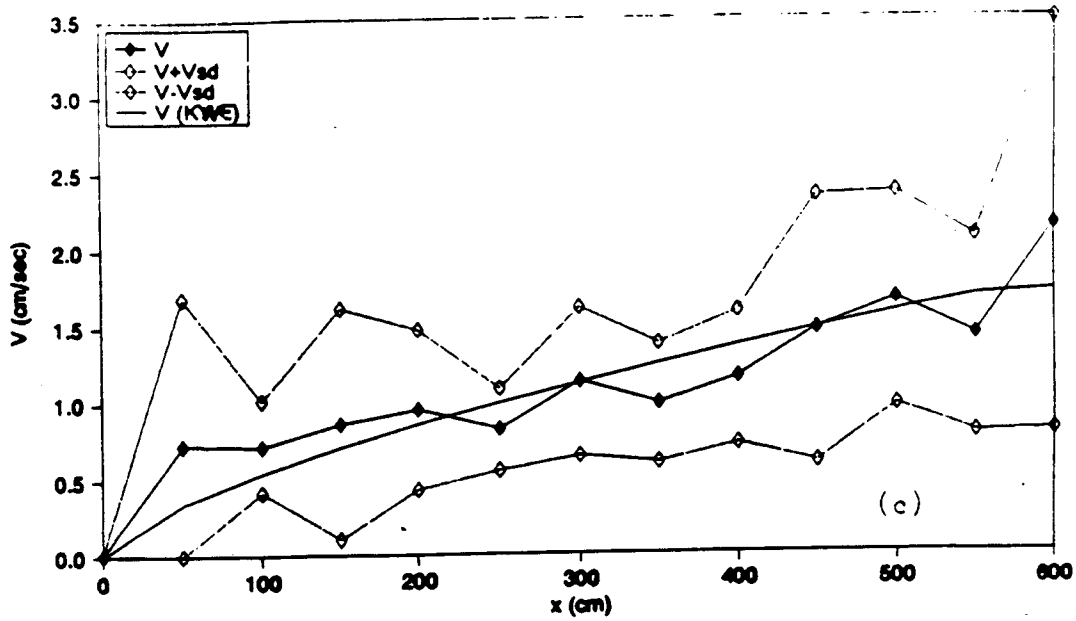

Figure 4.29 continued.
c) velocity

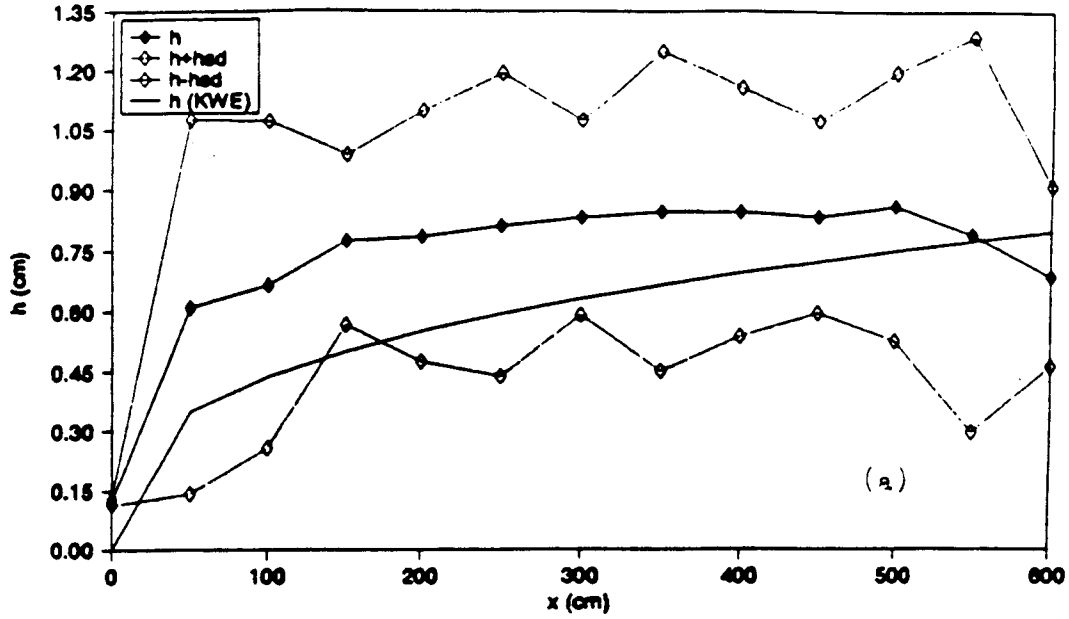

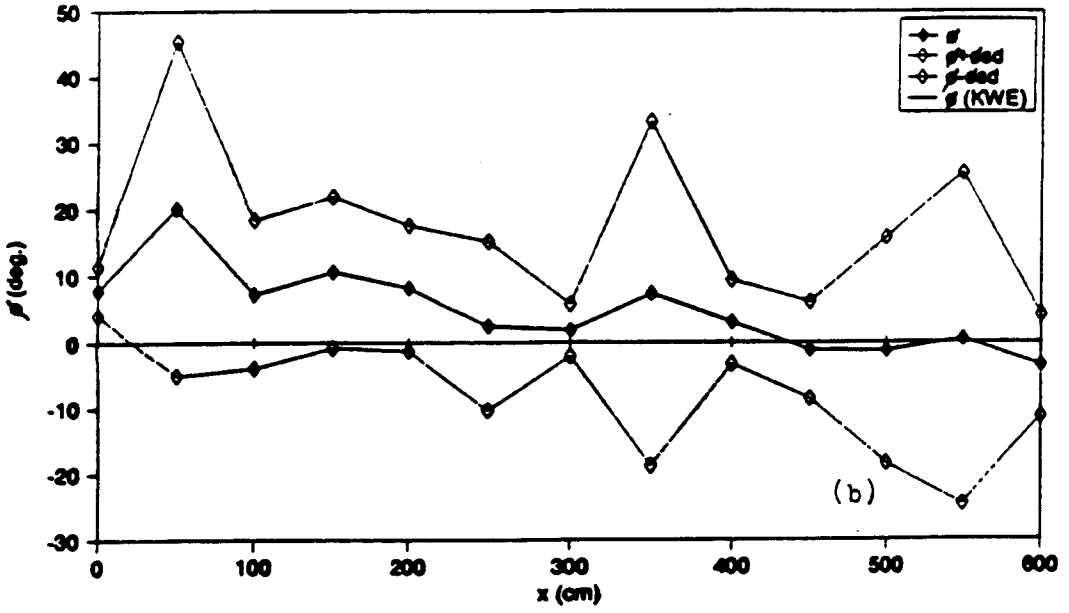

Figure 4.30 Comparison of the computed cross-slope mean profiles of depth, velocity and flow direction from the microtopography of plot KR-10 to those computed by assuming a uniform plane with a mean slope. where hsd = σ_h; Vsd = σ_V; ϕsd = σ_ϕ
a) depth; b) flow direction

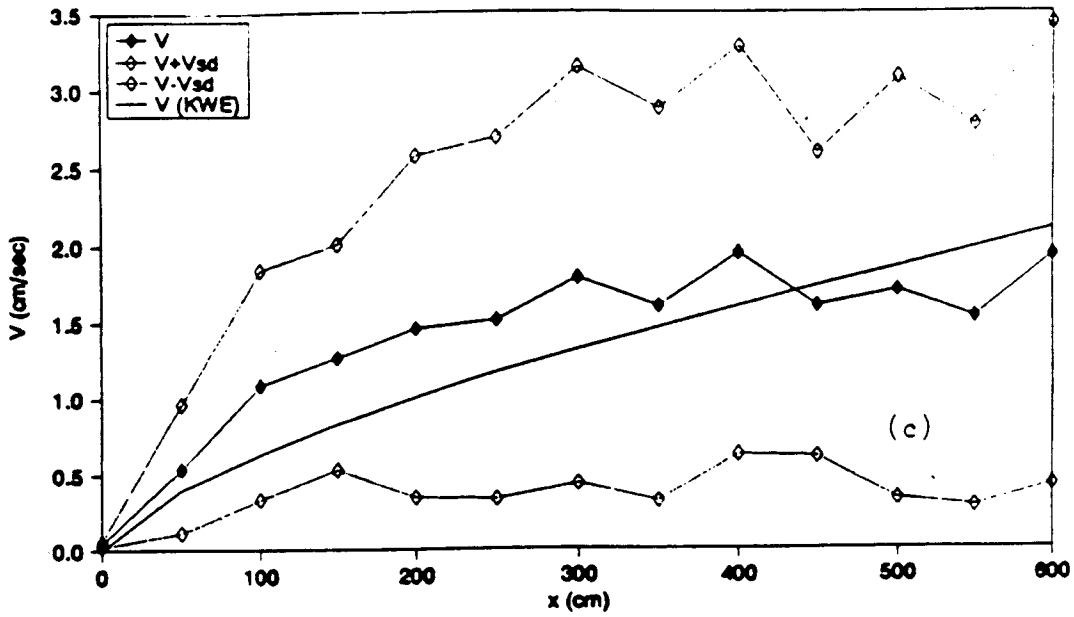

Figure 4.30 continued.
c) velocity

surfaces and those computed from the assumed plane surfaces with the averaged slopes. The results show that the depth, velocity, and flow directions on the variable microtopography have significant deviations from their cross-slope mean values. From Table 4.9, the values of CV_{*h} and CV_{*V} for plot KR-9 are 0.165 and 0.641, respectively, and the values for KR-10 are 0.445 and 0.779, respectively. Except for CV_{*h} of KR-9, which is about the same magnitude as from spatially variable K_s and K_o surfaces, all the other values of σ_* and CV_* are significantly greater than those computed from the spatially variable K_s and K_o. This indicates the dominant impact of hillslope microtopography on the variability of overland flow fields.

Clearly, the characteristics of sheet flow on natural hillslope surfaces can not be reproduced with a one-dimensional model. For the two plots simulated, considerable errors were generated even in the cross-slope average depth and velocity profiles when plane surfaces with mean slopes were used to represent the natural state.

4.5 Summary

A two-dimensional hydrodynamic and numeric model for overland flow (HyNuM) is used to simulate the influence of spatial variations of hillslope hydraulic and physical properties on the characteristics of overland flow,

Table 4.8 Peak and time to peak for hydrographs from two natural microtopographic surfaces (q_p^1, t_p^1) relative to those from uniform planes (q_p^o, t_p^o)

PLOT	tr > ts	tr = .75 ts	
	t_p^1/t_p^o	t_p^1/t_p^o	q_p^1/q_p^o
KR-9	1.48	1.0	.778
KR-10	1.16	1.0	1.080

Table 4.9 Computed mean cross-slope deviations in depth (σ_{*h}, CV_{*h}), velocity (σ_{*V}, CV_{*V}) and flow direction ($\sigma_{*\phi}$) from two natural microtopographic surfaces

CASE	σ_{*h} (cm)	CV_{*h}	σ_{*V} (cm/s)	CV_{*V}	$\sigma_{*\phi}$ (deg.)
KR-9	.0967	.1650	.641	.595	14.45
KR-10	.3360	.4450	1.11	.779	13.90

including flow fields and hydrographs. The three hillslope variables evaluated are steady state infiltration (K_s), surface roughness (K_o) and microtopography. The bias in calculating the characteristics of overland flow using the simple one-dimensional model, specifically, the KWE and with the assumed homogeneous planes in place of the spatial heterogeneous surface are discussed. The results are summarized below.

4.5.1 Effects on the characteristics of hydrographs

1. For random spatial variation in K_s and K_o, a hydrograph is only influenced by the distribution mean of K_s and K_o, not by the variations, represented by σ_{Ks} or σ_{Ko} when overland flow is produced over the entire surface. For these cases, hydrographs can be accurately predicted using a one-dimensional model, e.g., the KWE, using assumed homogeneous planes with the corresponding mean values of K_s and K_o.

2. By altering flow depth and velocity profiles along a slope, trending variation with or without the embedded randomness in K_s and K_o strongly influences a hydrograph, including its timing and peak discharge. If rainfall durations are longer than the times to steady state runoff of a hillslope, the effects of the trending variations in K_s and K_o on the equilibrium hydrographs are on the times to steady state runoff and hydrograph shapes in the rising

and falling limbs. In comparison with those from homogeneous planes with the constant values of K_s or K_o, the times to steady state runoff will be shortened for downslope increasing K_s or K_o, but delayed for downslope decreasing K_s or K_o.

The effects of the trending variations on non-equilibrium hydrographs also include the magnitudes of the peak discharges and the effects are more significant. Depending on the duration of rainfall, the characteristics of the resultant hydrographs can differ significantly. The effects on non-equilibrium hydrographs for an arbitrary duration, tr = 75% t_s^o, are simulated. For downslope decreasing variations, the times to hydrograph peaks are the same as those from the corresponding homogeneous planes but the peak discharges are higher than those computed from the corresponding homogeneous planes. The hydrograph peaks increase with the magnitudes of the gradient of variation, G. For downslope increasing variations, the times to hydrograph peaks are generally delayed and the magnitudes of the peak discharges may be lower or higher than those computed from the corresponding homogeneous planes. Higher hydrograph peaks occur for large G values.

For these cases, the hydrographs predicted by assuming homogeneous planes with mean values of K_s or K_o will have significant errors. The results also show that

where overland flow is produced from the entire surface on a hillslope the characteristics of hydrographs produced from surfaces of trending variations with embedded randomness in K_s or K_o are determined by the trending variation components.

3. Depending on its geometric configuration, microtopography may have differing effects on a hydrograph. The microtopography with the two-dimensional corrugated cosine-waves aligned in both downslope and across the slope have no effects on a hydrograph. For these cases, hydrographs can be accurately predicted using the KWE for equivalent representative homogeneous planes using the mean slopes. However, for surfaces with the geometric configurations favorable to convergence of flow, e.g., surfaces with the corrugations aligned only in the downslope direction, the characteristics of hydrographs will be significantly affected. Therefore, errors will be generated by using an assumed homogeneous plane.

On natural hillslopes, the variation patterns of microtopography and of hydrograph response are more complex. Hydrographs from different microtopographic surfaces but having identical spatial saturated hydraulic conductivities can be very different. Large errors in predicted hydrographs can be generated by using a representative homogeneous plane using the mean slopes in place of the actual microtopography.

4.5.2 Effects on the characteristics of flow fields

1. Spatial variability in K_s and K_o on hillslopes causes spatial variability in depth and velocity fields of overland flow. As the variation of K_s (σ_{Ks}) or K_o (σ_{Ko}) increases, the variability of depth and velocity fields increases.

2. The effect of microtopography on the variability of depth and velocity fields is stronger than that of spatially variable K_s or K_o. For given microtopographic wave length, λ, the variability of a flow field increases with the microtopographic amplitude, ϵ. With fixed ϵ, the variability of the flow field increases as the value of λ becomes smaller. In the latter instance the results are not definitive because of the smoothing errors introduced by the numerical resolution of the model.

3. Conditions that favor increasing flow depth and decreasing velocity, e.g., greater roughness or smaller slopes, reduce the variability of depth and velocity fields caused by spatial variability of K_s and K_o. One exception is for microtopography, where the variability of depth becomes larger for smaller slopes.

4. Decreasing excess rainfall rate reduces the variability of depth and velocity fields caused by spatial variability of K_o and microtopography. An exception is for

spatially variable K_s, where the variability of depth becomes larger for a smaller excess rainfall intensity.

In general, the simulation results show that on a spatially variable hillslope the cross-slope mean depth and velocity profiles along the downslope directions may be accurately computed by using the KWE and an assumed homogeneous plane. However, the spatial variability in the flow fields can not be predicted using the assumed homogeneous planes. The spatial variability in flow fields is important to soil erosion. Without incorporating the variability in flow fields when computing soil erosion, significant errors may result. This is illustrated in the next chapter.

Chapter Five

EFFECTS OF SPATIALLY VARIABLE SHEET FLOW ON SOIL EROSION

5.1 Introduction

Horton (1945) proposed a theory of sheet flow, sheetwash erosion, and rill formation to explain the interrelationships between hillslope geomorphology and overland flow. Where Horton overland flow is the dominant runoff process, a thin, irregular sheet of water flows down hillsides and imposes a shear stress on the soil surface. The boundary shear stress produced by the overland flow is the main force for the generation of soil erosion, and therefore is mostly responsible for sculpting hillslope morphology in arid and semi-arid regions. Accurate determination of the boundary shear stress is, therefore, necessary for understanding the processes of soil erosion and hillslope evolution, and is a necessary first step for any physically based soil erosion modeling.

The distribution of the boundary shear stress, τ, at any point on a hillslope is determined by the characteristics of overland flow at the point. The characteristics of overland flow, especially depth and velocity, are strongly influenced by the spatial variabilities of hillslope properties including surface roughness, infiltration, and microtopography. These spatial variations of hillslopes are sufficient to

redistribute runoff water within the flow field and concentrate the flow into topographically depressions. These altered flow fields in depth and velocity can significantly change the distribution of the boundary shear stress. For example, at places where flow concentrates the flow depth and velocity increase, the resulting boundary shear stress will be large. This will strongly influence the magnitude and spatial patterns of soil erosion.

The effect of spatially varied overland flow due to the spatial variation of hillslope properties on the boundary shear stress has not been adequately incorporated into soil erosion modeling. For the majority of the current physically based erosion models (e.g., Foster and Meyer, 1972; Foster, 1982; Simons et al., 1975; Morgan, 1980; Zhang, 1985) the boundary shear stress is computed based on the spatially averaged depth and velocity profiles of overland flow. Predictions of soil erosion and sediment transport rates by physically based erosion and transport models are extremely sensitive to local boundary shear stress (Dunne and Aubry, 1986; Zhang, 1986). Therefore, by ignoring the spatial variation of boundary shear stress, large errors may be generated by existing erosion models when significant spatial variation of overland flow occurs. Some implications of the variability

of flow fields on hillslope soil erosion are discussed below.

5.2 Implications for Modeling Soil Erosion

A simple erosion model based on a Du Boys-type equation is used for the analysis. The model has the following form:

$$q_s = \begin{cases} a\ (\ \tau - \tau_c\ )^b & \tau > \tau_c \\ 0 & \tau \le \tau_c \end{cases} \qquad (73)$$

where q_s is soil erosion rate, a is a parameter relating soil susceptibility to erosion, b is a constant, τ is the boundary shear stress due to sheet flow and τ_c is the critical boundary shear stress for initiation of soil erosion. τ and τ_c are often expressed as

$$\tau = \gamma\ h\ S_o \qquad (74)$$

$$\tau_c = \gamma\ h_c\ S_o \qquad (75)$$

where γ is the specific weight of water, h is the flow depths, h_c is the flow depth corresponding to τ_c, and S_o is the land surface local slope. Current erosion models often use cross-slope mean depth and spatially averaged slope of plots or even hillslopes in place of spatially variable depth and local slope for prediction of soil erosion. The question to be answered is: what is the prediction bias due to such a simplification?

For simplicity, the results from microtopographic surface, plot KR-10, are used for the present discussion. The results from this specific case should be relevant to the cases where there is a spatial variability in overland flow which may be caused by spatially variable infiltration or surface roughness.

5.2.1 Computational Bias in Predicting the Excess Shear Stress

Excess shear stress is defined as the part of shear stress which exceeds the critical shear stress and actually brings soil particles into motion. For a given hillslope, the critical boundary shear stress, τ_c, is determined by hillslope soil conditions. Depending on the nature of hillslope soils, the values of τ_c may vary from near zero for cohesionless soils to some large number for soils with strong cohesion. It is assumed that the critical shear stress, τ_c, on a hillslope remains spatially constant. Therefore, the effect of "armoring" on the critical shear stress is also ignored. The excess shear stress generated on the hillslope surface is thus assumed to vary only with the spatially variable overland flow. By assuming spatially uniform overland flow, significant errors in the distribution of the computed excess shear stress may result.

Depending the values of τ_c, and the excess rate of rainfall, the error in the computed excess shear stress fields will be different. Figure 5.1 shows some of the typical patterns of the excess shear stress fields computed for plot KR-10 and from the assumed equivalent homogeneous plane for critical shear stresses of 18, 14 and 8 dynes/cm^2 and an excess rainfall rate of 5cm/hr. On the variable microtopographic surface, there is a strong spatial variability in excess shear stress. These spatial distribution patterns of excess shear stress may result in non-uniform soil erosion and deposition over the plot. With the assumed homogeneous plane, the excess shear stress is uniform across the slope and increases monotonically downslope. This distribution pattern results in a uniform soil erosion at cross-slope sections. With the monotonically increasing excess shear stress downslope, there would be no deposition anywhere on the plot. This is inconsistent with field observations. Figure 5.1a also indicates that with spatially variable microtopography, the model predicts some patches of excess shear stress, thus, some soil erosion over the plot. However, the model predicts no excess shear stress on the assumed plane, and therefore no soil erosion occurring on the plot.

For given hillslope conditions, the bias in predicting the total area on which there is an excess

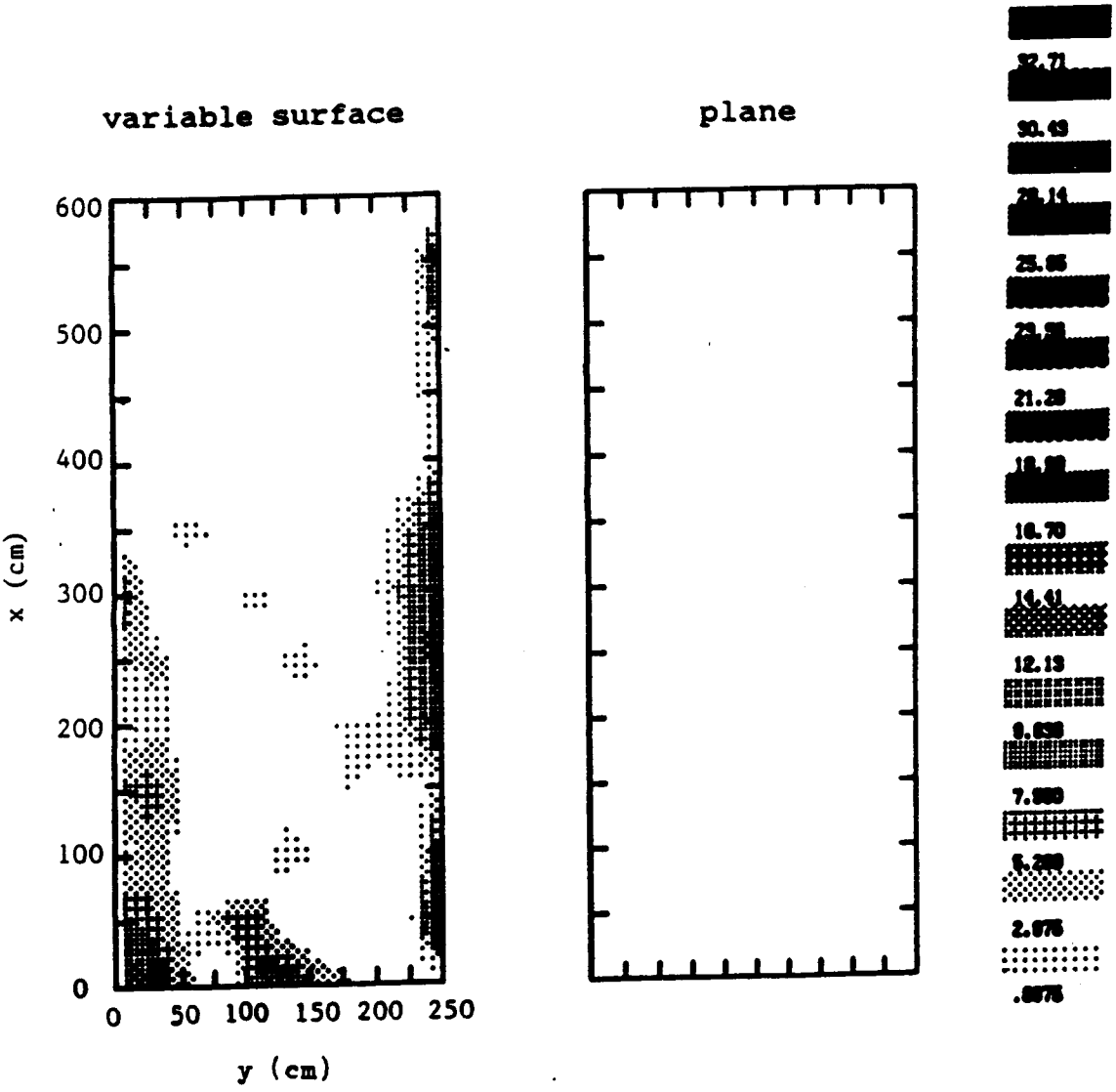

Figure 5.1 Excess shear stress fields simulated for the microtopography of plot KR-10 and the corresponding plane surface. (The gray scale represents excess shear stress in dynes/cm^2). a) V_o = 5 cm/hr; τ_c = 18 dynes/cm^2

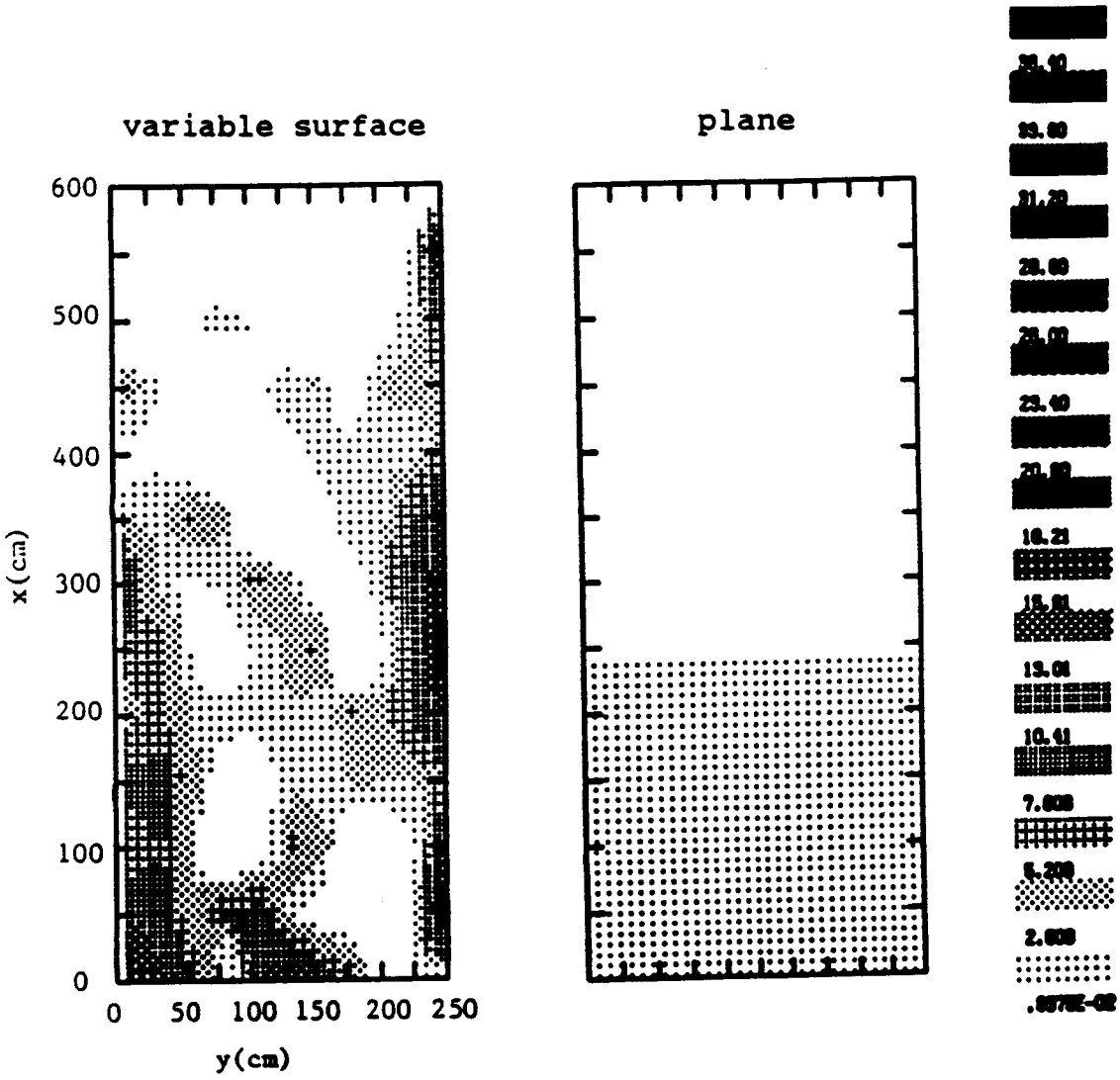

Figure 5.1 continued.
b) V_o = 5 cm/hr; τ_c = 14 dynes/cm^2

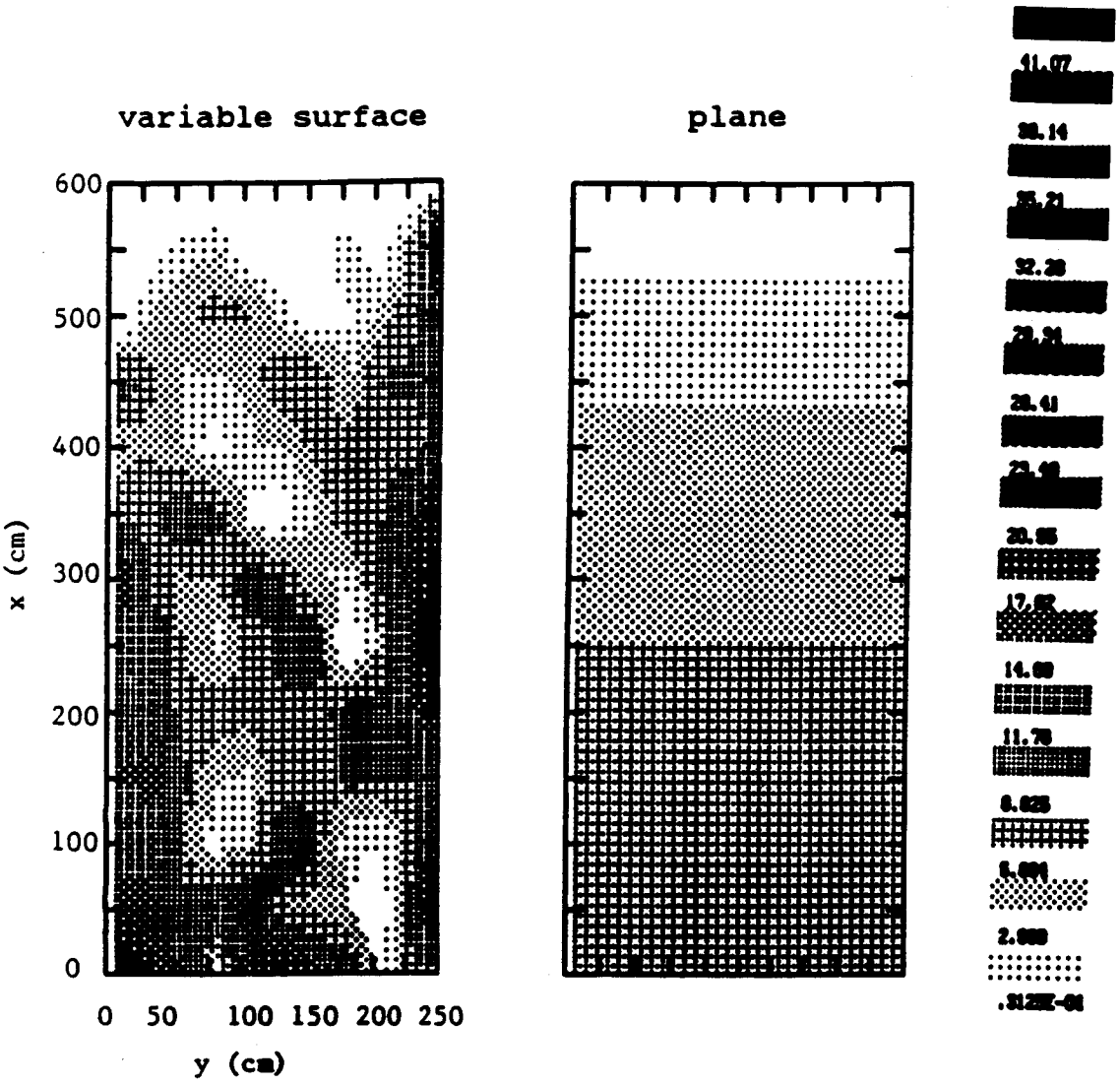

Figure 5.1 continued.
c) V_o = 5 cm/hr; τ_c = 8 dynes/cm^2

shear stress due to using a homogeneous plane is strongly affected by the critical shear stress, τ_c, and rainfall intensity. To examine the impact of τ_c, an excess rainfall rate of 5cm/hr is chosen and the total area of excess shear stress, A_c, within the plot is computed for different values of τ_c. The values of τ_c for cohesionless sediment materials have been summarized by Smith (1984), and the values ranges from 6 dynes/cm^2 for 0.1 mm diameter sediment to about 40 dynes/cm^2 for 4 mm diameter sediment. For this simulation, the values of τ_c have been assumed to vary from 6 dynes/cm^2 to 40 dynes/cm^2. The results of the simulation are shown in Figure 5.2. In Figure 5.2, A_t is the total area of plot KR-10 and A_c is the total area of excess shear stress. The results indicate that the area of excess shear stress from both the microtopography and the assumed homogeneous plane decrease as the value of τ_c increases. For τ_c < 10 dynes/cm^2, the values of A_c computed from the homogeneous plane are slightly (<10%) greater than those from the variable surface. For τ_c > 10 dynes/cm^2, as the value of τ_c increases, the value of A_c from the homogeneous plane reduces much faster than that from the variable microtopographic surface. As the value of τ_c increases over 18 dynes/cm^2, A_c for the homogeneous plane reduces to zero, while A_c for variable surface is still 32% of A_t for τ_c = 18 dynes/cm^2, and 2.1% of A_t even for τ_c = 40 dynes/cm^2. The results indicate that

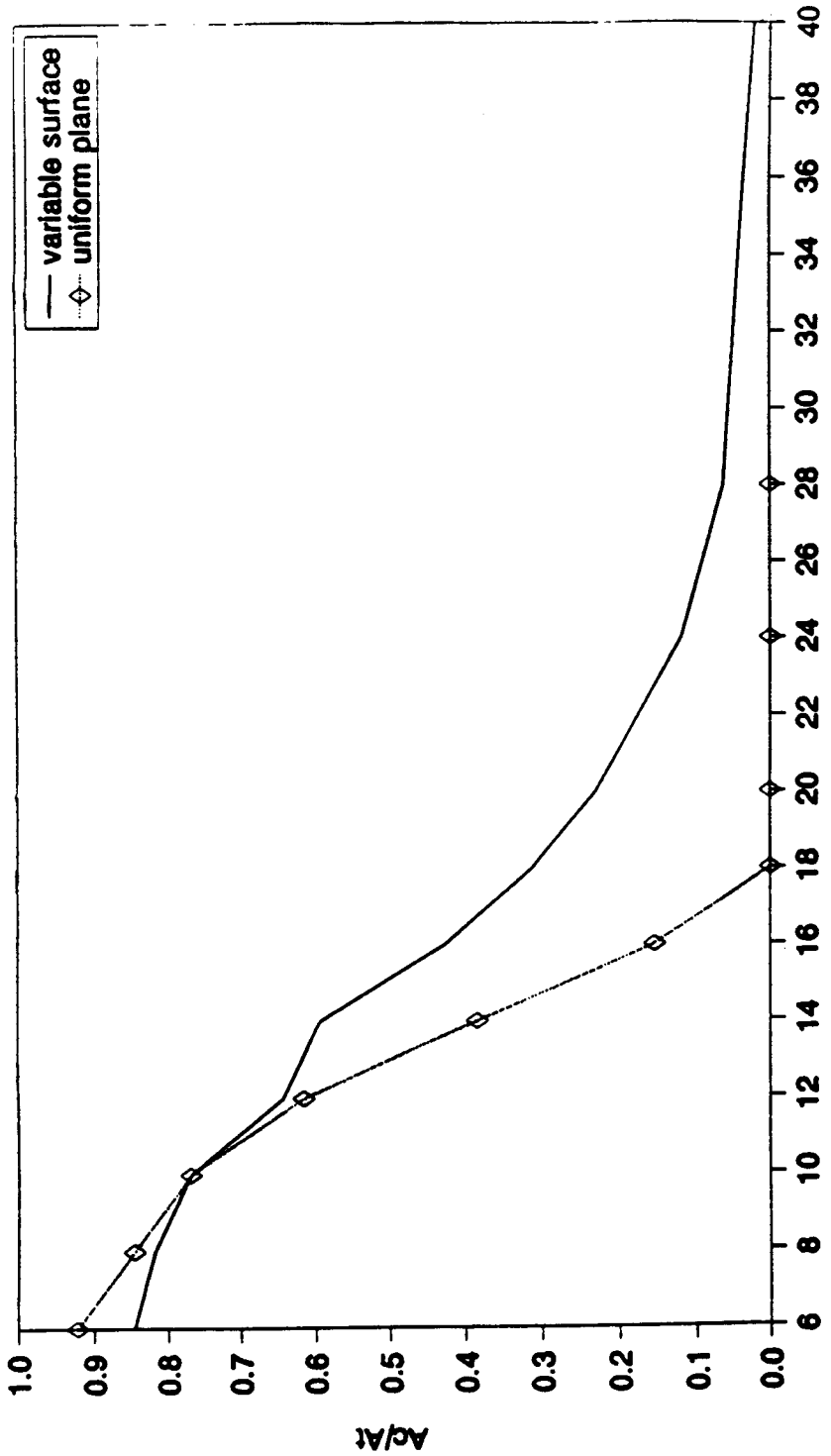

Figure 5.2 Bias in predicting total area of excess shear stress on plot KR-10 by assuming a uniform plane for various critical boundary shear stresses under an excess rainfall rate of 5cm/hr.

approximating a microtopographic surface with a homogeneous plane can result in a slight overestimation of the total area of excess shear stress for small values of τ_c, e.g., fine-textured, cohesionless soils, but a severe underestimation of the total area of excess shear stress for large τ_c.

To examine the impact of rainfall on these relations, a critical shear stress of 15 dynes/cm^2 was chosen and A_c was computed for various values of excess rainfall rate. The results are shown in Figure 5.3. For small excess rainfall rate, e.g., Vo < 9 cm/hr, A_c computed from the homogeneous plane is smaller than that from the variable surface. For an excess rainfall rate less than 4 cm/hr, A_c computed from the homogeneous plane reduces to zero, while A_c computed from the variable surface is 30% of the total plot area. Even for an excess rainfall rate of 2cm/hr, A_c computed from the variable surface is still 3% of the total plot area. As the excess rate of rainfall increases over 9 cm/hr, A_c computed from the homogeneous plane becomes larger than that from the variable surface. Therefore, using an homogeneous surface in place of the real microtopography can result in significant errors in the computed total area of excess shear stress. For the homogeneous plane, the total area of excess shear stress was underestimated for storms with V_o < 9 cm/hr, but was overestimated for extremely large storms.

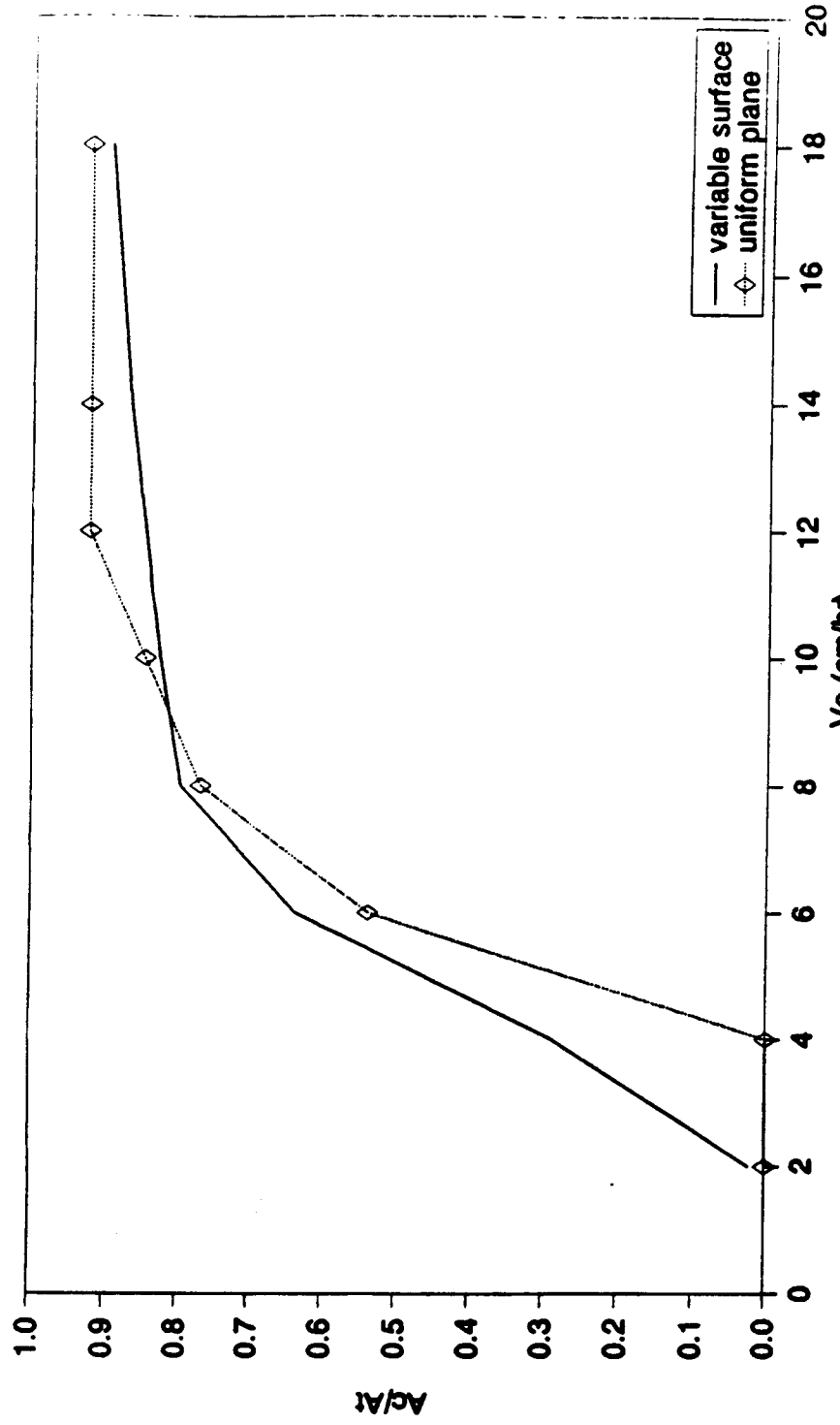

Figure 5.3 Bias in predicting total area of excess shear stress on plot KR-10 by assuming a uniform plane for various excess rainfall rates under a given critical boundary shear stress of 15 dynes/cm^2.

5.2.2 Computational Bias in Predicting Sediment Transport Rate

For a given hillslope, the soil erosion rate depends not only on the total area of the excess shear stress, but also the magnitude of the excess shear stress distributed on the area. The simulations in this section are only for soil erosion or detachment at local cross-slope sections and under steady flow conditions; the mechanisms of sediment transport and deposition are not considered.

The total sediment transport rate at a given cross-slope section along a hillslope can be computed either using a uniform cross-slope depth from a homogeneous plane surface as

$$Q_s' = B\ a\ (\tau - \tau_c)^b \qquad (76)$$

or using variable cross-slope depth and local slope at the cross-slope section as

$$Q_s = \int_0^B a\ (\tau - \tau_c)^b\ dy \qquad (77)$$

where Q_s' and Q_s are the computed total sediment transport rates at the cross-slope section using the mean depth and slope and variable depth and slope gradient, respectively, and B is the length of the cross-slope section.

The prediction bias resulting from using uniform depth and mean slope in place of the variable depth and local slope is expressed by the ratio of Q_s'/Q_s, i.e.,

$$\text{Bias} = \frac{Q_s'}{Q_s} \tag{78}$$

By substituting equation (74) for τ, and replacing the integral in equation (77) with finite summation of the values at the regularly discretized grid points, equation (78) takes the following form:

$$\text{Bias} = \frac{1}{\frac{1}{n}\Sigma\left[\frac{h_i S_i - \tau_c}{\bar{h}\,\bar{S} - \tau_c}\right]^b} \tag{79}$$

where n is the number of grid points at the cross-slope section, and h_i and S_i are the flow depth and slope at each grid point, respectively. Since the bias defined in equation (79) is independent of the soil susceptibility parameter a, the effect of this parameter will not be discussed. The values of exponent b have been given in several studies and typically ranged from 1 to 3 (Foster et al., 1977; Kilinc and Richardson (1973); Abrahams et al., 1988).

For examining the influence of critical shear stress and excess rainfall, an erosion susceptibility b = 2 was used. Figure 5.4 shows the bias in computed total sediment

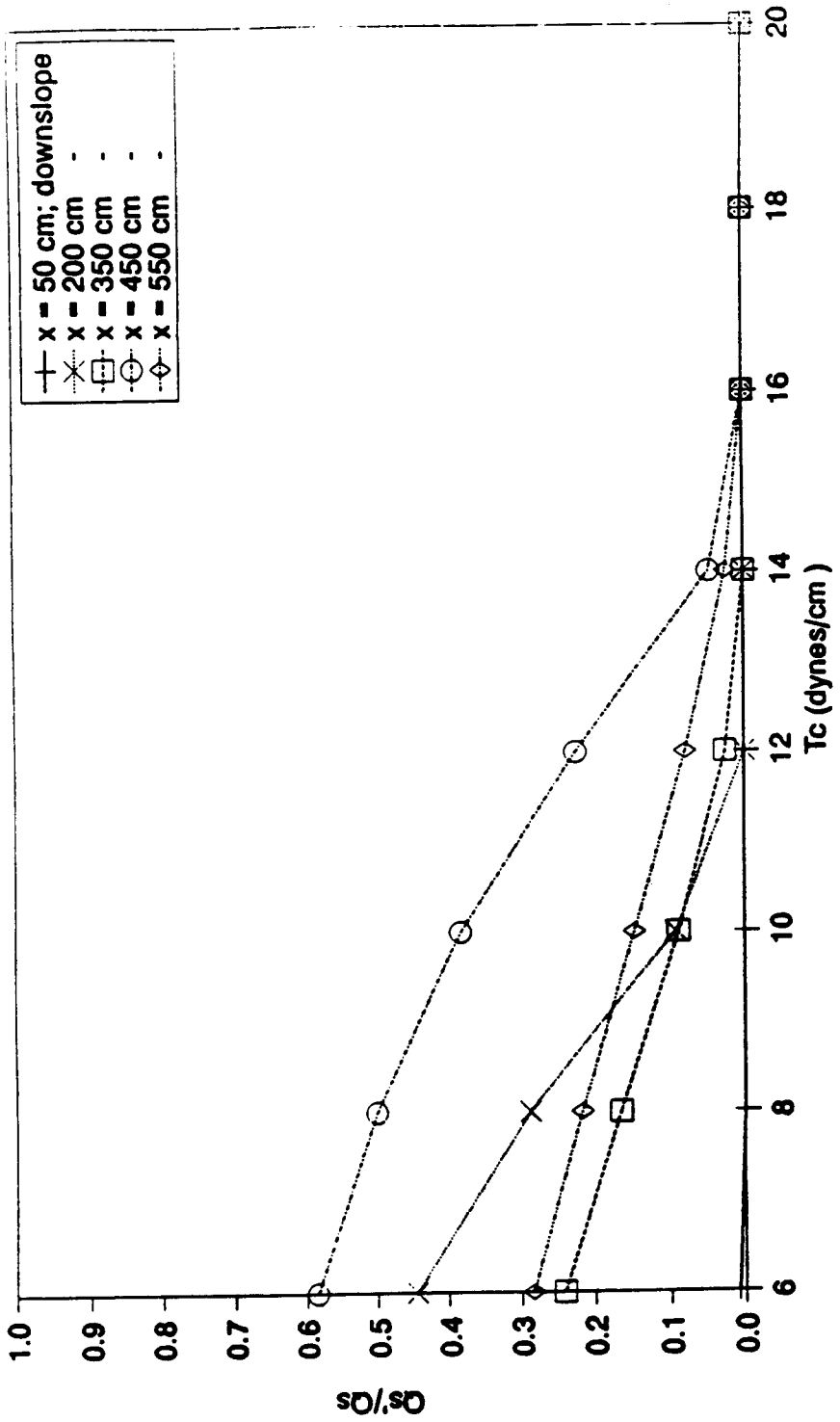

Figure 5.4 Bias in predicting total sediment transport rate at cross-slope sections on plot KR-10 by assuming a uniform plane for various critical boundary shear stresses under an excess rainfall of 5cm/hr.

transport rates at various cross-slope sections along plot KR-10 for an excess rainfall rate of 5 cm/hr and for different values of τ_c. The results reveal a severe underestimation in sediment transport rate by assuming an homogeneous plane for all values of τ_c and at all cross-slope sections, although the bias at different cross-slope sections are different. Even the best one at x = 450 cm and with τ_c = 6 dynes/cm^2 is still only 58% of the total sediment transport rate from the microtopographic surface. For small values of τ_c, the bias is relatively small, and as the values of τ_c increase, the bias becomes very large. For the values of τ_c greater than 16 dynes/cm^2, no cross-slope sections on the assumed homogeneous plane experience soil erosion. However, as indicated in Figure 5.2, at τ_c = 16 dynes/cm^2, there is still about 45% of the plot area where the boundary shear stress exceeds the critical shear stress, and therefore, where sediment transport continues.

The influence of the rate of excess rainfall on the bias of computed total sediment transport at cross-slope sections is illustrated in Figure 5.5. This result was generated with τ_c = 15 dynes/cm^2 and for various values of the excess rainfall rate. Again, the results reveal a severe underestimation of total sediment transport rate at all cross-slope sections for all excess rainfall rates, although as the excess rate of rainfall increases the prediction bias becomes smaller.

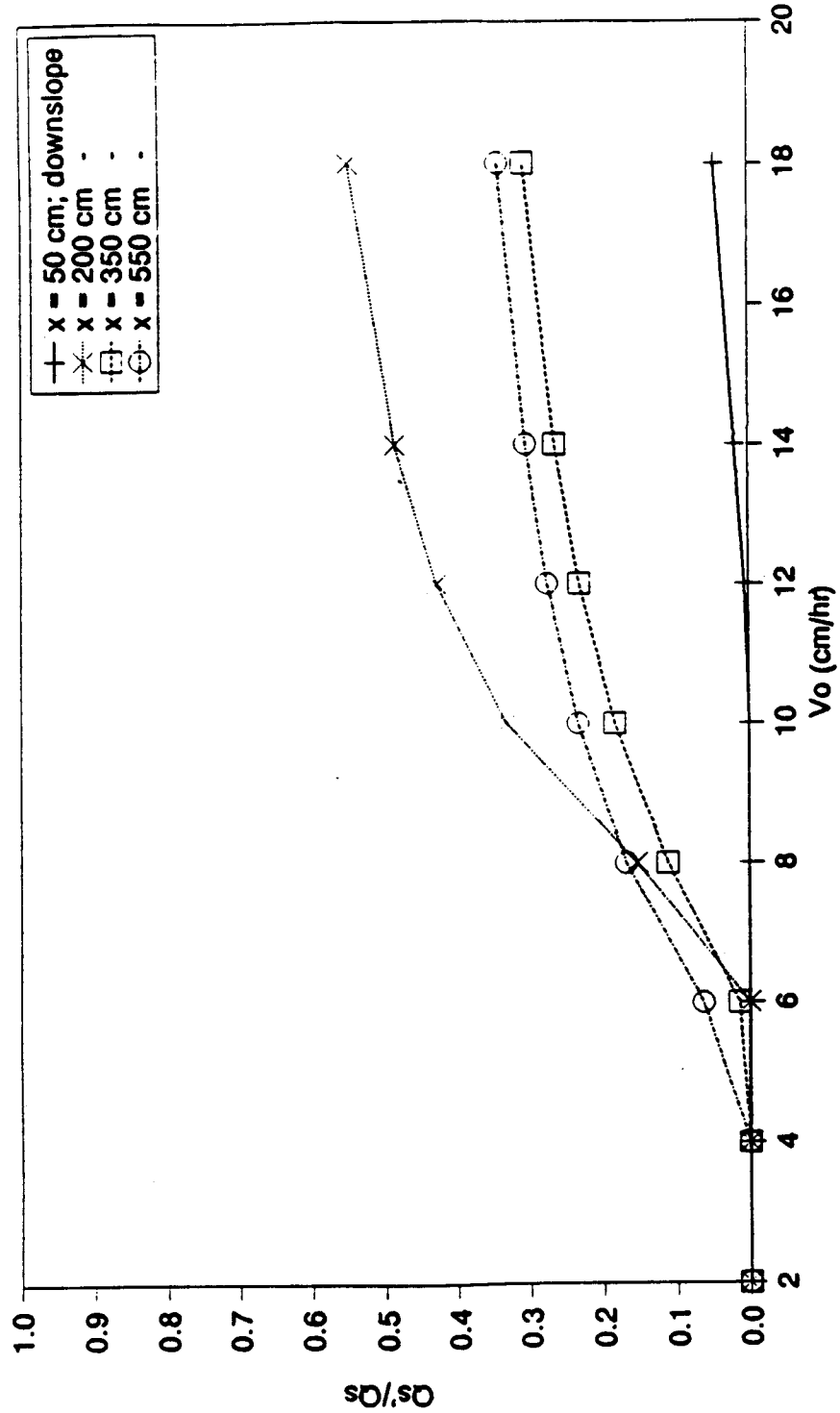

Figure 5.5 Bias in predicting total sediment transport rate at cross-slope sections on plot KR-10 by assuming a uniform plane for various excess rainfall rates under a given critical boundary shear stress of 15 dynes/cm^2.

The effect of parameter b on the prediction bias due to the assumption of an homogeneous plane was investigated over a range of 1 to 3. In the simulation, the excess rainfall rate and the critical shear stress were assigned the values of 8 cm/hr and 15 dynes/cm^2, respectively. The results of prediction bias at each cross-slope sections along the plot are shown in Figure 5.6. The results again show severe underestimations by using an homogeneous plane. The magnitudes of the underestimation greatly increase with parameter b. It is observed that the prediction bias generally decreases in the downslope direction. This presumably results from the increase of flow depth, and thus the reduced spatial variability in the flow.

5.3 Summary

The effects of spatial variability of overland flow due to spatial variations of hillslope characteristics on soil erosion have been examined. The analysis concentrated on two aspects that are of interest to modeling hillslope soil erosion: (1) the total area of excess shear stress, A_c, and its distribution on a spatially variable hillslope; and (2) sediment transport rate, Q_s, at cross-slope sections along the hillslope surface. The biases in predicting A_c and Q_s using an idealized homogeneous plane for a spatially variable hillslope surface are discussed.

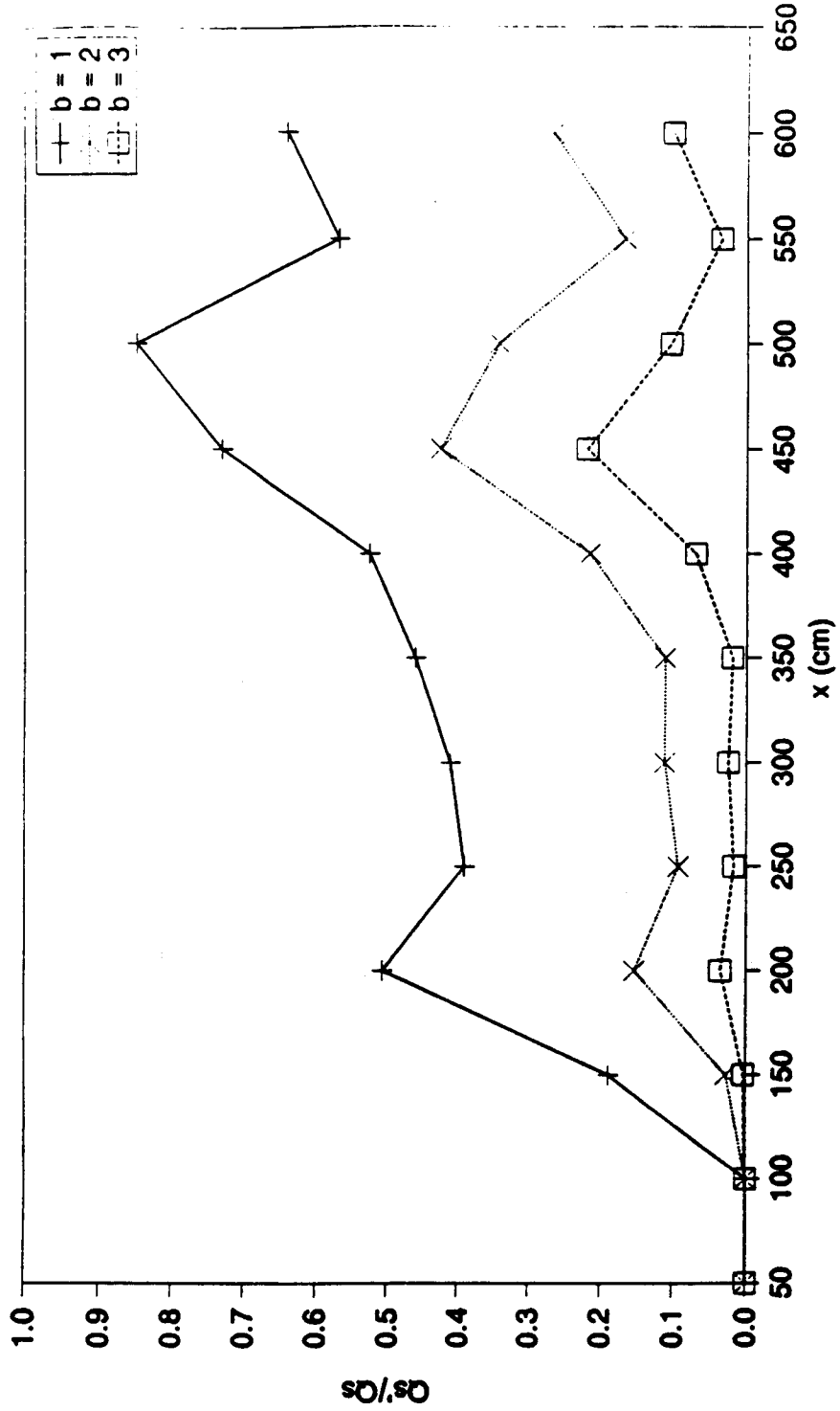

Figure 5.6 Bias in predicting total sediment transport rate at cross-slope sections on plot KR-10 by assuming a uniform plane for various values of exponent b.

The results from the model simulations are summarized below.

1. Variable flow fields produce spatially variable excess shear stress fields, which result in non-uniform soil erosion and deposition patterns on a hillslope surface. These patterns in excess shear stress, and, therefore, hillslope sediment transport and deposition can not be predicted with an assumed homogeneous plane.

2. Approximating a spatially variable hillslope with a representative homogeneous plane results in a slight overestimation of A_c for small τ_c, i.e., for fine-textured, cohesionless soils, but a severe underestimation of A_c for or coarse-textured or cohesive soils with large τ_c.

3. Using an homogeneous plane to represent a spatially variable hillslope results in an underestimation of A_c under excess rainfall intensities $\leq$ 9cm/hr, but an overestimation in A_c under rainfalls of extremely large intensities.

4. Sediment transport rates can be severely underestimated at cross-slope sections along a hillslope for different values of τ_c and under different rainfall intensities, if a spatially variable hillslope is approximated by an homogeneous plane. As the critical shear stress increases and the excess rainfall rate

decreases, the amount of underestimation in sediment transport increases.

5. The amount of underestimation in sediment transport due to using an homogeneous plane also increases with the exponent parameter b, if one uses a Du-Boys type equation for prediction of sediment transport.

6. From the results of the simulation and analysis, it is concluded that sheet flow with strong cross-slope variations generally results in more soil erosion than that with no cross-slope variations.

Chapter Six

CONCLUSIONS AND RECOMMENDATIONS

Spatial variations in hillslope properties strongly influence the characteristics of overland flow, and therefore hillslope soil erosion and pollutant transport. The objectives of the study have been: 1) to develop a physically-based overland flow model that can predict and simulate overland flow, including flow fields and hydrographs, under spatially-variable hillslope conditions; and 2) to use the model to examine the effects of spatial variations of hillslope properties on the characteristics of overland flow and on hillslope soil erosion. Conclusions and recommandations for future work follow.

6.1 Conclusions

A two-dimensional hydrodynamic and numerical model for overland flow has been developed. The model can explicitly incorporate hillslope variations in steady infiltration, surface roughness, and microtopography. The accuracy of the model has been tested by comparing the model results with those computed with characteristic-based methods for spatially uniform surfaces and with experimental data for surfaces with spatially-variable gradients. The results of these tests indicated that the numerical solution of the model is accurate and has good

stability and convergence properties. With the model, the effects of spatially-variable hillslope properties on the characteristics of overland flow, including flow fields, can be simulated and examined on a realistic basis. Some limitations of the model have also been pointed out. An important limitation is that the model requires the simulation domain to be inundated.

The second objective was carried out in chapters four and five. First, the model simulations of overland flow were performed on spatially-variable hillslope surfaces. Then, based on simulation results, the effects of spatially-variable steady infiltration, surface roughness and microtopography on the characteristics of overland flow and on soil erosion were analyzed.

With respect to hydrographs, the simulation results suggest that the spatial trending variation in steady infiltration and surface roughness has a strong influence on hydrographs. Depending on variation patterns, e.g., downslope-increasing or downslope-decreasing, trending variation in infiltration and surface roughness may have differing effects on a hydrograph. The effect of downslope-increasing variation in infiltration or surface roughness is to shorten the hillslope concentration time or time to equilibrium runoff. The effect of downslope-decreasing variation in infiltration

or surface roughness is the opposite. The effects of the two trending variations on hydrographs become more pronounced as the magnitude of the gradient of variation increases. Smith and Hebbert (1979) arrived at similar conclusions.

For the case of random variations in infiltration and surface roughness, the characteristics of hydrographs are influenced by the distribution means of the variables only, and the standard deviations of the distributions have no impacts on the hydrographs.

Therefore, for hydrograph predictions on hillslopes, it is necessary to take into account hillslope trending variations and hillslope random variations may be ignored. With these simplifications, a simple one-dimensional model, e.g., the KWE or a KWE-based cascade model, may be used for hillslope hydrograph predictions. Noting the assumptions of steady infiltration and the absence of spatial correlations in the distributions of steady infiltration and surface roughness during model simulations, the conclusion with regard to random variations may not be true for cases where there exist significant unsteady infiltration and strong spatial correlations in infiltration and surface roughness.

The effects of microtopography on the characteristics of hydrographs have been examined for both hypothetical and real microtopographic surfaces. The hypothetical

microtopography is represented by a surface with cosine-wave corrugations aligned in one or two directions on a plane. While the microtopography with the corrugations aligned in both the downslope and cross-slope directions has no influence on the characteristics of hydrographs, the microtopography with the corrugations aligned only in the downslope direction and the real microtopographic surfaces have strong influences on hydrographs. Depending on its geometric configurations, microtopography may have differing effects on a hydrograph. If the geometric configuration favors the convergence of the flow, the effect of the microtopography is to reduce the apparent flow resistance of the surface, and shorten hillslope concentration time.

The corrugated microtopography and the two real microtopography ed here may be but a few of many microtopographic patterns of natural hillslopes. To generalize the effects of microtopography on overland flow hydrographs, quantitative descriptions and abstractions of realistic microtopographic patterns for different geomorphologic regions will be necessary.

With regard to overland flow fields, the model simulations indicate that spatial variations of infiltration, surface roughness, and microtopography all have strong influences on the depth and velocity fields of

overland flow, and that the influence of microtopography is strongest.

For given hillslopes, the spatial variability of the depth and velocity fields due to these spatial variations generally decreases with an increase of flow depth and a decrease of flow velocity, and thus with an increase of surface roughness and a decrease of slope. Exceptions exist for individual cases. The simulation results show that while the profiles of the mean depth and velocity computed from spatially-variable hillslopes may be well approximated by using idealized homogeneous planes with mean values of the hillslope variables, the significant spatial variability of the depth and velocity can not be predicted and simulated using idealized homogeneous planes.

Accurate characterization of overland flow fields has been shown (chapter five) to be important for prediction of hillslope sediment transport by overland flow. When predicting soil erosion from spatially-variable hillslope surfaces, significant errors may result by using an idealized homogeneous plane. These errors may include: 1) the production of unrealistic erosion and deposition patterns; 2) the underestimation (most likely) or overestimation (rarely) of the total surface area on which the boundary shear stress generated by overland flow exceeds the critical shear stress; and 3) the severe

underestimation of sediment transport rates at cross-slope sections along the hillslopes. It is, therefore, necessary to take into account spatial variations in hillslope physical characteristics when predicting and simulating hillslope soil erosion and sediment transport.

The study of the effects of spatial variations in hillslope physical characteristics on overland flow and soil erosion suggest that the uncertainties in model parameters and thus model predictions can be significantly reduced if the spatial variations in hillslope properties are incorporated into the model simulation.

6.2 Recommendations

This study has contributed to our understanding of the processes of overland flow on spatially-variable hillslopes. It is the first time that the effects of spatial variations in infiltration, roughness and microtopography on the characteristics of overland flow have been simulated using a two-dimensional overland flow model. The roles and relative importances of individual hillslope spatial variables have been identified, but their interaction has not been simulated. The results of the study are useful for understanding the processes of overland flow and hydrologic predictions on natural hillslopes.

Further study is needed in three areas: 1) to improve the model so that the restriction of complete inundation required by the model may be relaxed; 2) to simulate the response of overland flow for more realistic spatial variations of natural hillslopes so that the characteristics of overland flow on natural hillslopes can be generalized and incorporated into routine hydrologic predictions; and 3) to develop a modeling approach so that the model or the information about the characteristics of overland flow obtained from the model simulation at small scales can be incorporated into hydrologic predictions of scales of practical interest. Detailed discussions of these three areas follow.

1. Recommendations on model improvements

Further improvement of the model should emphasize the elimination or relaxation of the model restriction of complete inundation of hillslope surfaces.

The restriction on microtopography may be eliminated with an ad hoc approach. With this approach, microtopographic heights are viewed as individual islands defined with fixed boundaries. The highs of these islands can be different depending on the distribution of the microtopographic highs, and therefore, they may be inundated or exposed at different times during transient an overland flow. Although it only approximates reality,

this modification would greatly enhance the utility of the model for the cases where hillslope surfaces may be partially inundated.

To eliminate the restriction on infiltration will be difficult, if not impossible, because of the free boundaries created by runoff and runon. Further research and modeling efforts are needed to deal with the free boundary problems.

2. Recommendations on further analysis of the effects of spatially-Variable hillslopes on overland flow

Future model simulations and analysis should focus on more realistic spatial variations of hillslope properties. Microtopographic patterns of natural hillslopes should be studied and quantitatively generalized within different geomorphologic regions. Only with the generalized, yet, realistic microtopography, can the effects of microtopography of natural hillslopes be simulated and analyzed. These effects can then be incorporated in routine predictions of overland flow and soil erosion on natural hillslopes.

Future study should also address the combined effects of spatial variations in infiltration, surface roughness and microtopography. Field observations (Dunne et al., 1987) indicated that there is a strong positive correlation between infiltration capacity, surface

roughness and microtopography due to vegetation. The preliminary analysis of the data suggest that this positive correlations in infiltration, surface roughness, and microtopography would cause more spatial variability in overland flow fields and have additional effects on hydrographs. It is important to examine these effects in a realistic two-dimensional framework.

3. Recommendations on the application of the model for hillslope scales of practical interest

Numerical solutions by finite-difference models have some inherently unstable features. As the number of the computational grids increases beyond a certain limit, the round-off errors will accumulate much faster, causing instability in the numerical solutions. For overland flow cases, the lack of control at the downslope boundary will also give rise to numerical instability at and near the boundary. This instability at and near the downslope boundary grows as the number of grid nodes increases. Therefore, there is a trade-off between large spatial scales to be modeled and small hillslope features to be resolved when using the model for prediction of hillslope overland flow.

This work has been concerned with small portions of a hillslope. For hydrologic predictions for an entire hillslope, to maintain a stable solution, the model

computation is required to use a large spatial step or grid size. As a result, the grid size used may be so large, in comparison with the spatial scales of hillslope variabilities, that some important effects of the hillslope spatial variabilities may be left out during model computations. To resolve the hillslope spatial variabilities that are important to overland flow and soil erosion, it is necessary to use spatial steps that are smaller than the spatial scales of the hillslope variabilities during model computations. This may result in a strong instability in the numerical solution. Therefore, appropriate modeling strategies must be developed to solve this spatial problem.

The model simulations and analysis described in this study are admittedly at a smaller scale than is of practical interest to the predictions in overland flow and soil erosion on natural hillslopes. The response of overland flow to the spatial variabilities of hillslopes of small scales, once understood, might be parameterized at sub-grid scales, and then incorporated into large grid scales during large scale predictions. This is one possible approach for addressing the scale problems.

REFERENCES:

Abrahams, A. D., A. J. Parsons and S-H Luk, Resistance to Overland Flow on Desert Hillslopes. J. of Hydrol. 88, 343-363, 1986.

Abrahams, A. D., A. J. Parsons and S-H Luk, Hydrologic and Sediment Responses to Simulated Rainfall on Desert Hillslopes in Southern Arizona. Catena 15, pp 103-117, 1988.

Achouri, M. and G. F. Gifford, Spatial and Seasonal Variability of Field Measured Infiltration Rates on A Rangeland Site in Utah. J. of Range Management, 37(5), pp.451-455, 1984.

Anderson, D.A., J.C. Tannehill, R. H. Pletcher, Computational Fluid Mechanics and Heat Transfer, McGraw-Hill, New York, 1984.

Akan, A.O. and B.C. Yen, Mathematical Modeling of Shallow Water Flow over Porous Media. J. of Hydraul. Div. ASCE, 107(HY4), pp.479-494, 1981.

Aubry, B.F., Runoff, Sediment Transport, and Rill Formation by Sheet Flow, M.S. Thesis Submitted to the University of Washington, Seattle, WA., 1984.

Babalola, O., Spatial Variability of Soil Water Properties in Tropical Soils of Nigeria, Soil sci. 21(2), pp.269-279, 1978.

Borah, D.K., S.N. Prasad and C.V. Alonso, Kinematic Wave Routing Incorporating Shock Fitting, Water Resour. Res. 16(3), pp. 529-541, 1980.

Brutsaert, W., De Saint-Venant Equations Experimentally Verified, J. Hydraul. Div. ASCE, 97(HY9), pp. 1387-1401, 1971.

Chen, C., Urban Storm Runoff Inlet Hydrograph Study, Vol. 2, Laboratory Studies of the Resistance Coefficient for Sheet Flow over Natural Turf Surface. Final Report No. PRWA106-2, Utah Water Research Laboratory, College of Engineering, Utah State Univ., Logan, Utah, p.56, 1975.

Chow, V.T. and A. Ben-Zvi, Hydrodynamic Modeling of Two-Dimensional Water Flow, J. Hydraul. Div. ASCE, 99(HY11), pp.2023-2040, 1973.

Codova, J.R., I. Rodriguez-Iturbe and P. Vaca, On the Development of Drainage Networks. In Recent Developments in the Explanation and Prediction of Erosion and Sediment Yield, Proc. of the Exeter Symp., IAHS Publ. no. 137, pp. 239-249, 1982.

Constantinides, C.A. and D. Stephenson, Two-Dimensional Kinematic Overland Flow Modeling. In Urban Stormwater Hydraulics and Hydrology, Proc. of 2nd Intl. Conf. on Urban Storm Drainage, Edit by B-C Yen. pp.49-58, 1981.

Cundy, T. W., An Analysis of the Effects of Spatial Variability of Point Infiltration Rates on the Comparison of Small and Large Plot Rainfall-Runoff. Ph.D Dissertation, Utah State University, 1982.

Cundy, T. W. and S. W. Tendo, Solution to the Kinematic Wave Approach to Overland Flow Routing with Rainfall Excess Given by Philip's Equation. Water Resour. Res., 21(8), pp.1132-1140, 1985.

Dronkers, J.J. Tidal Computations in River and Coastal Waters, North-Holland Publ. Amsterdam, pp.142-149, 1964.

Duffy, C., P. J. Wierenga and R. A. Kselik, Variations in Infiltration Rate Based on Soil Survey Information and Field Measurements. Ag. Exp. Sta. Bull. No. 600, New Mex. State Univ., p.40, 1981.

Dunne, T., The Relation of Field Studies and Modeling in the Prediction of Storm Runoff. J. of Hydrology, 65, pp.25-48, 1983.

Dunne, T. and B. F. Aubry, Evaluation of Horton's Theory of Sheetwash and Rill Erosion on the Basis of Field Experiments. In Hillslope Processes, A. D. Abrahams (ed), Allen & Unwin, Boston, 31-53, 1986.

Dunne, T. and R. D. Black, An Experimental Investigation of Runoff Production in Permeable Soils. Water Resour. Res., 6, pp.478-490, 1970a.

Dunne, T. and R. D. Black, Partial Area Contributions to Storm Runoff in A Small New England Watershed. Water Resour. Res., 6, pp. 1296-1311, 1970b.

Dunne, T and W.E. Dietrich, Experimental Investigation of Horton Overland Flow on Tropical Hillslopes: 2) Hydraulic Characteristics and Hillslope Hydrographs,

Zeitschrift fur Geomorphologie Supplemental Band 35, pp. 60-80, 1980.

Dunne, T. and L. B. Leopold, Water in Environmental Planning. W. H. Freeman Co., San Francisco, p.818, 1978.

Dunne, T., W-H, Zhang, T. C. Cundy, Systematic Variations in Infiltration on Semi-Arid Hillslopes. IGU-IAHS Workshop on Erosion, Transport, and Deposition Processes, Jerusalem, Israel, 1987.

Emmett, W. W., The Hydraulics of Overland Flow on Hillslopes, USGS Prof. Paper 662-A, P46, 1970.

Foster, G. R., Modeling the Erosion Process. In Hydrologic Modeling of Small Watersheds, Amer. Soc. Agri. Engi. Monograph No. 5, pp.297-380, 1982.

Foster, G. R. and L. D. Meyer, Transport of Soil Particles by Shallow Flow. Trans. of ASAE, 15(1), pp. 99-102, 1972.

Foster, G. R., L. D. Meyer and C. A. Onstad, An Erosion Equation Derived from Basic Erosion Principles. Trans. ASAE, 20: pp 678-682, 1977.

Freeze, R. A., A Stochastic-Conceptual Analysis of Rainfall-Runoff Processes on A Hillslope. Water Resour. Res., 16(2), pp.391-408, 1980.

Freeze, R. A. and J. A. Cherry, Groundwater. Prentice-Hall, Inc., Englewood Cliffs, H.J., p.604, 1979.

Govindaraju, R. S., S. E. Jones, and M. L. Kavvas, On the Diffusion Wave Model for Overland Flow: 1. Solution for Steep Slopes. Water Resour. Res., 24(5), pp.734-744, 1988.

Grah, O. J., R. H. Hawkins, T. W. Cundy, Distribution of Infiltration on A Small Watershed. Adv. Irrig. Drain., pp 44-54. 1983

Green, W. H. and G. Ampt, Studies of Soil Physics, Part 1: the Flow of Air and Water through Soils. J. of Agricultural Sciences, 4, pp.1-24, 1911.

Henderson, F.M., Open Channel Flow, pp.27-29, Macmillan, N.Y., 1966.

Henderson, F. M. and R. A. Wooding, Overland Flow and Groundwater Flow from A Steady Rainfall of Finite Duration, J. of Geophys. Res., 69(8), pp.1531-1540, 1964.

Horton, R. E., The Role of Infiltration in the Hydrological Cycle. Trans. Amer. Geophys. Union, 14, pp.446-460, 1933.

Horton, R. E., Erosion Development of Streams and Their Drainage Basins: Hydrophysical Approach to Quantitative Morphology. Bull. of Geol. Soc. of Amer., 56, pp. 275-370, 1945.

Horton, R. E. H. R. Leach and R. V. Vliet, Laminar Sheet Flow. Trans. Amer. Geophys. Union, 15, 1934.

Hromadka II, T.V., R.H. McCuen and C.C. Yen, Comparison of Overland Flow Hydrograph Models, ASCE J. Hydraul. Engr., 113(HY11), pp. 1422-1440, 1987.

Iwagaki, Y., Fundamental Studies on Runoff Analysis by Characteristics, Bull. 10, pp.1-25, Disaster Prev. Res. Inst., Kyoto Univ., Kyoto, Japan, 1955.

Izzard, C. F., The Surface Profile of Overland Flow. Eos Amer. Geophys. Union Trans., 25, pp.959-968, 1944.

Katapodes, N. and T. Strelkoff, Two-Dimensional Shallow Water-Wave Model, J. Engin. Mech. Div., ASCE, 105(EM2), pp.317-334, 1979.

Kawahara, M. and T. Yokoyama, Finite Element Method for Direct Runoff Flow, J. Hydraul. Div. ASCE, 106(HY4), pp.519-534, 1980.

Kibler, D.F. and D.A. Woolhiser, The Kinematic Cascade as A Hydrologic Model, Hydrol. Paper 39, Colo. State Univ., Fort Collins, 1970.

Kilinc, M. and E. V. Richardson, Mechanics of Soil Erosion from Overland Flow Generated by Simulated Rainfall. Hydrology Papers, Colorado State University, Fort Collina, No. 63, 1973.

Kisisel, I. T., R. A. Rao and J. W. Delleur, Turbulent Characteristics of Overland Flow - The Effects of Rainfall and Boundary Roughness. Technical Report No. 28, Water Resources and Hydromechanics Laboratory, Purdue Univ., Lafayette, Ind., p. 145, 1971.

Kouwen, N. and R. M. Li, Biomechanics of Vegetative Channel Linings. J. of Hydraul. Div. ASCE, 106(HY6) pp.1085-1103, 1980.

Kramer, L. A. and L. D. Meyer, Small Amounts of Surface Runoff Reduce Soil Erosion and Runoff Velocity. Trans. of ASAE, 12, pp. 638-641 & 648, 1969.

Kuchment, L. S., A Two-Dimensional Rainfall-Runoff Model: Identification of Parameters and Possible Use for Hydrological Forecasts. In Hydrological Forecasting, Proc. of Oxford Symp., IAHS-AISH Publ. no.129, pp.215-219, 1980.

Lai, C., Numerical Modeling of Unsteady Open-Channel Flow, Advances in Hydroscience, 14, pp.161-333, 1986.

Li, R. M., D. B. Simons, and M. A. Stevens, Kinematic Wave Approximation for Water Routing. Water Resour. Res., 11(2), pp.245-252, 1975.

Liggett, J. A. and J. A. Cunge, Numerical Methods of Solution of the Unsteady Flow Equations. In Unsteady Flow in Open Channels, Water Resour. Publ., pp. 89-182, 1975.

Liggett, J. A. and D. A. Woolhiser, Difference Solutions of the Shallow-Water Equation, J. Eng. Mech. Div. ASCE, 93(EM2), pp. 39-71, 1967.

Lighthill, M. J. and G. B. Whitham, On Kinematic Waves, 1. Flood Movement in Long Rivers. Proc. of Royal Soc., Series A, 229, pp.281-316, 1955.

Linsley, R. K. and J. B. Franzini, Water Resources Engineering. McGraw-Hill Book Co., 1979.

Loague, K. M., Impact of Rainfall and Soil Hydraulic Property Information on Runoff Predictions as the Hillslope Scale. Water Resour. Res., 24(9), pp.1501-1510, 1988.

Lyatkher, V. M. and I. N. Gurin, Hydraulic Characteristics of Flows over A Surface Covered with Herbaceous Vegetation. Vodnye Resursy, No. 3, pp. 159-168, 1977.

MacCormack, R. W., The Effect of Viscosity in Hypervelocity Impact Cratering, Pap. 69-354, Am. Inst. Aeronaut. and Astronaut., New York, 1969.

MacCormack, R. W., Numerical Solution of the Interaction of A Shock Wave with A Laminar Boundary Layer, Lecture Notes in Physics, Vol. 8 pp.151-163, Springer-verlag, 1971.

Matias, P. and F. N. Correia, Spatial Variability of Saturated Hydraulic Conductivity and Its Impact on Modeling the Infiltration and Runoff Processes. IUGG/UGGI XIX General Assembly, HW2-Spatial Variability and Representativeness of Hydrogeological Parameters, Vancouver, B.C., Can., 1987.

McCuen, R. H., W. J. Rawls and D. L. Brakensiek, Statistical Analysis of the Brooks-Corey and the Green-Ampt Parameters across Soil Textures. Water Resour. Res., 17(4), pp.1005-1013, 1981.

Miller, J. E., Basic Concepts of Kinematic-Wave Models. USGS Prof. Paper 1302, p.29, 1984.

Morel-Seytoux, H.J., Derivation of Equations for Variable Rainfall Infiltration. Water Resour. Res., 14(4), pp. 561-568, 1978.

Morel-Seytoux, H.J., Analytical Results for Prediction of Variable Rainfall Infiltration. J. of Hydrol., 59, pp. 209-230, 1982.

Morgan, R. P. C., Field Studies of Sediment Transport by Overland Flow. Earth Surface Processes, 5, pp.307-316, 1980.

Morris, E. M. and D. A. Woolhiser, Unsteady One-Dimensional Flow over A Plane: Partial Equilibrium and Recession Hydrographs. Water Resour. Res., 16(2), pp.355-360, 1980.

Nielson, D.R., J.W. Biggar and K.T. Erh, Spatial Variability of Field-Measured Soil-Water Properties, Hilgardia 42(7), pp.214-259, 1973.

Petryk, S. and G. Bosmajian III, Analysis of Flow Through Vegetation. J. of Hydraul. Div. ASCE, 101(HY7), pp. 871-884, 1975.

Philip, J. R., The Theory of Infiltration: 1. The Infiltration Equation and Tis Solution. Soil Sciences, pp.345-357, 1957.

Philip, J. R., The Theory of Infiltration: 2. The Profiles at Infinity. Soil Sciences, pp.435-448, 1958.

Ponce, V. M., R. M. Li and D. B. Simons, Applicability of Kinematic and Diffusion Models. J. of Hydraul. Div. ASCE, 104, HY3, pp.353-360, 1978.

Reid, L. M. and T. Dunne, Sediment Production from Forest Road Surfaces. Water Resour. Res. 20(11), pp.1753-1761, 1984.

Richards, L. A., Capillary Condition of Liquids through Porous Mediums. Physics, 1, pp.318-333, 1931.

Rubin, J., Theory of Rainfall Uptake by Soils Initially Drier Than Their Field Capacity and Its Applications. Water Resour. Res. 2(4), pp.739-799, 1966.

Russo, D. and E. Bresler, Soil Hydraulic Properties as Stochastic Processes: 1. An Analysis of Field Spatial Variability. Soil Sci. Soc. Amer. J. 45, pp.682-687, 1981.

Schumm, S. A., M. P., Mosley and W. E. Weaver, Experimental Fluvial Geomorphology. A Wiley-Intersci. Publ., John Wiley & Sons, p.413, 1987.

Shen, H.W. and R.M. Li, Rainfall Effect on Sheet Flow over Smooth Surface, J. Hydraul. Div. ASCE, 99(HY5), pp. 771-792, 1973.

Simons, D. B., R. M. Li and M. A. Stevens, Development of Models for Predicting Water and Sediment Routing and Yield from Storms on Small Watershed. USDA For. Ser., Rocky Mount. For. and Range Exp. Sta., 1975.

Smith, J. D., "Princeples of Sediemnt Transport by Turbullent Flow." Lecture Notes, University of Washington, 1984.

Smith, R. E. and R. H. B. Hebbert, A Monte Carlo Analysis of the Hydrologic Effects of Spatial Variability of Infiltration. Water Resour. Res., 15(2), pp.419-429, 1979.

Smith, R.E. and J.Y. Palange, A Parameter-Efficient Hydrologic Infiltration Model. Water Resour. Res., 14(3), pp. 533-538, 1978.

Sokolov, V.G., Hydrodynamic and Hydraulic Equations Describing Rainwater Runoff from Slopes with

Allowance for Infiltration, Vodnyye Resursy (Water Resources), No. 2, pp. 95-110, 1973.

Strahler, A.N., Physical Geography, 4th ed. Wiley, New York, 1975.

Temple, D. M., Velocity Distribution Coefficients for Grass-Lined Channels. J. of Hydraul. Eng. ASCE, 112(3), pp. 193-205, 1986.

Vieira, S. R., D. R. Nielsen and J. W. Biggar, Spatial Variability of Field-Measured Infiltration Rate. Soil Soc. Amer. J. 45, pp.1040-1048, 1981.

Wagenet, D. W., Variability of Field Measured Infiltration Rates. M.S. Thesis, Utah State Univ., Logan, UT, p.106, 1981.

Woolhiser, D.A., Simulation of Unsteady Overland Flow. In Unsteady Flow in Open Channels. Water Resour. Publ., pp. 485-508, 1975.

Woolhiser, D. A. and D. C. Goodrich, Effect of Storm Rainfall Intensity Patterns on Surface Runoff. J. of Hydrology, 102, pp335-352, 1988

Woolhiser, D. A., C. L. Hanson and A. R. Kuhlman, Overland Flow on Rangeland Watersheds. J. of Hydrology (NZ), 9, pp.336-356, 1970.

Woolhiser, D.A. and J. A. Liggett, Unsteady, One-Dimensional Flow over A Plane - The Rising Hydrograph, Water Resour. Res., 3(3), pp. 39-71, 1967.

Wu, Y-H, V. Yevjevich and D. A. Woolhiser, Effects of Surface Roughness and Its Spatial Distribution on Runoff Hydrographs. Hydrol. Paper 96, p.47, Colo. State Univ., Fort Collins, 1978.

Yoon, Y.N. and H.G. Wenzel, Mechanics of Sheet Flow under Simulated Rainfall. Proc. of ASCE, J. of Hydraul. Div., 97(HY9), pp.1367-1386, 1971.

Zhang, W-H, Modeling of Overland Flow and Erosion on A Forest Road Surface. M.S. Thesis, Univ. of Washington, p.137, 1985.

APPENDIX A:

Derivation of the Two-Dimensional Overland Flow Equations

Two-Dimensional Continuity Equation

The two-dimensional continuity equation is obtained by integrating equation 19 over the flow depth, i.e,

$$\int_{\eta}^{\xi} \frac{\partial u}{\partial x}\, dz + \int_{\eta}^{\xi} \frac{\partial v}{\partial y}\, dz + w_{\xi} - w_{\eta} = 0 \qquad (A.1)$$

Applying the Leibnitz rule, the first two integral terms become

$$\int_{\eta}^{\xi} \frac{\partial u}{\partial x}\, dz = \frac{\partial}{\partial x} \int_{\eta}^{\xi} u\, dz - u_{\xi} \frac{\partial \xi}{\partial x} + u_{\eta} \frac{\partial \eta}{\partial x} \qquad (A.2)$$

$$\int_{\eta}^{\xi} \frac{\partial v}{\partial y}\, dz = \frac{\partial}{\partial y} \int_{\eta}^{\xi} v\, dz - v_{\xi} \frac{\partial \xi}{\partial y} + v_{\eta} \frac{\partial \eta}{\partial y} \qquad (A.3)$$

where the terms associated with u_{η} and v_{η} vanish because of a non-slip boundary condition. Denoting q_x and q_y as flow rate per unit width in x and y directions, respectively, we have

$$q_x = \int_{\eta}^{\xi} u\, dz \qquad (A.4)$$

$$q_y = \int_{\eta}^{\xi} v\, dz \qquad (A.5)$$

Substitution of these terms into Eq. A.1 and with consideration of the boundary conditions (equations 27 and 28) yields the two-dimensional continuity equation

$$\frac{\partial h}{\partial t} + \frac{\partial q_x}{\partial x} + \frac{\partial q_y}{\partial y} = r(x,y,t) - f(x,y,t) \qquad (A.6)$$

Two-Dimensional Momentum Equations

In the derivation of the two-dimensional equations, the following assumptions were made: 1) for a shallow water flow of long waves, the vertical acceleration of a fluid particle, dw/dt, is small in comparison with the acceleration of gravity, 2) again in the case of long waves, the shear stresses due to the vertical velocity component, $\nabla^2 w$, are also small, 3) the terms due to horizontal shear on vertical surfaces, $\partial^2 u/\partial x^2$, $\partial^2 u/\partial y^2$, $\partial^2 v/\partial x^2$ and $\partial^2 v/\partial y^2$ are small compared with the terms due to vertical shear on horizontal surfaces, $\partial^2 u/\partial z^2$ and $\partial^2 v/\partial z^2$. Omitting these terms from equation 22 yields

$$0 = -\frac{1}{\rho}\frac{\partial p}{\partial z} - g \qquad (A.7)$$

Integrating A.7 with respect to z and setting the atmospheric pressure at the water surface, p_ξ, to a constant yield

$$p = p_\xi + \rho g(\xi - z) \tag{A.8}$$

Integrating equation 20 over the flow depth, we have

$$\int_\eta^\xi \frac{\partial u}{\partial t}\,dz + \int_\eta^\xi \frac{\partial uu}{\partial x}\,dz + \int_\eta^\xi \frac{\partial vu}{\partial y}\,dz + \int_\eta^\xi \frac{\partial wu}{\partial z}\,dz$$
$$= -\frac{1}{\rho}\int_\eta^\xi \frac{\partial p}{\partial x}\,dz + \frac{1}{\rho}\int_\eta^\xi \frac{\partial \tau_{zx}}{\partial z}\,dz \tag{A.9}$$

Applying the Leibnitz rule to the four terms on the left hand side of the equation, we have

$$\int_\eta^\xi \frac{\partial u}{\partial t}\,dz = \frac{\partial}{\partial t}\int_\eta^\xi u\,dz - u_\xi\frac{\partial \xi}{\partial t} + u_\eta\frac{\partial \eta}{\partial t} \tag{A.10}$$

$$\int_\eta^\xi \frac{\partial uu}{\partial x}\,dz = \frac{\partial}{\partial x}\int_\eta^\xi uu\,dz - u_\xi{}^2\frac{\partial \xi}{\partial x} + u_\eta{}^2\frac{\partial \eta}{\partial x} \tag{A.11}$$

$$\int_\eta^\xi \frac{\partial vu}{\partial y}\,dz = \frac{\partial}{\partial y}\int_\eta^\xi vu\,dz - v_\xi u_\xi\frac{\partial \xi}{\partial y} + v_\eta u_\eta\frac{\partial \eta}{\partial y} \tag{A.12}$$

$$\int_\eta^\xi \frac{\partial wu}{\partial z}\,dz = \frac{\partial}{\partial z}\int_\eta^\xi wu\,dz - w_\xi u_\xi\frac{\partial \xi}{\partial z} + w_\eta u_\eta\frac{\partial \eta}{\partial z} \tag{A.13}$$

Again, the terms associated with v_η and u_η vanish, and noting that

$$\frac{\partial}{\partial t}\int_\eta^\xi u\,dz = \frac{\partial q_x}{\partial t} \tag{A.14}$$

and

$$\int_{\eta}^{\xi} wu \, dz = w_{\xi} u_{\xi} \tag{A.15}$$

From Eq. A.8, the pressure term in Eq. A.9 becomes

$$\frac{1}{\rho} \int_{\eta}^{\xi} \frac{\partial p}{\partial z} \, dz = g(\xi-\eta)\left[\frac{\partial(\xi-\eta)}{\partial x} + \frac{\partial \eta}{\partial x} \right] \tag{A.16}$$

The integrals of shear stress terms in Eq. A.9 may be discussed separately for laminar and turbulent flows. For laminar flow, only the viscous shear stress term remains in equation 24. Thus, the integral in the vertical direction is

$$\int_{\eta}^{\xi} \frac{\partial \tau_{zx}}{\partial z} \, dz = \int_{\eta}^{\xi} \mu \frac{\partial^2 u}{\partial z^2} \, dz = \mu \frac{\partial u}{\partial z}\bigg|_{\xi} - \mu \frac{\partial u}{\partial z}\bigg|_{\eta} = (\tau^{\xi}_{x} - \tau^{\eta}_{x}) \tag{A.17}$$

where τ^{ξ}_{x} and τ^{η}_{x} are the shear stresses for laminar flow.

For turbulent flow, the Reynolds stress term is considered. Since there is no universally accepted way to relate Reynolds stress to average velocity profiles, direct integration of the Reynolds stress over the flow depth is difficult. Using an analogy to Newton's law of friction for laminar flow, Boussinesq proposed an eddy viscosity approach to replace the Reynolds stress, i.e.

$$\tau_{zx} = -\rho\langle u'w'\rangle = \epsilon\frac{\partial u}{\partial z} \tag{A.18}$$

where ϵ is the eddy viscosity for turbulent flow. Unlike the kinematic viscosity for laminar flow, the eddy viscosity may vary with flow velocity. Although studies to date have proposed several theories relating the eddy viscosity with flow velocity, e.g., Prandtl's eddy viscosity or mixing length theory, they all have many shortcomings and introduce more empirical constants; thus, are difficult to use (Dronkers, 1964). Therefore, the assumption of constant ϵ is usually made and is adopted in this study. As for the laminar flow case, by integrating the derivative term of the stress with respect to the flow depth, we have

$$\int_{\eta}^{\xi}\frac{\partial \tau_{zx}}{\partial z}\,dz = \int_{\eta}^{\xi}\epsilon\frac{\partial^2 u}{\partial z^2}\,dz = \epsilon\frac{\partial u}{\partial z}\bigg|_{\xi} - \epsilon\frac{\partial u}{\partial z}\bigg|_{\eta} = (\tau^{\xi}{}_{x} - \tau^{\eta}{}_{x}) \tag{A.19}$$

where, $\tau^{\xi}{}_{x}$ and $\tau^{\eta}{}_{x}$ represent the shear stresses for turbulent flow.

Substituting equations A.10 through A.18 (or A.19) into equation A.9 and using the boundary conditions (equations 27 and 28) yields

$$\frac{\partial q_x}{\partial t} + \frac{\partial}{\partial x}\int_{\eta}^{\xi} uu\,dz + \frac{\partial}{\partial y}\int_{\eta}^{\xi} vu\,dz - u_{\xi}R$$

$$= -g(\xi-\eta)\left[\frac{\partial(\xi-\eta)}{\partial x} + \frac{\partial \eta}{\partial x}\right] + \frac{1}{\rho}(\tau^{\xi}_{x} - \tau^{\eta}_{x}) \qquad (A.20)$$

By introducing momentum correction factors, β_x and β_{xy}, we make the following approximation

$$\int_{\eta}^{\xi} uu\, dz = \beta_x uu(\xi-\eta) \qquad (A.21)$$

$$\int_{\eta}^{\xi} vu\, dz = \beta_{xy} vu(\xi-\eta) \qquad (A.22)$$

Substituting them into equation A.20, we obtain the two-dimensional momentum equation for overland flow as

$$\frac{\partial q_x}{\partial t} + \frac{\partial[\beta_x uu(\xi-\eta)]}{\partial x} + \frac{\partial[\beta_{xy} vu(\xi-\eta)]}{\partial y} - u_{\xi} R$$
$$= -g(\xi-\eta)\left[\frac{\partial(\xi-\eta)}{\partial x} + \frac{\partial \eta}{\partial x}\right] + \frac{1}{\rho}(\tau^{\xi}_{x} - \tau^{\eta}_{x}) \qquad (A.23)$$

Similarly, for the y direction

$$\frac{\partial q_y}{\partial t} + \frac{\partial[\beta_y vv(\xi-\eta)]}{\partial y} + \frac{\partial[\beta_{xy} uv(\xi-\eta)]}{\partial x} - v_{\xi} R$$
$$= -g(\xi-\eta)\left[\frac{\partial(\xi-\eta)}{\partial y} + \frac{\partial \eta}{\partial y}\right] + \frac{1}{\rho}(\tau^{\xi}_{y} - \tau^{\eta}_{y}) \qquad (A.24)$$

Replacing the velocity terms, u and v, in equations A.23 and A.24 with the discharge terms, q_x and q_y, we obtain equations 30 and 31.

APPENDIX B: List of the Cases for Model Simulation

The following tables give the values of all parameters and variables used in the numerical experiments reported. These parameters and variables are defined in section 4.3.

Table B.1: Cases of random variation in K_s

CASE	r (cm/hr)	S_x	K_o	μ_{Ks} (cm/hr)	σ_{Ks} (cm/hr)	CV_{Ks}
FOR1	15	0.05	512	5.0	1.0	0.2
FOR2	15	0.05	512	5.0	1.5	0.3
FOR3	15	0.05	512	5.0	2.0	0.4
FOR4	15	0.05	1000	5.0	1.0	0.2
FOR5	15	0.05	1000	5.0	1.5	0.3
FOR6	15	0.05	1000	5.0	2.0	0.4
FOR21	15	0.10	512	5.0	1.0	0.2
FOR22	15	0.10	512	5.0	1.5	0.3
FOR23	15	0.10	512	5.0	2.0	0.4
FOR28	15	0.10	1000	5.0	1.0	0.2
FOR29	15	0.10	1000	5.0	1.5	0.3
FOR30	15	0.10	1000	5.0	2.0	0.4
FOR31	11	0.05	1000	5.0	1.0	0.2
FOR32	11	0.05	1000	5.0	1.5	0.3
FOR33	11	0.05	1000	5.0	2.0	0.4

Table B.2: Cases of trending variation in K_s

(a) downslope increase

CASE	r (cm/hr)	S_x	K_o	μ_{Ks} (cm/hr)	K_s^U (cm/hr)	K_s^L (cm/hr)
FI1	15	0.05	512	5.0	0.0	10.0
FI2	15	0.05	512	5.0	2.0	8.0
FI3	15	0.05	512	5.0	4.0	6.0
FI4	15	0.05	1000	5.0	0.0	10.0
FI5	15	0.05	1000	5.0	2.0	8.0
FI6	15	0.05	1000	5.0	4.0	6.0
FI7	15	0.10	512	5.0	0.0	10.0
FI8	15	0.10	512	5.0	2.0	8.0
FI9	15	0.10	512	5.0	4.0	6.0
FI10	15	0.10	1000	5.0	0.0	10.0
FI11	15	0.10	1000	5.0	2.0	8.0
FI12	15	0.10	1000	5.0	4.0	6.0
FI13	11	0.05	1000	5.0	0.0	10.0
FI14	11	0.05	1000	5.0	2.0	8.0
FI15	11	0.05	1000	5.0	4.0	6.0

(b) downslope decrease

CASE	r (cm/hr)	S_x	K_o	μ_{Ks} (cm/hr)	K_s^L (cm/hr)	K_s^U (cm/hr)
FD1	15	0.05	512	5.0	0.0	10.0
FD2	15	0.05	512	5.0	2.0	8.0
FD3	15	0.05	512	5.0	4.0	6.0
FD4	15	0.05	1000	5.0	0.0	10.0
FD5	15	0.05	1000	5.0	2.0	8.0
FD6	15	0.05	1000	5.0	4.0	6.0
FD7	15	0.10	512	5.0	0.0	10.0
FD8	15	0.10	512	5.0	2.0	8.0
FD9	15	0.10	512	5.0	4.0	6.0
FD10	15	0.10	1000	5.0	0.0	10.0
FD11	15	0.10	1000	5.0	2.0	8.0
FD12	15	0.10	1000	5.0	4.0	6.0
FD13	11	0.05	1000	5.0	0.0	10.0
FD14	11	0.05	1000	5.0	2.0	8.0
FD15	11	0.05	1000	5.0	4.0	6.0

Table B.3. Cases of trending variation in K_s with embedded randomness

CASE	r (cm/hr)	S_x	K_o	trending		random	
				K_s^U (cm/hr)	K_s^L	μ_{Ks} (cm/hr)	σ_{Ks}
FTI1	15	0.1	1000	2.0	8.0	0.0	0.5
FTI2	15	0.1	1000	2.0	8.0	0.0	1.0
FTD1	15	0.1	1000	8.0	2.0	0.0	0.5
FTD2	15	0.1	1000	8.0	2.0	0.0	1.0

Table B.4: Cases of random variation in K_o

CASE	r (cm/hr)	S_x	K_s (cm/hr)	μ_{Ko}	σ_{Ko}	CV_{Ko}
RUR71	15	0.05	5.0	512	51.2	0.1
RUR91	15	0.05	5.0	512	102.4	0.2
RUR81	15	0.05	5.0	512	153.6	0.3
RUR72	15	0.05	5.0	1000	100	0.1
RUR92	15	0.05	5.0	1000	200	0.2
RUR82	15	0.05	5.0	1000	300	0.3
RUR212	15	0.05	10.0	512	51.2	0.1
RUR232	15	0.05	10.0	512	102.4	0.2
RUR222	15	0.05	10.0	512	153.6	0.3
RUR112	15	0.05	10.0	1000	100	0.1
RUR132	15	0.05	10.0	1000	200	0.2
RUR122	15	0.05	10.0	1000	300	0.3
RUR11	15	0.10	5.0	512	51.2	0.1
RUR31	15	0.10	5.0	512	102.4	0.2
RUR21	15	0.10	5.0	512	153.6	0.3
RUR12	15	0.10	5.0	1000	100	0.1
RUR32	15	0.10	5.0	1000	200	0.2
RUR22	15	0.10	5.0	1000	300	0.3
RUR41	15	0.10	10.0	512	51.2	0.1
RUR61	15	0.10	10.0	512	102.4	0.2
RUR51	15	0.10	10.0	512	153.6	0.3
RUR42	15	0.10	10.0	1000	100	0.1
RUR62	15	0.10	10.0	1000	200	0.2
RUR52	15	0.10	10.0	1000	300	0.3

Table B.5: Cases of trending variation in Ko

(a) downslope increase

CASE	r (cm/hr)	S_x	K_s (cm/hr)	μ_{Ko}	K_o^U	K_o^L
RI1	15	0.05	5	512	200	824
RI2	15	0.05	5	512	300	724
RI3	15	0.05	5	512	400	624
RI4	15	0.10	5	512	200	824
RI5	15	0.10	5	512	300	724
RI6	15	0.10	5	512	400	624
RI7	11	0.05	5	512	200	824
RI8	11	0.05	5	512	300	724
RI9	11	0.05	5	512	400	624
RI10	11	0.05	5	1000	100	1900
RI11	11	0.05	5	1000	500	1500
RI12	11	0.05	5	1000	900	1100

(b) downslope decrease

CASE	r (cm/hr)	S_x	K_s (cm/hr)	μ_{Ko}	K_o^L	K_o^U
RD1	15	0.05	5	512	200	824
RD2	15	0.05	5	512	300	724
RD3	15	0.05	5	512	400	624
RD4	15	0.10	5	512	200	824
RD5	15	0.10	5	512	300	724
RD6	15	0.10	5	512	400	624
RD7	11	0.05	5	512	200	824
RD8	11	0.05	5	512	300	724
RD9	11	0.05	5	512	400	624
RD10	11	0.05	5	1000	100	1900
RD11	11	0.05	5	1000	500	1500
RD12	11	0.05	5	1000	900	1100

Table B.6. Cases of trending variation in K_o with embedded randomness

CASE	r (cm/hr)	S_x	K_s (cm/hr)	trending		random	
				K_o^U	K_o^L	μ_{Ko}	σ_{Ko}
RTI1	15	0.05	5	300	724	0.0	51.2
RTI2	15	0.05	5	300	724	0.0	102.4
RTD1	15	0.05	5	724	300	0.0	51.2
RTD2	15	0.05	5	724	300	0.0	102.4

Table B.7: Cases of two-dimensional corrugated microtopography

CASE	r (cm/hr)	S_x	K_s (cm/hr)	K_o	a_x (cm)	a_y (cm)	λ_x (cm)	λ_y (cm)
M321	15	.05	5	512	.5	.5	283	283
M331	15	.05	5	512	.5	.5	424	424
M341	15	.05	5	512	.5	.5	566	566
M322	15	.05	5	512	1.0	1.0	283	283
M332	15	.05	5	512	1.0	1.0	424	424
M342	15	.05	5	512	1.0	1.0	566	566
M323	15	.05	5	512	1.5	1.5	283	283
M333	15	.05	5	512	1.5	1.5	424	424
M343	15	.05	5	512	1.5	1.5	566	566
M361	15	.05	5	1000	.5	.5	283	283
M371	15	.05	5	1000	.5	.5	424	424
M381	15	.05	5	1000	.5	.5	566	566
M362	15	.05	5	1000	1.0	1.0	283	283
M372	15	.05	5	1000	1.0	1.0	424	424
M382	15	.05	5	1000	1.0	1.0	566	566
M363	15	.05	5	1000	1.5	1.5	283	283
M373	15	.05	5	1000	1.5	1.5	424	424
M383	15	.05	5	1000	1.5	1.5	566	566
M21	15	.10	5	512	.5	.5	283	283
M31	15	.10	5	512	.5	.5	424	424
M41	15	.10	5	512	.5	.5	566	566
M22	15	.10	5	512	1.0	1.0	283	283
M32	15	.10	5	512	1.0	1.0	424	424
M42	15	.10	5	512	1.0	1.0	566	566
M23	15	.10	5	512	1.5	1.5	283	283
M33	15	.10	5	512	1.5	1.5	424	424
M43	15	.10	5	512	1.5	1.5	566	566
M61	15	.10	5	1000	.5	.5	283	283
M71	15	.10	5	1000	.5	.5	424	424
M81	15	.10	5	1000	.5	.5	566	566
M62	15	.10	5	1000	1.0	1.0	283	283
M72	15	.10	5	1000	1.0	1.0	424	424
M82	15	.10	5	1000	1.0	1.0	566	566

Table B.7: continued.

M63	15	.10	5	1000	1.5	1.5	283	283
M73	15	.10	5	1000	1.5	1.5	424	424
M83	15	.10	5	1000	1.5	1.5	566	566
M101	15	.10	10	512	.5	.5	283	283
M111	15	.10	10	512	.5	.5	424	424
M121	15	.10	10	512	.5	.5	566	566
M102	15	.10	10	512	1.0	1.0	283	283
M112	15	.10	10	512	1.0	1.0	424	424
M122	15	.10	10	512	1.0	1.0	566	566
M103	15	.10	10	512	1.5	1.5	283	283
M113	15	.10	10	512	1.5	1.5	424	424
M123	15	.10	10	512	1.5	1.5	566	566

VITA

Weihua Zhang was born on April 25, 1957 in Hebei, the People's Republic of China. He received his Bachelor of Science Degree in Forest Hydrology and Engineering from Beijing Forestry University (formally, Beijing Forestry College) in 1981. In 1983, he studied at the College of Environmental Science and Forestry, State University of New York at Syracuse. In 1984, he transferred to the College of Forest Resources, University of Washington at Seattle from which he received his Master of Science Degree in Forest Hydrology in 1985. In 1986, he entered the Department of Civil Engineering, University of Washington at Seattle, and earned his Ph.D. in Hydrology and Water Resources in 1990.